Distribution Agreement

In presenting this thesis or dissertation as a partial fulfillment of the requirements for an advanced degree from Emory University, I hereby grant to Emory University and its agents the non-exclusive license to archive, make accessible, and display my thesis or dissertation in whole or in part in all forms of media, now or hereafter known, including display on the world wide web. I understand that I may select some access restrictions as part of the online submission of this thesis or dissertation. I retain all ownership rights to the copyright of the thesis or dissertation. I also retain the right to use in future works (such as articles or books) all or part of this thesis or dissertation.

Signature:

_____ _____

Jacob C. Laas Date

Methanol Photodissociation as a Case Study For Probing Complex Interstellar Organic Chemistry

By

Jacob C. Laas
Doctor of Philosophy

Chemistry

Susanna L. Widicus Weaver, Ph.D.
Advisor

Joel M. Bowman, Ph.D.
Committee Member

Michael C. Heaven, Ph.D.
Committee Member

Accepted:

Lisa A. Tedesco, Ph.D.
Dean of the James T. Laney School of Graduate Studies

Date

Methanol Photodissociation as a Case Study For Probing Complex Interstellar Organic Chemistry

By

Jacob C. Laas
B.S., Pittsburg State University, 2008

Advisor: Susanna L. Widicus Weaver, Ph.D.

An abstract of
A dissertation submitted to the Faculty of the
James T. Laney School of Graduate Studiesof Emory University
in partial fulfillment of the requirements for the degree of
Doctor of Philosophy
in Chemistry
2014

Abstract

Methanol Photodissociation as a Case Study For Probing Complex Interstellar Organic Chemistry

By Jacob C. Laas

Methanol is ubiquitous in interstellar molecular clouds and other molecule-rich extraterrestrial environments. Its reaction dynamics are therefore expected to be highly-influential on related chemistries. This was verified through astrochemical modeling, when it was found that the fractional abundances of methyl formate and its structural isomers glycolaldehyde and acetic acid can change by up to an order of magnitude if changes to the branching ratios of the cosmic-ray induced photodissociation of methanol are made. This is due to the fact that methanol photodissociation is the primary formation pathway for the molecular radicals methoxy (CH_3O), hydroxymethyl (CH_2OH), and methyl (CH_3) on grain surfaces under hot core/corino conditions, and these radicals may then go on to form larger COMs through radical-radical addition reactions. Motivated by these results, a millimeter/submillimeter absorption spectrometer has been implemented to quantitatively measure these branching ratios in the gas-phase, as well as provide more complete rotational line catalogs for methoxy and hydroxmethyl. Spectral line surveys of a statistically-significant population of star-forming regions have also been acquired through observational radio astronomy so as to better constrain astrochemical models by cataloging their molecular inventories. I present here the results of the modeling, laboratory, and observational studies, and provide a discussion of each in the context of methanol playing a critical role in the complex organic chemistry of the interstellar medium.

Methanol Photodissociation as a Case Study For Probing Complex Interstellar Organic Chemistry

By

Jacob C. Laas
B.S., Pittsburg State University, 2008

Advisor: Susanna L. Widicus Weaver, Ph.D.

A dissertation submitted to the Faculty of the
James T. Laney School of Graduate Studiesof Emory University
in partial fulfillment of the requirements for the degree of
Doctor of Philosophy
in Chemistry
2014

Acknowledgments

Let me first begin with academe: First and foremost, a great big thanks is owed to my advisor Prof. Susanna Widicus Weaver. My committee members, Prof. Michael Heaven and Prof. Joel Bowman, are owed acknowledgment in guiding my work to success. I also owe thanks to Prof. Eric Herbst for being a mentor and someone to look up to. Prof. Robert Pavlis and Prof. Khamis Siam have both played important roles in my success at Pittsburg State University, and direct roles in my placement at Emory. Gary Leiker, Jayne Jones, Judy Tilley, Tammy Hall, and Carolyn Schwindt went above and beyond the call of duty as teachers, and they will always have my respect. Even further back in time, Kay Wright helped me learn about perseverance.

On a more practical level: Building an experimental apparatus is not the work of only one person, and I couldn't have done it without help from the rest of the Widicus Weaver research group, both past and present. Also, the early days were made much less painful, thanks to the generosity of Prof. Michael Heaven and Prof. Thom Orlando for loaning out laboratory equipment with which I could test things. A number of Emory support staff have been greatly helpful and patient: Horace Dale and Cody Anderson in the machine shop, Patti Barnett and Steve Krebs in the chemistry stockroom, Stephenie Thioubou with accounting, to name the most important few. Even if they had only been 'doing their job', the CSO staff did it in such a way that I didn't feel completely on my own during its operation: Diana Bisel, Richard Chamberlin, Ed Bufil, Hiroko Shinnaga, and Simon Radford.

Beyond academics, I couldn't have survived graduate school had it not been for such great friends and family. I have been privileged, indeed, to have so many. A great family was sure to keep me on the right footing, and so many friends have helped me through the good times and the bad. They all know who they are, and I will pardon the reader from such an exhaustive list...

To my parents, Lorri and Richard Laas…

Contents

List of Tables

List of Figures

List of Symbols and Abbreviations

A/D	Analog-to-digital converter
A_{ij}	Einstein A coefficient
B_{ij}	Einstein B coefficient
BRs	Branching ratios
COM	Complex organic molecule
CR	Cosmic-ray
CSO	Caltech Submillimeter Obervatory
DC	Direct current
E	Energy
FIR	Far-infrared
FTMW	Fourier transform microwave
GBT	Green Bank Telescope
GWWH08	Garrod, Widicus Weaver, and Herbst. *ApJ*. **2008**. *682*:283–302.

IC	Integrated circuit
IDP	Interplanetary dust particle
IR	Infrared
ISM	Interstellar medium
J	Total rotational angular momentum quantum number
JPL	Jet Propulsion Laboratory
k	Chemical rate coefficient
LIA	Lock-in amplifier
$M_\odot$	Solar mass
N_T	Total column density
PTFE	Polytetrafluoroethylene
SLWW	Susanna L. Widicus Weaver
SNR	Signal-to-noise ratio
T_A^*	Brightness temperature
t	Time
UV	Ultraviolet
yr	Year

λ	Spectral wavelength
ν	Spectral frequency
ρ (also ρ_i, ρ_f)	Gas density (general, initial, final)
σ	Standard deviation
σ_λ	Absorption cross section
$\Phi(T)$	Partition function
$\varnothing$	Diameter symbol

Chapter 1

Introduction

1.1 Interstellar Chemistry and Our Molecular Origins

To date, more than 180 molecules have been detected in space (Müller et al., 2005). While several species in this inventory are familiar among terrestrial chemistry, many occur on Earth only as transient intermediates or in low abundance within exotic environments, such as ultra-cold traps in the laboratory or high-temperature reactors. The motivation for the studies presented herein is the complete understanding of the connection between the molecules detected remotely across interstellar space and the chemistry of planetary systems and life. The chemistry we are familiar with on Earth is a far cry from the hydrogen gas and dust that dominate the vast expanse of our observable universe. While much has been discovered and understood within the field of astrochemistry during the last $\sim$40 years, many uncertainties remain. The purpose of the work presented herein is to improve our understanding of extraterrestrial organic chemistry so that we may make more sense of our molecular origins.

There are many distinct extraterrestrial environments in which COMs, defined per the convention suggested by Herbst and van Dishoeck (2009) as molecules consisting of 6 atoms or more, have been detected:

- dense clouds, particularly hot cores/corinos and other prestellar objects therein (Herbst and van Dishoeck, 2009);
- planetesimals within our Solar System (cometary coma, IDPs, asteroids/meteorites) (Mumma and Charnley, 2011; Pizzarello et al., 2013); and,
- circumstellar envelopes of evolved stars (Ziurys, 2006);

While dense clouds and the prestellar objects contained within are the most astrophysically primitive of these environments, they are home to the largest, most diverse inventories of extraterrestrial molecules detected to date. Many of the low-mass molecular clouds and cores are expected to continue their evolution into low-mass stars like the Sun (see, e.g. Carroll and Ostlie, 2007, §23.2). The most recent statistical analysis of data from NASA's exoplanet-finding mission, the *Kepler* spacecraft, suggests that Earth-like planets may be relatively common among Sun-like stars (Petigura et al., 2013). This then begs the questions of how, when, and where do the simple molecular inventories within primitive environments transform into the prebiotic chemistry that is more closely related to terrestrial life.

COMs can form in either the gas phase or condensed phase. Their gas-phase formation is generally inefficient—only ion-molecule reactions may contribute to their formation mechanisms due to the low densities and temperatures of molecular clouds—yet a plethora of processes readily contribute to their destruction (Herbst and van Dishoeck, 2009, §5.1.1). In the condensed phase, rates of additive processes are significantly enhanced due to the collisional dynamics and reduced dimensionality. While only H atoms are mobile in and on ices at temperatures as low as 10 K, heavier atoms and molecular species can become mobile at elevated temperatures ($\gtrsim$30 K). It is thought that the photo-driven reactions involving methanol and its dissociation products drive COM chemistry in these environments. To better understand these astrochemical dynamics, I present below a number of studies centered around methanol and its role in interstellar chemistry.

1.2 Methanol Photodissociation

Methanol is one of the most abundant COMs in the ISM. With a high binding energy to water ice due to its ability to hydrogen bond, it remains in the condensed phase in low-temperature systems—in many cases at up to $\sim$30% the total ice abundance. Its formation mechanism, while still somewhat uncertain, is generally understood to function through successive hydrogenation of CO on grains (see, e.g. Wirström et al., 2011, and references therein).

Due to its molecular complexity, methanol has a diverse set of possible fragmentation products:

$$\mathrm{CH_3OH} + \mathrm{h}\nu \longrightarrow \mathrm{CH_3} + \mathrm{OH}, \tag{1.1a}$$

$$\longrightarrow \mathrm{CH_2OH} + \mathrm{H}, \tag{1.1b}$$

$$\longrightarrow \mathrm{CH_3O} + \mathrm{H}, \tag{1.1c}$$

$$\longrightarrow \mathrm{CH_2} + \mathrm{H_2O}, \tag{1.1d}$$

$$\longrightarrow \mathrm{H_2CO} + \mathrm{H_2}, \tag{1.1e}$$

$$\longrightarrow \mathrm{HCOH} + \mathrm{H_2}. \tag{1.1f}$$

In the OSU gas/grain astrochemical network (Garrod et al., 2008), which is the most complete astrochemical modeling network available for complex organics, the primary products for methanol cosmic-ray induced photodissociation are considered to be methyl (1.1a), hydroxymethyl (1.1b), and methoxy (1.1c). The rate coefficient for the total cosmic-ray induced photodissociation of methanol is derived from gas-phase measurements to be 3.25×10^{-14} cm^{-3} s^{-1}; however, the branching ratios for its photodissociation are not known for certain, despite many previous attempts to measure these values in the laboratory.

Under certain physical conditions, methanol's high abundance makes its cosmic-ray induced photodissociation a significant factor in the chemistry of its fragmentation products.

Here, the fragmentation products are thought to combine through surface reactions to form more complex molecules. The methyl radical is modeled to be one of the most mobile molecular radicals on the grain surface, whereas hydroxymethyl is one of the least mobile radicals on the grain surface due in part to its ability to hydrogen bond to the ice matrix. The varying properties and different reactivities of each radical contribute to significantly diverging chemistry. It was thus hypothesized in Garrod et al. (2008) that reactions of these molecules play a significant role in the structural isomerism that is observed among interstellar COMs. Therefore, studies of methanol photodissociation and its dissociation products are the focus of the work presented here.

1.3 Thesis Overview

Chap. 2 presents a number of studies performed using astrochemical modeling. In §2.2.1, I first present the results of a study that aimed to test the effects of varying methanol photodissociation branching ratios on methyl formate and its structural isomers. In a related note—and also in Chap. 2—I present the results of modeling the efficiency of a novel gas-phase formation mechanism for methyl formate (§2.2.2).

In Chap. 3, I first present the design, construction, and benchmarking of a mm/submm gas-phase spectrometer (§3.2). I then present application of this spectrometer to various molecular systems (§3.3), namely attempts to measure methanol photodissociation BRs, and dedicated spectral studies of its dissociation products.

In Chap. 4, I present astronomical observations performed by the Widicus Weaver research group, and the tentative detection of methoxy in a number of broadband line surveys at $\lambda \approx 1.2$ mm.

Chapter 2

Astrochemical Modeling

Note. Much of the work presented herein (Chapter 2) can be found in the following publication:

J. C. Laas, R. T. Garrod, E. Herbst, and S. L. Widicus Weaver. *The Astrophysical Journal*, **2011**, *728*:71.

2.1 Background

Astrochemical modeling is an essential tool for bridging the gap between astronomical observations and the vast datasets supplied by laboratory studies of molecular systems. Models are key to testing hypotheses through their predictive power, as astronomy is purely an observational science.

The astrochemical modeling presented herein is based on that of Garrod et al. (2008, hereafter referred to as GWWH08), which consists of the most comprehensive chemical network for COMs to date (referred hereafter as the OSU gas/grain network). This model is important because it allows the study of small molecule chemistry on grain surfaces. Grain surface species become mobile at temperatures $\gtrsim$30 K and may lead to the formation of more complex species during star formation.

The physical model that is employed is based on the two stages that molecular clouds

experience during formation of hot cores. The first stage is an isothermal collapse from a gas number density of $\rho_i \approx 3 \times 10^3$ cm^{-3} to $\rho_f = 10^7$ cm^{-3}, at a temperature of 10 K, and for a time period of $\sim$10^6 yr. The second stage is a gradual warm-up in which the number density remains at $\rho = 10^7$ cm^{-3}, while the temperature increases via a second-order power law from 10 to 200 K. The timescale for this second stage varies depending on the mass of the molecular cloud: the fastest timescale is 5×10^4 yr for the most massive clouds ($\gtrsim$50 $M_\odot$), whereas the longest timescale is 10^6 yr for low-mass star-forming regions (Aikawa et al., 2008).

Initial abundances of most molecules in the pre-collapse clouds are negligible and all elements heavier than H are in their elemental form. The initial fractional abundances when the isothermal collapse begins are based on that of Graedel et al. (1982). The final fractional abundances for the isothermal collapse stage are then fed into the isobaric collapse stage.[a]

Presented below are two studies that were performed using this gas/grain astrochemical model: §2.2.1 discusses the effects that the methanol photodissociation branching ratios have on the relative abundances of methyl formate and its two structural isomers in hot cores; and §2.2.2 discusses the results of modeling new gas-phase formation pathways for interstellar methyl formate. Also, §2.2.4 briefly presents the results of a collaboration that involved implementing this gas/grain OSU network into a classical T Tauri type accretion disk, which focused on testing the extent to which COMs may form in protoplanetary disks from modern gas/grain chemistry.

2.2 Methyl Formate Formation

The highly abundant COM methyl formate ($HCOOCH_3$) has posed several challenges to the basic tenets of classical astrochemistry. Neither low-temperature surface chemistry via atom-addition reactions, nor gas-phase ion-molecule chemistry in warmer regions, can

[a]With the exception of methane (CH_4), formaldehyde (H_2CO), and methanol (CH_3OH), whose fractional abundances must each be reduced to better match observed ice abundances (see GWWH08, p. 294).

account for the relatively high fractional abundances of methyl formate, nor its ubiquity across a variety of interstellar environments. The size and complexity of this organic molecule and its disparate relative abundance with respect to its structural isomers make it an important species in interstellar chemistry. Understanding the role of methyl formate in interstellar chemical processes has had profound impacts on the way researchers have approached understanding the chemistry of other interstellar COMs.

In 2004, Horn et al. presented the results of an exhaustive set of *ab initio* quantum chemical calculations and laboratory measurements to characterize various gas-phase reactions that may lead to methyl formate formation. It had been previously speculated that methyl formate formed in the gas-phase though an ion-molecule formation reaction of a precursor ion (Ehrenfreund and Charnley, 2000). The main finding of this report, however, was that all of the considered gas-phase formation reactions involved energy barriers that were prohibitively high for molecular cloud temperatures ($T \lesssim 200$ K), and that methyl formate must form in the condensed phase on interstellar grains. This conclusion was further supported by evidence of methyl formate and other COMs detected in shock-dominated regions in the GC, where the gas-phase abundances are expected to represent those of the grain mantles due to extensive sputtering ((M. A. Requena-Torres et al., 2006).

2.2.1 Radical-Radical Addition Mechanism

In an attempt to model methyl formate grain-surface formation, an astrochemical code incorporating grain-surface chemistry was presented by Garrod and Herbst (2006). Under this model, radicals on the grain surface begin to dominate the organic chemistry of star-formation during the rising temperature (from 10 K to $\sim$200 K) of an evolving hot core. This study showed that methyl formate may form on grain surfaces directly from the reaction between the highly abundant formyl radical (HCO) and the methoxy radical (CH_3O). Intriguingly, glycolaldehyde, a sugar-like molecule of prebiotic interest, may also form directly from the reaction of formyl and another methanol photodissociation product, hy-

droxymethyl (CH_2OH). An expanded and revised gas/grain chemical network (GWWH08) confirmed the importance of this general model, leading Garrod et al. to hypothesize that methanol photodissociation may strongly govern the relative abundances of these isomers. Yet the extent of the influence of photodissociation on COM chemistry had remained unexplored. To test this hypothesis, a number of permutations on the branching ratios (BRs) of methanol's cosmic-ray-induced photodissociation were incorporated into the gas/grain network used in GWWH08. Attention was then focused on the affected abundances of methyl formate and its structural isomers during the warm-up phase of the model. Only the BRs for the CR-induced photodissociation of methanol were altered so that direct comparison could be made to previous work. The permutations of the CR-induced photodissociation BRs were tested for the gas-phase and grain surface processes, both individually to test the effects that each phase may contribute, and in combination to characterize the total effects.

Branching Ratio Sets

The following channels are those considered in the model for the photon- or CR-induced photodissociation of methanol:

$$\mathrm{CH_3OH} + \mathrm{h}\nu \longrightarrow \mathrm{CH_3} + \mathrm{OH}, \tag{2.1a}$$

$$\longrightarrow \mathrm{CH_2OH} + \mathrm{H}, \tag{2.1b}$$

$$\longrightarrow \mathrm{CH_3O} + \mathrm{H}. \tag{2.1c}$$

The sets of BRs to test, as summarized in Table 2.1, were chosen so that each photodissociation channel was emphasized in one of the BRs. This enables the quantification of the extreme limits of the reaction chemistry that may ensue following the evolution of the photodissociation products. The labeling scheme used hereafter is as follows: label = prefix_suffix_timescale, where the prefixes are:

- B (both grain surface and gas phase methanol photodissociation channels);

Table 2.1. Branching ratios of Reaction 1.1 used for different modeling trials.

Percent Branching Ratios 2.1a:2.1b:2.1c (%)	Label Suffix
60:20:20	Standard
90:5:5	Methyl
5:90:5	Hydroxymethyl
5:5:90	Methoxy

- S (grain surface channels only); or,
- G (gas phase methanol photodssociation channels only).

The suffixes refer to the BRs and are listed in Table 2.1, and the timescale is either:

- S (a slow warm-up time of 1×10^6 yr);
- M (a medium warm-up of 2×10^5 yr); or,
- F (a fast warm-up of 5×10^4 yr).

In the cases where the sets contained altered methanol photodissociation BRs only for the grain surface or gas phase reaction sets, the values for the unaltered reactions were set to the "standard" values (i.e. those used in GWWH08) by default. For example, the trial with methanol photodissociation BRs emphasizing the hydroxymethyl channel set to 90% on the grain surface (2.1a:2.1b:2.1c = 5:90:5) and tested at a medium warm-up timescale is labeled as "S_Hydroxymethyl_M," and the gas-phase methanol photodissociation BRs were kept at 2.1a:2.1b:2.1c = 60:20:20.

Results and Discussion

The results of the trials where only methanol photodissociation BRs were modified are shown in Figures 2.1–2.3. For the sake of simplification, only molecules that have been identified in the Sgr B2(N-LMH) hot core source have been included. Figure 2.1 compares

the peak fractional abundances determined using the standard BRs from GWWH08 and those predicted using grain surface BRs that emphasize the methoxy (CH_3O) channel. The slow warm-up timescale is shown for comparison in Figure 2.1, as this is the accepted timescale appropriate for hot cores like Sgr B2(N). Examination of Figure 2.1 reveals that the S_Methoxy_S trial gives a peak methyl formate abundance that is in better agreement with the observed abundance than the standard methanol photodissociation BRs used in GWWH08.

As is shown in more detail in Figure 2.2, the methoxy BRs give the best match between observations and peak fractional abundances for methyl formate, but both the acetic acid and glycolaldehyde peak fractional abundances better match observations when the methyl BRs are used. It should be noted here that the differences between these two trials for these two molecules are of the same magnitude as the estimated 20% uncertainty in the observational numbers. It is unclear from these results which set of BRs gives the best overall match to the relative abundances observed in Sgr B2(N). The set of BRs favoring the methoxy channel agrees qualitatively with gas phase laboratory measurements, which determined the overall branching fraction for the combined CH_3O and CH_2OH channels to be $\sim$0.75 (Hagege et al., 1968). To our knowledge, no gas phase or condensed phase laboratory measurements have yet distinguished between these two channels through direct measurements of the products. In contrast, neither set of BRs that gives a reasonable match to the Sgr B2(N) abundances agrees with the results of a recent laboratory study of methanol ice photodissociation, where the CH_2OH channel was found to dominate the other two pathways (Öberg et al., 2009). Regardless, it is clear that an increase in the methanol photodissociation branching fraction that leads to the methoxy channel is required to explain the methyl formate abundance observed in Sgr B2(N).

Despite the agreement observed in the S_Methoxy_S trial for methyl formate, and reasonable agreement in this trial for acetic acid, the predicted peak fractional abundance for glycolaldehyde in all trials is more than an order of magnitude higher than that observed

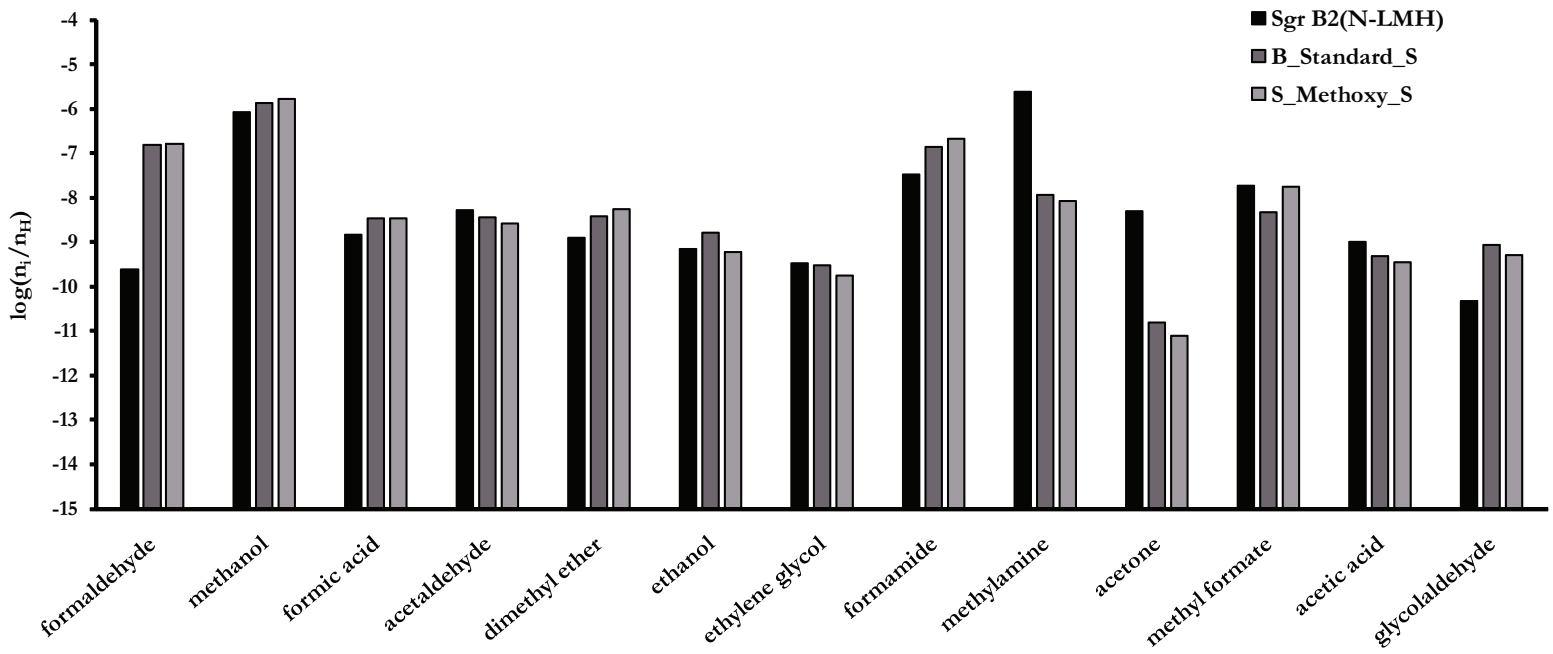

Figure 2.1 – Peak fractional abundances for a variety of interstellar species, comparing the observationally-determined values for Sgr B2(N-LMH) (as referenced in GWWH08), the standard branching ratio values from the GWWH08 study (i.e. B_Standard_S), and the S_Methoxy_S BRs used in this work.

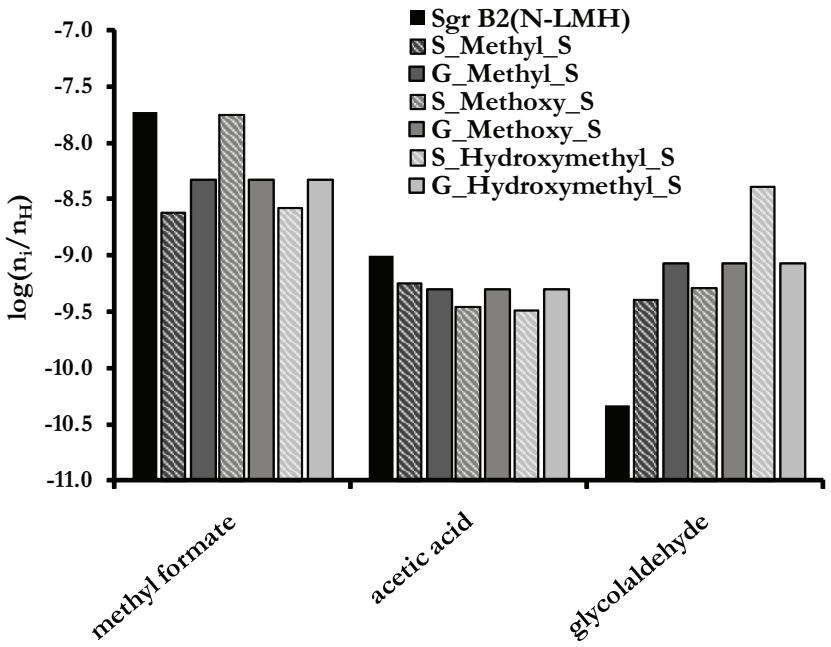

Figure 2.2 – Peak fractional abundances of methyl formate and its structural isomers for a warm-up time of 1×10^6 yr.

in Sgr B2(N-LMH). Glycolaldehyde is known to be cold (<50 K) and extended (>60″) in this source (Hollis et al., 2004), unlike its structural isomers methyl formate and acetic acid, which are both compact hot core molecules (Snyder, 2006). The peak abundance for glycolaldehyde occurs at a long timescale and high temperature in the model. If shocks released significant quantities of glycolaldehyde into the cold gas in the outer shells of the Sgr B2(N) hot core, then it is unrealistic to compare the peak gas phase abundance for glycolaldehyde in the model to the observed abundance. Direct comparison with the grain surface peak abundance is also not reasonable, because not all of the grain surface species would necessarily be released into the gas by the shock. Even if all grain surface glycolaldehyde was released by shocks into the gas phase, some fraction of the released glycolaldehyde would accrete back onto the grain at the lower temperatures of the outer envelope. Therefore, the only reasonable point of comparison is the $T = 80$–120 K range, where significant evaporation of grain surface glycolaldehyde is occurring. Indeed, the glycolaldehyde fractional abundance of 2–4×10^{-11} predicted by the model at $T \approx 100$ K

matches the value of 4×10^{-11} observed in Sgr B2(N-LMH).

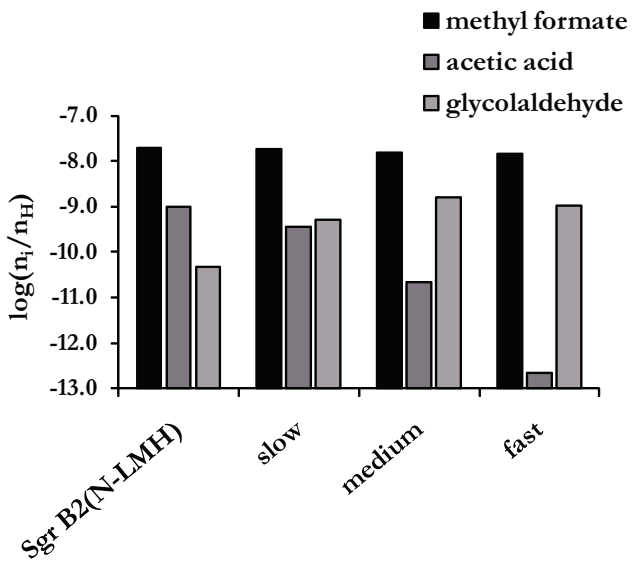

Figure 2.3 – Peak fractional abundances of methyl formate and its structural isomers, showing the timescale dependence predicted using the S_Methoxy BRs.

Looking beyond the influence of the grain surface photodissociation BRs, these trials reveal two other interesting trends. As is shown in Figure 2.2, the gas phase BRs have no influence on the peak abundances of COMs. This is to be expected, as the dominant formation mechanisms for these species are grain surface pathways. Additional examination of the results reveals that a change in warm-up timescale in addition to changes in the grain surface BRs can have a large influence on the peak abundances for COMs, as is illustrated by Figure 2.3. Fast warm-up timescales allow less time for chemistry, and so the more complex species are not formed efficiently under these conditions. This is especially true for a species such as acetic acid that forms from secondary radicals, as is evident in Figure 2.3. The longest warm-up timescale, which is typically associated with high-mass hot cores, gives the best match to the observed Sgr B2(N-LMH) abundances. Longer warm-up timescales should result in more chemical complexity.

2.2.2 Gas-Phase Ion-Neutral Mechanisms

In addition to the proposed grain surface formation of methyl formate and its structural isomers, recent theoretical investigations of ion-molecule reactions involving methyl formate suggest that gas phase formation routes beyond those previously employed in astrochemical models may be plausible (Neill et al., 2011). Methyl formate was long assumed to form from the Fischer esterification reaction involving protonated methanol ($CH_3OH_2^+$) and neutral formic acid (HCOOH). Yet Freeman et al. (1978a) found that this reaction was not significant, and Horn et al. (2004) showed that other ion-molecule leadings to methyl formate have high barriers that lead to slow reaction rates in interstellar environments. However, both of these studies only investigated pathways leading to the *cis* conformer of protonated methyl formate. While the *cis* conformer of neutral methyl formate is lower in energy than the *trans* conformer by 2880 K, the *trans* conformer of protonated methyl formate is lower in energy than the *cis* conformer by a similar value (Neill et al., 2011). To date, the only conformers of methyl formate or protonated methyl formate ($CH_3OCOH_2^+$) considered in astrochemical models are the *cis* stereoisomers. The energy barriers for interconversion between the *cis* and *trans* conformers of both species make conformer interconversion in interstellar environments unlikely. For the purpose of completeness in the chemical model, the viability of gas phase routes involving both stereoisomers should be examined.

Neill and coworkers (Neill et al., 2011) have suggested that Fischer esterification reactions between formic acid and methanol may be feasible gas phase formation routes for methyl formate. For this study, two Fischer esterification mechanisms were tested: the standard esterification mechanism with formic acid as the protonated reactant and a second esterification reaction with methanol as the protonated reactant. These two mechanisms and the steps taken to incorporate them into the model from GWWH08 are described below.

Route 1: Protonated Formic Acid + Methanol

The Fischer esterification reaction between protonated formic acid and methanol (hereafter referred to as Route 1) involves the reaction of protonated formic acid with methanol:

$$\mathrm{HCOOH_2^+ + CH_3OH \longrightarrow CH_3OCOH_2^+ + H_2O.} \tag{2.2}$$

This reaction was added to the reaction network and classified as a gas phase ion-molecule reaction with the standard rate expression. Additional related reactions, including the proton-transfer between methanol and formic acid, and a set of ion-neutral reactions involving formic acid, were also added to the network. The list of new reactions added to the network for Route 1 and the associated information for their rate coefficients are given in Table 2.2.

In addition to the new gas phase formation reactions, additional modifications were made to the network for the dissociative recombination (DR) reactions of protonated formic acid. These changes were based on the recent DR study of protonated formic acid at CRYRING (Vigren et al., 2010). In the original network, the following DR reactions for protonated formic acid were present:

$$\mathrm{HCOOH_2^+ + e^- \longrightarrow CO_2 + H_2 + H,} \tag{2.3}$$

and,

$$\mathrm{HCOOH_2^+ + e^- \longrightarrow HCOOH + H.} \tag{2.4}$$

In the present study, Reaction 2.3 was replaced with

$$\mathrm{HCOOH_2^+ + e^- \longrightarrow HCO + OH + H,} \tag{2.5}$$

so as to accommodate the higher likelihood of bonds between heavy atoms being cleaved;

Table 2.2. Changes to the reaction network based on Route 1.

Reactants	Products	Rate Coefficient Terms[a]			Reference
		α	β	γ	
$HCOOH_2^+ + CH_3OH$	$CH_3OCOH_2^+ + H_2O$	2.00×10^{-9} [b]	-0.5	2810	1
$CH_3OH_2^+ + HCOOH$	$CH_3OH + HCOOH_2^+$	3.70×10^{-10}	-0.5	685	2
$HCOOH_2^+ + CH_3OH$	$CH_3OH_2^+ + HCOOH$	2.29×10^{-9}	-0.5	0	3
$CH_5^+ + HCOOH$	$HCOOH_2^+ + CH_4$	3.00×10^{-9}	-0.5	0	2
$H_3^+ + HCOOH$	$HCO^+ + H_2O + H_2$	3.90×10^{-9}	-0.5	0	2, 4
$He^+ + HCOOH$	$HCO^+ + OH + He$	9.00×10^{-10}	-0.5	0	4
$C^+ + HCOOH$	$HCO^+ + OH + C$	8.00×10^{-10}	-0.5	0	4
$N_2H^+ + HCOOH$	$HCOOH_2^+ + N_2$	1.70×10^{-9}	-0.5	0	2
$H_2CN^+ + HCOOH$	$HCOOH_2^+ + HCN$	1.40×10^{-9}	-0.5	0	2
$H_3S^+ + HCOOH$	$HCOOH_2^+ + H_2S$	2.00×10^{-9}	-0.5	0	2
$H_2COH^+ + HCOOH$	$HCOOH_2^+ + H_2CO$	2.00×10^{-9}	-0.5	0	2

Notes.

[a] $k(T) = \alpha\ (T/300)^{\beta} \exp(-\gamma/T)$ cm^3 s^{-1}.

[b] The rate coefficient used here is identical with an estimate based on the Su-Chesnavich theory for reactions between ions and polar neutrals (Woon and Herbst, 2009) in the temperature range 10–300 K.

References. (1) Neill et al. (2011); (2) Freeman et al. (1978a); (3) Feng and Lifshitz (1994); (4) Freeman et al. (1978b).

Table 2.3 summarizes the DR reactions and their rate coefficients.

Route 2: Protonated Methanol + Formic Acid

A second esterification reaction leading to methyl formate, this time involving protonated methanol and formic acid, was also added to the network:

$$CH_3OH_2^+ + HCOOH \longrightarrow CH_3OCOH_2^+ + H_2O. \tag{2.6}$$

This pathway is hereafter referred to as Route 2. Here, the product can be either the *cis* or *trans* stereoisomer of protonated methyl formate. The pathway leading to the *cis* stereoisomer involves a 1320 K barrier, while the reaction leading to the *trans* stereoisomer does not

Table 2.3. Protonated formic acid DR reactions.

Reaction	Previous Rate Coefficient ($cm^3\ s^{-1}$)	New Rate Coefficient ($cm^3\ s^{-1}$)
2.3	$k(T) = 2.85 \times 10^{-7}\ (T/300)^{-0.5}$	0
2.4	$k(T) = 1.5 \times 10^{-8}\ (T/300)^{-0.5}$	$k(T) = 1.1 \times 10^{-7}\ (T/300)^{-0.78}$
2.5	0	$k(T) = 7.3 \times 10^{-7}\ (T/300)^{-0.78}$

have a barrier. These reactions were added to the network, and the α term in the rate coefficient expression was based on the experimental results of Freeman et al. (1978a), which gave a total α value of $3.7{\times}10^{-10}$ $cm^3\ s^{-1}$. In this study, the measurements focused on the proton-transfer reaction, rather than the formation of protonated methyl formate. The total rate determined for the proton-transfer reaction is higher than the rates determined for other similar reactions. It is not clear from this study whether the protonated methyl formate channel could have contributed to the overall rate measured in this experiment, but it is possible if this value was determined by monitoring the reactants and the assumption was made that the proton-transfer reaction was the only reaction channel. Based on this fact, and the unusually high value for the proton-transfer reaction rate determined in this study, it is reasonable to assume that the protonated methyl formate formation channel may have contributed to the overall measured value of the rate. We therefore used the more typical value for the proton-transfer reaction rate coefficient of $1.9{\times}10^{-10}$ $cm^3\ s^{-1}$, and derived from this a total rate coefficient for Route 2 to be $1.8{\times}10^{-10}$ $cm^3\ s^{-1}$. This rate coefficient is in agreement with those values used in the model for other similar reactions. The resultant rate coefficient information for the two esterification reactions leading to *cis* and *trans* protonated methyl formate is given in Table 2.4.

Methyl Formate Stereoisomers

In addition to the new reactions outlined above, the reaction network was modified so that a distinction was made between the *cis* and *trans* stereoisomers of methyl formate and its

Table 2.4. Changes to the reaction network based on Route 2.

Reactants	Products	Rate Coefficient Terms[a]		
		α	β	γ
$CH_3OH_2^+ + HCOOH$	*cis*-$CH_3OCOH_2^+ + H_2O$	1.8×10^{-10}	-0.5	1320
$CH_3OH_2^+ + HCOOH$	*trans*-$CH_3OCOH_2^+ + H_2O$	1.8×10^{-10}	-0.5	0

Notes.

[a] $k(T) = \alpha\ (T/300)^{\beta}\ \exp(-\gamma/T)$ cm^3 s^{-1}.

protonated counterpart. The reaction energies of the stereoisomers are quite different in each case, and can therefore lead to different chemical pathways. Structurally, the two stereoisomers of methyl formate differ in the orientation of the -CH_3O group relative to the -CHO group, with the *trans* species being 2880 K higher in energy than the *cis* species (Neill et al., 2011). The protonated versions of the *cis* and *trans* stereoisomers have similar structures to their neutral counterparts, but in this case the *trans* species is lower in energy by 2880 K. In the reaction network, the stereoisomers of both neutral and protonated methyl formate are distinguished as separate species, differing only in their label and their respective reaction rates. The overall chemistry was assumed to be the same for the two stereoisomers in each case. All reactions involving the neutral and protonated forms of methyl formate were duplicated so that a complete set of reactions was included for each stereoisomer. The gas phase reactions of each stereoisomer are shown in Table 2.5. Here, the α term in the rate coefficient expression for the *cis* conformer was used for the *trans* conformer. Dissociative recombination reactions leading to neutral methyl formate from protonated methyl formate were assumed to proceed with no conformational change (i.e. the structure of the ion is retained in the neutral product).

Only one form of methyl formate was included in the list of grain surface species, and this molecule was not distinguished as either *cis* or *trans*. However, for reactions on

Table 2.5. Gas phase reactions involving neutral and protonated methyl formate.

Reactants	Products	Rate Coefficient Terms[a]			Reference
		α	β	γ	
$CH_3OH_2^+ + HCOOH$	*cis*-$CH_3OCOH_2^+ + H_2O$	1.8×10^{-10}	-0.5	1320	1
$CH_3OH_2^+ + HCOOH$	*trans*-$CH_3OCOH_2^+ + H_2O$	1.8×10^{-10}	-0.5	0	1
$CH_3^+ + HCOOH$	*cis*-$CH_3OCOH_2^+$	1.0×10^{-11}	-1.5	0	2
$CH_3^+ + HCOOH$	*trans*-$CH_3OCOH_2^+$	1.0×10^{-11}	-1.5	0	
cis-$CH_3OCOH_2^+ + e^-$	$CH_3OH + HCO$	1.43×10^{-7}	-0.5	0	3
trans-$CH_3OCOH_2^+ + e^-$	$CH_3OH + HCO$	1.43×10^{-7}	-0.5	0	
cis-$CH_3OCOH_2^+ + e^-$	*cis*-$HCOOCH_3 + H$	7.50×10^{-9}	-0.5	0	3
trans-$CH_3OCOH_2^+ + e^-$	*trans*-$HCOOCH_3 + H$	7.50×10^{-9}	-0.5	0	
$HCOOH_2^+ + CH_3OH$	*cis*-$CH_3OCOH_2^+ + H_2O$	2.00×10^{-9}	-0.5	2810	1
$HCOOH_2^+ + CH_3OH$	*trans*-$CH_3OCOH_2^+ + H_2O$	2.00×10^{-9}	-0.5	3310	1
cis-$HCOOCH_3$	HCO+ CH_3O	5.00×10^{2}	0	0	3
trans-$HCOOCH_3$	HCO+ CH_3O	5.00×10^{2}	0	0	
C^+ + *cis*-$HCOOCH_3$	*cis*-$HCOOCH_3^+ + C$	2.17×10^{-9}	-0.5	0	4
C^+ + *trans*-$HCOOCH_3$	*trans*-$HCOOCH_3^+ + C$	2.17×10^{-9}	-0.5	0	
H^+ + *cis*-$HCOOCH_3$	*cis*-$HCOOCH_3^+ + H$	6.90×10^{-9}	-0.5	0	4
H^+ + *trans*-$HCOOCH_3$	*trans*-$HCOOCH_3^+ + H$	6.90×10^{-9}	-0.5	0	
He^+ + *cis*-$HCOOCH_3$	$HCO_2^+ + CH_3 + He$	3.54×10^{-9}	-0.5	0	4
He^+ + *trans*-$HCOOCH_3$	$HCO_2^+ + CH_3 + He$	3.54×10^{-9}	-0.5	0	
$H_2COHOCH_2^+ + e^-$	*cis*-$HCOOCH_3 + H$	1.50×10^{-9}	-0.5	0	2
$H_2COHOCH_2^+ + e^-$	*trans*-$HCOOCH_3 + H$	1.50×10^{-9}	-0.5	0	
$CH_3OH_2OCH_2^+ + e^-$	*cis*-$HCOOCH_3 + H_2 + H$	1.50×10^{-9}	-0.5	0	2
$CH_3OH_2OCH_2^+ + e^-$	*trans*-$HCOOCH_3 + H_2 + H$	1.50×10^{-9}	-0.5	0	
cis-$HCOOCH_3$	$CH_3OCHO^+ + e^-$	2.00×10^{-10}	0	2.5	3
trans-$HCOOCH_3$	$CH_3OCHO^+ + e^-$	2.00×10^{-10}	0	2.5	
cis-$HCOOCH_3$	$HCO + CH_3O$	5.00×10^{-10}	0	1.7	3
trans-$HCOOCH_3$	$HCO + CH_3O$	5.00×10^{-10}	0	1.7	
H_3^+ + *cis*-$HCOOCH_3$	*cis*-$CH_3OCOH_2^+ + H_2$	4.05×10^{-9}	-0.5	0	4
H_3^+ + *trans*-$HCOOCH_3$	*trans*-$CH_3OCOH_2^+ + H_2$	4.05×10^{-9}	-0.5	0	
H_3O^+ + *cis*-$HCOOCH_3$	*cis*-$CH_3OCOH_2^+ + H_2O$	1.81×10^{-9}	-0.5	0	4
H_3O^+ + *trans*-$HCOOCH_3$	*trans*-$CH_3OCOH_2^+ + H_2O$	1.81×10^{-9}	-0.5	0	
HCO^+ + *cis*-$HCOOCH_3$	*cis*-$CH_3OCOH_2^+ + CO$	1.55×10^{-9}	-0.5	0	4
HCO^+ + *trans*-$HCOOCH_3$	*trans*-$CH_3OCOH_2^+ + CO$	1.55×10^{-9}	-0.5	0	

Notes.

[a] For ion-molecule reactions, $k(T) = \alpha\ (T/300)^{\beta}\ \exp(-\gamma/T)$ cm^3 s^{-1}. For cosmic-ray induced photodissociation reactions, $k = \alpha\ \zeta$ s^{-1}, where ζ is the cosmic-ray ionization rate. For direct photodissociation reactions, $k = \alpha \exp(-\gamma A_v)$ s^{-1}.

References. (1) Neill et al. (2011); (2) Garrod and Herbst (2006); (3) Garrod et al. (2008); (4) taken from the OSU gas phase network.

Table 2.6. Grain surface reactions producing gas phase methyl formate.[a]

Reactants	Products	Scaling for the Rate Coefficient Term α
s-H + s-CH_3OCO	*cis*-$HCOOCH_3$	1
s-H + s-CH_3OCO	*trans*-$HCOOCH_3$	10^{-25}
s-HCO + s-CH_3O	*cis*-$HCOOCH_3$	1
s-HCO + s-CH_3O	*trans*-$HCOOCH_3$	10^{-25}
s-$HCOOCH_3$	*cis*-$HCOOCH_3$	1
s-$HCOOCH_3$	*trans*-$HCOOCH_3$	10^{-25}
cis-$HCOOCH_3$	s-$HCOOCH_3$	1
trans-$HCOOCH_3$	s-$HCOOCH_3$	10^{-25}

Notes.

[a] The prefix "s-" denotes a grain surface species.

surfaces that produce gas phase methyl formate, the reaction was duplicated in the same manner as the gas phase reactions so that both stereoisomers could be included. The rates for those reactions involving the *trans* stereoisomer were scaled using a Boltzmann factor based on the energy difference between the two stereoisomers and assuming a temperature of 50 K. This temperature was selected because GWWH08 showed that the heavy radicals involved in these reactions become mobile on the grain surface and react in the 30–70 K temperature range. As is shown in Table 2.6, the values of the α term in the rate coefficient expression for the grain surface reactions involving the gas phase *trans* species were therefore scaled by 10^{-25} [i.e. $e^{-(2880K/50K)}$] with respect to the reactions involving the gas phase *cis* species. Only grain surface reactions that involved one gas phase molecule were included in the model, following the convention used in previous modeling studies (Garrod et al., 2007).

Results and Discussion

The results of the trials including the new gas phase routes to form methyl formate (i.e. Routes 1 and 2) are shown in Figures 2.4 and 2.5. Figure 2.4 shows the peak fractional

abundances for COMs using both the B_Standard_S and the S_Methoxy_S BRs, both with and without the new gas phase reactions, compared to the abundances observed in Sgr B2(N-LMH). The inclusion of the new gas phase formation routes for methyl formate yield no change in the model predictions for the peak abundances for any trials.

Detailed analysis indicates that no changes occur for the *cis*-methyl formate abundance when Routes 1 and 2 are included, regardless of temperature, although the results from trials including these new gas phase reactions do indicate that *trans*-methyl formate should be an abundant molecule in hot cores. The time evolution plot of Figure 2.5 reveals that at $T < 55$ K, gas phase *trans*-methyl formate is slightly higher in abundance than gas phase *cis*-methyl formate because it is formed in the gas via Route 2. In the range $T = 55$–100 K, *cis*-methyl formate is produced via grain surface chemistry, and this formation route dominates its formation over the new gas phase routes. The gas phase *cis*-methyl formate abundance peak occurs at $T \approx 80$ K; at this temperature the $^{cis}/_{trans}$ relative abundance ratio is 2.3×10^8. Above 100 K, the grain surface production routes to methyl formate no longer contribute significantly to the *cis*-methyl formate gas phase abundance. The gas phase abundance of *trans*-methyl formate begins to rise dramatically at these higher temperatures because of its formation via Route 2, while the gas phase abundance of *cis*-methyl formate decreases gradually as it is destroyed through gas phase processes and is no longer replenished via grain surface chemistry. The two conformers begin to approach a similar gas phase abundance at higher temperatures and long timescales, and the $^{cis}/_{trans}$ relative abundance ratio is $\sim$3 at $T = 200$ K.

Although the peak abundances do not change when Routes 1 and 2 are included, small changes are observed in the time evolution plots for formic acid and acetic acid. These changes arise from the adjustment of the protonated formic acid dissociative recombination rates reflected in Table 2.3. The formic acid abundance in the gas phase increases at temperatures below 100 K because the rate of its formation via Reaction 2.4 is increased over the rate used in GWWH08. This results in an increase in formic acid abundance on

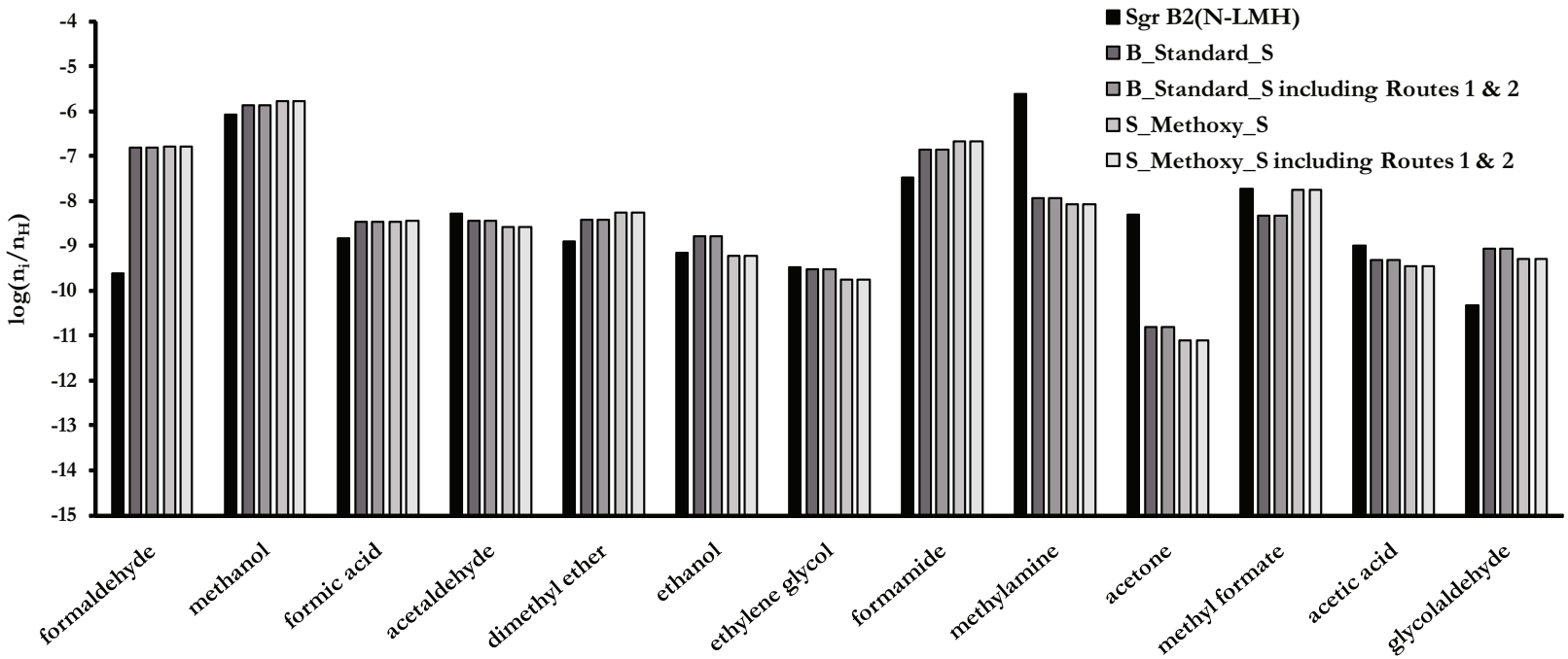

Figure 2.4 – Peak fractional abundances for a variety of interstellar species, comparing the observationally-determined values for Sgr B2(N-LMH) (as referenced in GWWH08) to the B_Standard_S and S_Methoxy_S branching ratio trials both before and after the addition of Routes 1 and 2 to the network.

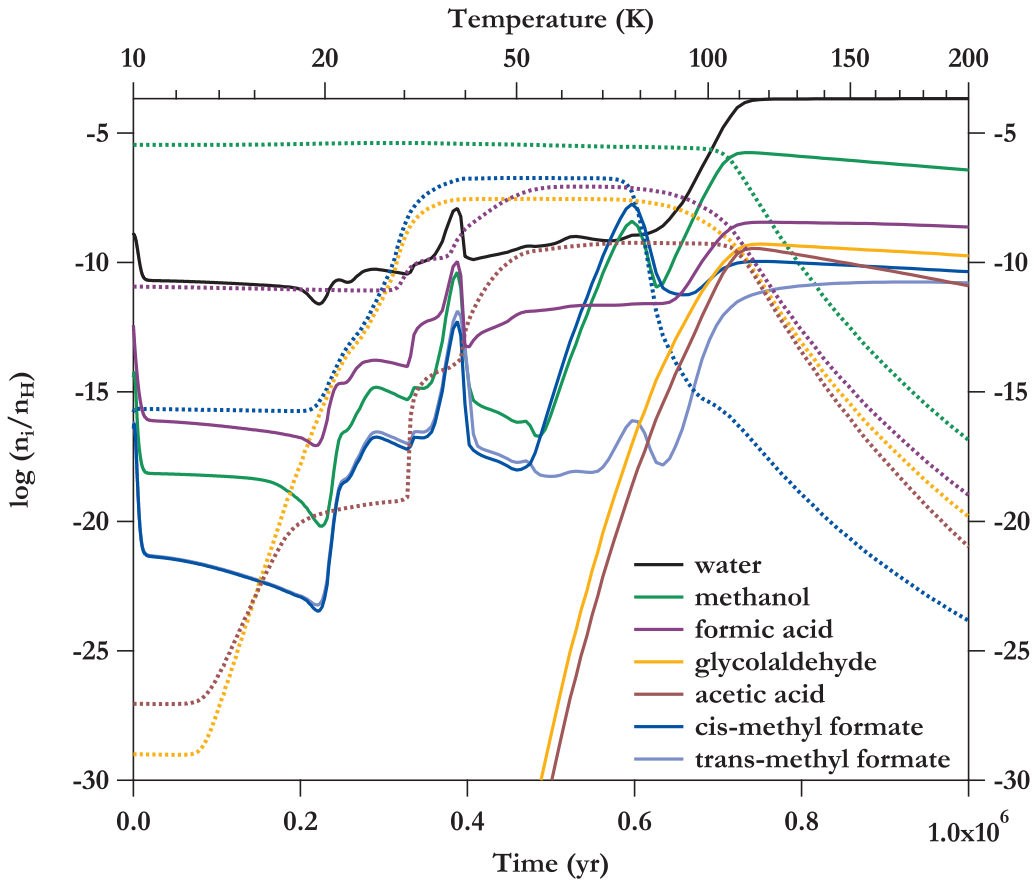

Figure 2.5 – Time and temperature evolution of the $C_2H_4O_2$ species and other highly-abundant molecules for the S_Methoxy_S trial that incorporates Routes 1 and 2. The dotted lines show the evolution of the grain surface species, while the solid lines show the gas phase species.

the grain (via accretion of the gas phase neutral) and acetic acid abundance in the gas (via its formation from formic acid in grain surface reactions and subsequent evaporation). No change is observed at $T > 100$ K between the two sets of trials (i.e. with and without Routes 1 and 2) for any species examined here other than *trans*-methyl formate.

The methyl formate stereoisomers can be used as a gauge of the validity of the gas-phase chemistry examined in this model, as *trans*-methyl formate should be observable in the Sgr B2(N-LMH) source if it forms from the mechanisms included here. Its presence will also allow a test of the physical model assumed for comparison to Sgr B2, as the abundance ratios directly probe the temperature at which methyl formate is released from grains. The fractional abundance of *cis*-methyl formate in Sgr B2 is 1.9×10^{-8}. The

expected thermodynamic ratio between the two isomers is $\sim 10^{-25}$ [i.e. $e^{-(2880K/50K)}$], but the model predicts the fractional abundance of *trans*-methyl formate to be 1×10^{-11} at high temperatures (i.e. $T > 100$ K) and long timescales. The rotational spectrum of *trans*-methyl formate has now been recorded up to 60 GHz, and initial observational searches indicate its presence in Sgr B2—though only in absorption (Neill et al., 2012). No quantitative information about its temperature or abundance is yet available. Additional higher frequency laboratory studies are desired before its physical properties in a hot core can be probed.

In addition to using stereoisomers as probes of the chemistry and physics included in this model, the model now provides predictions for ion abundances that are based on a more realistic chemical network. Imaging observations that compare the distribution of these ions to their neutral counterparts could reveal their role in the chemical processing of material in hot cores. A direct spatial correlation between the ion and its neutral counterpart might indicate formation of the neutral species from the electron recombination reactions of its protonated counterpart. If an anti-correlation is observed, however, then the conclusion could be drawn that the neutral forms from grain chemistry, and is subsequently ionized in the gas phase after release from the grain. Regardless, these species hold great promise for unveiling the true chemical mechanisms leading to the formation and destruction of COMs in interstellar clouds. The peak fractional abundances predicted for protonated methanol (2×10^{-11}) and protonated *cis*-methyl formate (8×10^{-11}) indicate that both of these ions should be observable in the Sgr B2 source. The predicted peak fractional abundances for protonated formic acid (1×10^{-13}) and protonated *trans*-methyl formate (6×10^{-14}) indicate that detection of these ions will be observationally challenging.

2.2.3 Conclusions

Several modifications have been made to the gas/grain code of GWWH08 to explore the influence of additional grain surface and gas phase chemical pathways on methyl formate

and its structural isomers acetic acid and glycolaldehyde. The following conclusions can be drawn from this study:

1. The direct and cosmic-ray induced photodissociation BRs for methanol on grain surfaces do influence the peak abundances of the $C_2H_4O_2$ isomers, but the gas phase methanol photodissociation BRs ultimately have no influence over the peak abundances for these species. The methanol photodissociation BRs that favor the methoxy radical channel most closely match observations for methyl formate. These BRs qualitatively agree with gas phase laboratory measurements. However, the BRs that favor the methyl channel give more reasonable matches to the observed acetic acid and glycolaldehyde abundances. Regardless, the set of BRs giving the worst agreement with the Sgr B2(N) abundances is that favoring the hydroxymethyl channel, which stands in contrast to the results from recent laboratory studies where this channel was suggested to dominate methanol ice photodissociation. Additional laboratory studies that directly measure the BRs for each product are required to provide the quantitative information necessary for the modeling studies.

2. The warm-up timescale largely influences the chemistry of these species, and a combination of the grain surface methanol photodissociation BRs and warm-up timescale can be used to adjust the peak fractional abundances to better match observations. However, it is difficult to accurately estimate the appropriate warm-up timescale and temperature evolution model to be used for any given source. Additionally, single-dish observations include the full source and probe everything from the warm, compact regions near the star to the cold, extended regions where little gas phase processing has occurred. It is therefore likely that the physical model assumed in this study is much too simple to allow more than single-temperature comparisons to observations. More sophisticated hydrodynamic models incorporating this chemistry are needed before more conclusions can be drawn as to the influence of the physics on the chemistry.

3. Addition of the Fischer esterification reactions and the *trans* stereoisomer of methyl formate does not change the predicted peak abundance for *cis*-methyl formate. From 55–100 K, *cis*-methyl formate is predominantly formed via grain surface chemistry. At higher temperatures, the reaction between protonated methanol and formic acid (Route 2) favors the production of *trans*-methyl formate. This indicates that *trans*- and *cis*-methyl formate may be spatially segregated, and that the *trans*-conformer may be most abundant in the hot, compact region of the core. The gas phase reaction cycle leading to *trans*-methyl formate relies upon the dominant channel for the dissociative recombination of protonated methyl formate to be the production of methanol, which leads to protonated methanol and drives the formation of *trans*-methyl formate via Route 2. Investigation of the dissociative recombination process for protonated methyl formate would greatly aid in evaluating this proposed mechanism. Observational searches for *trans*-methyl formate would also be helpful in fully evaluating the accuracy of the chemical network used in the model.

4. Glycolaldehyde is overproduced by the model at high temperatures and long timescales when compared to its Sgr B2(N-LMH) abundance. However, the abundance predicted by the model at $T = 100$ K more closely matches observations. Significant quantities of glycolaldehyde are being evaporated from the grain surface at this temperature in the model, and so this is a reasonable comparison for the glycolaldehyde abundance in the outer envelope of the hot core, where shocks may have liberated it from the grains. Explicit, detailed models of shock chemistry are required to quantitatively explain extended shock-induced gas phase glycolaldehyde. Glycolaldehyde has been detected in three sources, Sgr B2 (Hollis et al., 2000), G31.41+0.31 (Beltrán et al., 2009), and IRAS 16293-2422 (Jørgensen et al., 2012), with only the former detection offering a full determination of its temperature and abundance. More observational studies of glycolaldehyde are required so that its chemistry can be fully investigated. If it is indeed a cold, extended molecule, then its observed abundance

might be more directly tied to the grain surface abundance than its structural isomers, which are formed in or ejected into the hot gas. However, its absence from the warm hot core gas is puzzling, as it should be present in even higher abundance in these regions. Other gas phase destruction mechanisms may be required to explain the behavior glycolaldehyde of hot core sources.

5. These results point to a path forward for additional observational studies of methyl formate and its structural isomers, glycolaldehyde and acetic acid. These three structural isomers must be observed in a variety of sources with varying physical conditions to allow direct comparison with the model predictions. If all three molecules indeed form primarily from grain surface chemistry, then acetic acid and glycolaldehyde should also be present in regions of grain mantle disruption where methyl formate has already been observed.

6. The predictions from this model indicate that the protonated forms of methanol and *cis*-methyl formate should be observable in high-mass hot cores. Observational studies that compare the spatial distributions of the ions to their neutral counterparts would offer clues to the dominant formation and destruction mechanisms for COMs in interstellar clouds. Laboratory and observational searches for these two ions are required before direct comparison with the model can be made.

2.2.4 Impact and Future Work

Several relevant lab and observational studies have been conducted since these modeling studies were published. The results of these studies are summarized here.

Laboratory Measurements for Formic Acid Revisited

Cole et al. (2012) have recently reported laboratory measurements on the Reactions 2.2 and 2.6. They have confirmed the report by Feng and Lifshitz (1994) that only proton-transfer

occurs for Route 1. They have also determined that formation of both the adduct ion and protonated methyl formate dominates Reaction 2.6, which is in contrast to the previous report by Freeman et al. (1978a), and validates the most important assumption that was made for the modeling study discussed above. Another point that deserves attention is the rate constant measured for Reaction 2.2. The observed rate coefficient for the formation of protonated methyl formate (Cole et al., 2012, Table 1) was found to be a factor of $\sim$10 lower than what was estimated in the modeling study above. This should have the effect of significantly reducing the total abundance of *trans*-methyl formate due to its gas-phase formation from Route 2, as well as reducing the ratio of *trans*-to-*cis* of the stereoisomers.

Astronomical Observations

The original *ab initio* study by Neill et al. had been inspired by spatial distributions of *cis*-methyl formate and methanol, particularly the observed anti-correlation of each species' abundance. The authors had also reported preliminary detections of *trans*-methyl formate, though, at the time, there was not yet enough laboratory data to allow a thorough analysis of its interstellar detection. More recently, Neill et al. (2012) have reported the FTMW rotational spectrum (up to $J = 10$) and a systematic interstellar search (up to $J = 4$) of *trans*-methyl formate within the publicly available GBT PRIMOS survey. The simultaneous observation of absorption features for both the A- ($J_{K_aK_c} = 2_{11} \leftarrow 1_{10}$) and E-state ($J_K = 2_{-1} \leftarrow 1_{-1}$) provided an estimate of the excitation temperature to be 7.6 ± 1.5 K. Such a temperature is much lower than what is predicted by the model if one compares to the gas/dust temperature at which the abundance peaks. The fact that only absorption features could be observed means that the interstellar detection of *trans*-methyl formate still remains to be explored in greater detail.

Interferometric observations of dimethyl ether (CH_3OCH_3) have revealed a close similarity between its distribution and that of methyl formate, even at high spatial resolutions (Widicus Weaver and Friedel, 2012; Brouillet et al., 2013). These observational studies pro-

vide tight constraints for a more comprehensive model of both species, particularly since it has been speculated that both share common formation precursors.

Warm-up Timescales

Given the importance of the influence of the warm-up timescale for the relative abundances of the $C_2H_4O_2$ isomers, an important area of focus for future models of complex chemistry will be uncovering the details of the difference in physics of high- vs low-mass cores. Methyl formate and many other COMs have now been detected toward a number of hot corinos (Bottinelli et al., 2004a,b; Öberg et al., 2010), yet it remains uncertain exactly how the warm-up timescale in these protostars differs from those of their high-mass counterparts. As is summarized by Garrod and Widicus Weaver (2013, §7.7), some authors suggest that low-mass cores spend longer times at moderately elevated temperatures, whereas others suggest the opposite. More comprehensive observing observational surveys in which relative abundances of various molecules may help to clarify this discrepancy.

COMs in Protoplanetary Disks

To explore the extent of COMs in protoplanetary disks, a collaboration was initiated that incorporates the OSU gas/grain network discussed above, as well as a set of gas-phase reactions with energy barriers that are relevant for modeling interstellar environments at temperatures up to $\sim$1000 K (Harada et al., 2010, 2012), into the astrochemical code presented in Walsh et al. (2010, 2012). This physical model describes the protoplanetary (i.e. accretion) disk surrounding a classical T Tauri star, and includes a number of photo-processes (UV, X-ray emission from the central protostar), as well all the grain surface processes considered in Garrod et al. (2008).

A model of COMs in such a disk is particularly relevant in the current age of planetary science, when thousands of exoplanets have recently been detected with the NASA *Kepler* mission (Howell, 2013), and the ALMA observatory has been constructed and is reaching

its full potential for probing extraterrestrial environments at unprecedented spectral sensitivities and spatial resolutions. While the specific details of Walsh et al. (2014) are not included here, a summary of the main result relevant to the work discussed above is provided. This study showed that COMs can be produced efficiently within the disk midplane at a level sufficient to provide peak gas phase fractional abundances up to 10^{-6}–10^{-4}. This is despite the higher radiation fields that are experienced even in the disk midplane, which is highly shielded compared to the disk surface. While the mechanism that produces these relatively high COM abundances is not entirely equivalent to that included in models of hot cores/corinos, these results do indicate that grain surface chemistry may indeed play a crucial role in forming complex molecules in disks. Fragmentation chemistry of intermediate-size molecules may then play an important role in the specific relative abundances of larger species such as the $C_2H_4O_2$ isomers.

This study was particularly aimed at preceding—and thus guiding—initial full-science observational surveys of star-forming regions with ALMA. It is anticipated that reports of recent and/or near-future observations will be able to immediately test the validity of such a physicochemical model of complex chemistry in protoplanetary disks. This may then enable more detailed studies of the complex organic chemistry such as the ones presented above.

Chapter 3

Laboratory Spectroscopy

3.1 Background

The laboratory work presented here is motivated by the desire to study the photodissociation dynamics of organic molecules that drive complex interstellar chemistry. As is previously discussed in Chapter 2, methanol photodissociation is an important process in interstellar chemistry, yet there are many unknowns that remain regarding its dissociation chemistry. It is thus crucial that laboratory measurements be made specifically on the BRs of methanol photodissociation and the spectral features of its dissociation products. Below, I present the design, construction, and use of a spectrometer for this purpose.

The first part of the work presented in this chapter discusses a proof-of-concept study to verify that highly-reactive dissociation products can be generated using these methods, and that the spectral technique is of sufficient sensitivity to quantify these products with respect to the parent molecule. I describe the implications of these findings for future studies of dissociation mechanisms in the context of interstellar chemistry.

In the second part of this chapter, I present various applications of the spectrometer to chemical systems of interest that are related to methanol photodissociation. I begin first with initial spectral studies attempting to detect UV-induced methanol photodissociation products. I then present two spectral searches for the mm/submm rotational features of the

radicals hydroxymethyl and methoxy. Lastly, I discuss other techniques that could be used in conjunction with this experimental technique to provide a more complete understanding of dissociative reaction dynamics.

3.2 Design & Benchmarks of a mm/submm Spectrometer

Note. Much of the work presented herein (§3.2) can be found in the following publication:

Jacob C. Laas, Brian M. Hays, and Susanna L. Widicus Weaver. *The Journal of Physical Chemistry A*, **2013**, *117*(39):9548–9554.

3.2.1 Background

Spectroscopic and mass spectrometric techniques are widely used for state-selective measurements on molecular reactants and products during dissociation reactions. Such studies are critically important to the field of astrochemistry, where the dissociative reaction dynamics of small organic molecules dictate the formation of key reaction intermediates such as organic radicals and ions. These small reactive species are the drivers of organic chemistry in interstellar environments through both condensed-phase chemistry on ice surfaces in dense molecular clouds, and gas-phase chemistry in star- and planet-forming regions (Garrod et al., 2008). Therefore, a full quantitative understanding of radical and ion formation, including product energies and branching ratios, is required to guide accurate astrochemical modeling of these interstellar environments. Surprisingly, while rotationally-resolved spectroscopic methods are often used in reaction dynamics studies (Butler and Neumark, 1996), very few experiments utilize pure rotational spectroscopic techniques. A few reaction dynamics studies of organic molecules have been conducted using microwave and millimeter spectrometers (Dian et al., 2008; Kolbe and Leskovar, 1985; Duffy, 2005), but to our knowledge, no reaction dynamics studies have yet utilized rotational spectroscopy at higher frequencies within the THz spectral range.

The THz spectral range, also known as the far-infrared (FIR) or submillimeter region, lies between the microwave and infrared spectral windows and includes frequencies from 100 GHz to 10 THz (3–300 cm^{-1}). Rich molecular information can be accessed by THz studies, including the pure rotational signatures of small molecules, the low-frequency vibrational modes of large molecules, and the complex spectral signatures associated with molecular internal motion. The present work focuses on the application of THz spectroscopy to high-resolution pure rotational spectroscopy. This approach offers a unique opportunity for the study of chemical mechanisms like the dissociation reactions of small organics because it probes structure-specific spectral fingerprints, enabling the direct detection of reactive species. The structure specificity of rotational spectroscopy is particularly valuable for the study of organic molecules, where dissociation mechanisms may involve many separate channels in which products have either overlapping spectral signatures in other wavelength ranges, or equal masses that preclude mass spectrometry studies. Any dissociation product that has a permanent dipole moment can be probed using rotational spectroscopy.

3.2.2 Experimental Methods

Our initial studies have applied a multipass millimeter/submillimeter direct absorption spectrometer to the investigation of the methanol dissociation mechanism. A schematic diagram of this setup is shown in Figure 3.1. Below I present in more detail each major component.

Signal Generation

The millimeter/submillimeter signal was generated by multiplication of the output signal from an analog signal generator (Agilent Technologies, E8257D PSG with the options 1EA, UNU, 550, and UNT). The output signal was frequency modulated at 15 kHz and then multiplied to the appropriate frequency range using a custom-built frequency multiplier

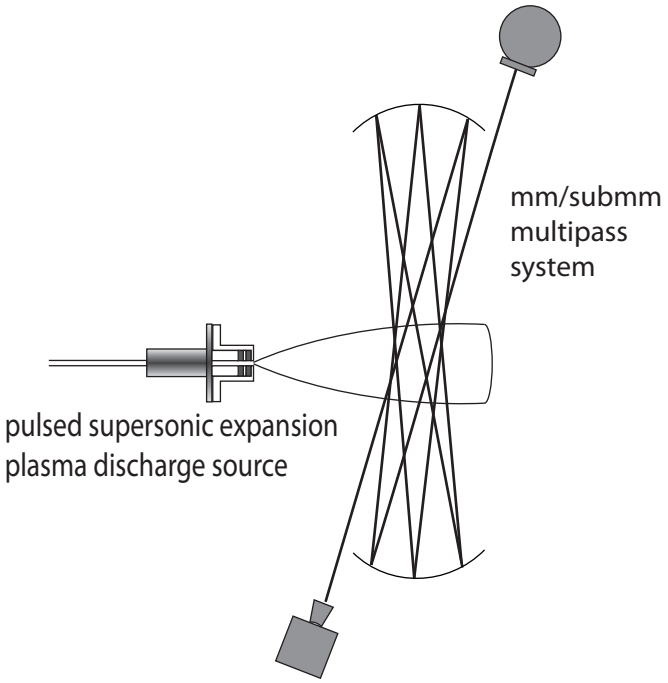

Figure 3.1 – Schematic of the multipass spectrometer coupled with the supersonic expansion discharge source.

extender kit (Virginia Diodes, Inc.). This multiplier chain has several sets of multipliers and power amplifiers, enabling full frequency coverage from 50 - 1000 GHz. The specific components used in the experiments described here included a WR8x3 tripler plus a W-Band power amplifier with a frequency output of 90–140 GHz, and a WR10 tripler and W-Band power amplifier driving a WR5.1 doubler with a frequency output of 140–220 GHz.

Supersonic Expansion

The gas-phase spectroscopic study of reactive species as is required in dissociative reaction dynamics studies necessitates the use of a supersonic expansion source combined with a suitable production technique for the molecule of interest—i.e. dissociation of a precursor molecule using a UV lamp, laser, or high-voltage plasma discharge. At sufficiently low sample concentration relative to the inert carrier gas, the supersonic expansion can be used to both quench the excess energy of the dissociation products and to reduce recombina-

tion reactions. This enables the spectroscopic interrogation of products while minimizing additional complications from excited vibrational states and further reactions. Rotational temperatures of $T_{rot} < 20$ K are typical for medium- to small-sized organics.

Sample Preparation

Methanol (Fisher Scientific, Certified ACS solvent grade, 99.9%) was diluted to $\sim$1% in argon carrier gas (NexAir, ultra-high purity) by passing the carrier gas through a glass bubbler containing the liquid methanol sample at room temperature, and then diluting this mixture with additional argon. In this way, an approximate concentration of 1–2% can be estimated from

$$Conc. \approx \frac{P_{vap}}{P_{tot}} \frac{F_{bub.}}{F_{bub.} + F_{pure}}, \tag{3.1}$$

where P_{vap} is the vapor pressure, P_{tot} is the total pressure of the sample gas line, $F_{bub.}$ is the flow rate of Ar through the bubbler, and F_{pure} is the flow rate of the pure Ar that is used to dilute the gas sample. The flow rates of each gas line were controlled using dedicated mass-flow controllers (MKS).

A pulsed valve (Parker Hannifin, Series 9) introduced the methanol/argon mixture into a vacuum chamber through a 1 mm pinhole nozzle; a nozzle backing pressure of 0.5–1 bar was used. The plasma discharge source that was attached to the front of the pulsed valve is described in more detail below. After dissociation, the gas mixture was expanded adiabatically into the chamber. The pulsed nozzle was set to a repetition rate of 18 Hz with an on duration of 5 ms. A combined rotary vane + roots blower pumping system with an effective pumping speed at the valve of $\sim$250 L s^{-1} was used to maintain a chamber pressure of 30$\pm$5 mTorr. These operating conditions were found to give the best compromise between signal strength and sample cooling.

High-voltage Plasma Discharge Source

A plasma discharge source based on the design of McCarthy et al. (2000) was used to dissociate methanol. An auto-ignited plasma was generated between two electrodes in the throat of the expansion during each valve pulse. Teflon spacers were used to separate the first electrode from the valve faceplate by a distance of 2.5 cm. Both electrodes were 0.25 cm thick, and they were separated by a 1 mm-thick Teflon spacer. The electrode closest to the valve was made of copper and was held at ground, while a potential of +600 V was applied to the outer electrode made of stainless steel using a high-voltage power supply (Spellman HV Electronics Corp., SL2000). The gas mixture passed through an additional 0.23 cm long channel formed by the Teflon housing before being expanded into the vacuum chamber. A discharge current of $\sim$27 mA was maintained using a ballast resistor of 10 kΩ in series with the source. A schematic and image of this discharge can be found in Figure 3.2.

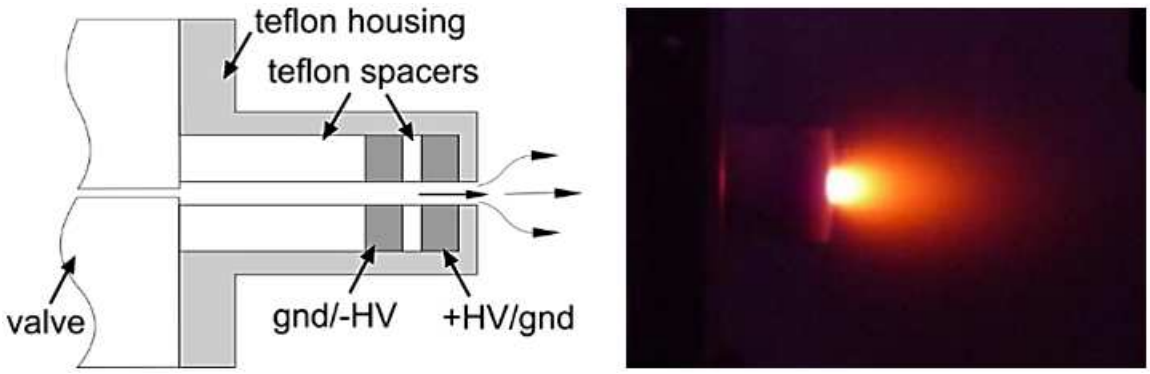

Figure 3.2 – Schematic diagram of discharge (left) and image of the discharge source igniting a mixture of Ar & CH_3OH (right).

Millimeter/Submillimeter Optics

The use of such supersonic expansion sources complicates THz spectroscopy experiments. While the adiabatic cooling offered by supersonic expansions yields an increase in line strength due to a reduction in the molecular partition function, the pathlength through the sample is significantly reduced when compared to the long-pathlength direct absorption

techniques commonly used in this frequency range. The already weak signals from trace amounts of sample, combined with this shortened pathlength, limit the application of this approach for reaction dynamics studies. Therefore, advancements in pure rotational studies as applied to reaction dynamics rely upon increasing the sensitivity of THz spectrometers beyond the standard direct absorption technique. There have been a few efforts to extend cavity-enhanced spectral techniques into this frequency range (Gopalsami et al., 2002; De Lucia, 2010; Braakman and Blake, 2011), but implementation is challenging because of limitations in appropriate hardware. A straightforward alternative method for increasing spectral sensitivity is to increase the optical pathlength through the sample using an optical arrangement that provides multiple passes while minimizing optical loss factors.

To this end, we have adopted the optical design of Kaur et al. (1990) used at visible/infrared wavelengths, which was specifically designed for application to molecular beams due to its minimally-sized interaction region. While a similar optical design has been used for THz spectroscopy at much higher frequencies ($>$1.8 THz) (Schmuttenmaer et al., 1990), we have further extended this design to lower frequencies, enabling studies of a variety of polyatomic organic molecules that have strong spectral signatures at frequencies in the 100 GHz to 1 THz range. We have coupled this spectrometer with a high-voltage plasma discharge supersonic expansion source to study the methanol dissociation mechanism. The output radiation from the multiplier was coupled into the multipass optical setup using a standard waveguide horn. The THz radiation was aligned in the multipass arrangement described by Kaur et al. (1990); spherical mirrors having a 7.62 cm diameter and focal length (Edmund Optics, NT32-824) and spaced at a distance of 28.5 cm were used to produce 7 optical passes in the vacuum chamber. The number of passes was limited by the power lost ($\sim$90%) from clipping the large beam at the edges of the spherical mirrors. The "beam waist" region of the optical path crossed the center of the expansion $\sim$2.5 cm downstream from the dissociation region, oriented such that the optical path was parallel to the benchtop and in-plane with the centerline of the gas expansion. This orientation ensured

that all optical passes crossed the molecular beam in the coldest part of the expansion.

Also, prior to entry into the vacuum chamber and multipass cell, PTFE lenses were used to focus the beam so that its beam radius is as small as realistically possible and so that its focal point meets in the center of the multipass cell. The details of these lens solutions can be found in Appendix A.

Signal Detection

The output signal from the multipass cavity was monitored with a zero-bias diode detector that was matched in frequency response to the corresponding multiplier chain (Virginia Diodes, Inc., WR8.0 ZBD and WR5.1 ZBD). The output signal from the detector was processed by two digital lock-in amplifiers (Stanford Research Systems, SR810 and SR830), the first of which was locked to the modulation frequency of the input radiation, and the second of which was locked to the trigger signal from the pulsed valve driver. The output signal intensity was recorded as a function of frequency using a computerized data acquisition routine. The spectral resolution of $\sim$30 kHz is controlled by the frequency point spacing, which is set to resolve spectral linewidths of approximately 300 kHz. Amplitude modulation was used to measure the relative power from the multiplier across the spectral ranges covered in the experiment, and all spectra were power-normalized before analysis.

3.2.3 Methanol Dissociation Dynamics as a Case Study

Our reaction dynamics experiments rely on the structure-specificity of THz spectroscopic measurements. Therefore, the critical first step in any such study is to obtain a general overview of the chemistry involved in the reaction mechanism, so that the necessary structural information for each target molecule can be sought to guide the laboratory investigations. We summarize here the available information concerning the methanol dissociation mechanism that pertains to a rotational spectroscopic study.

Several theoretical studies of methanol dissociation have determined the stationary

points and transition states for the pathways involved in the dissociation mechanism (Xia et al., 2002; Ing et al., 2003; Chang and Lin, 2002, 2004). All the dissociation channels shown in Equation 1.1 have been shown to be energetically accessible within a range of $\sim$30 kcal/mol (Chang and Lin, 2002, 2004). It is therefore likely that all of these channels play a role in the experiments presented here.

There have been a number of gas phase laboratory studies of methanol photodissociation (Hoch and Patat, 1935; Fricke and Hart, 1936; Farkas and Hirshberg, 1937; Porter and Noyes, Jr., 1959; Hagege et al., 1968; Satyapal et al., 1989; Harich et al., 1999a,b; Chen et al., 2011). However, none of these studies have clearly distinguished between the CH_2OH and CH_3O channels while also determining quantitative branching ratios. Some estimates of the methanol photodissociation branching ratios from experiments on interstellar ice analogs do exist (see e.g. Öberg et al., 2009). Thus no complete studies of methanol dissociation pathways have been conducted under conditions relevant to astrochemistry in the condensed or gas phase. It is generally agreed that either the CH_2OH or CH_3O channel dominates in methanol dissociation reactions.

Traditional mass spectrometric techniques prove difficult for a methanol dissociation study because neither the CH_2OH versus CH_3O channels nor the CHOH versus H_2CO channels can be distinguished. However all of these product channels have strong THz spectral signatures. The pure rotational spectrum of the CH_3O radical has been characterized for select transitions up to 900 GHz (Endo et al., 1984; Momose et al., 1988). The H_2CO rotational spectrum has been characterized up to 2.6 THz (Bocquet et al., 1996; Brünken et al., 2003). The OH rotational spectrum has been characterized up to 4 THz (Beaudet and Poynter, 1978; Blake et al., 1986; Farhoomand et al., 1985; Brown et al., 1986), but the rotational lines that fall within the range of our spectrometer are too weak to detect by these methods. No rotational spectrum is available for CHOH, and only infrared spectroscopic data are available for CH_2OH (Feng et al., 2004; Roberts et al., 2013). Because of the limited availability of rotational spectra for all channels, our initial experiments

have focused on the CH_3O and H_2CO products.

3.2.4 Results and Analysis

Methanol spectra comparing the SNR of a single-pass optical arrangement and that of the multipass spectrometer are shown in Figure 3.3. As expected, the seven-fold increase in pathlength increased the SNR of the spectrum by up to a factor of $\sim$5; additional increase in SNR was limited by power loss in the probe beam. This power loss was also observed by Schmuttenmaer et al. (1990), who worked with a similarly sized THz beam. The relative intensities of the lines between the two spectra indicate that the temperature of the gas probed by the single-pass and multi-pass setups is similar in value.

The density and temperature of a molecule in a gas sample can be determined using a Boltzmann diagram analysis based on the integrated intensity of the observed spectral lines. This analysis approach adopts the convention used in radio astronomy, where the integrated intensities of the spectral lines, $\int_{-\infty}^{\infty} I_b dv$, and their corresponding energy levels, E_i, are related by

$$\int_{-\infty}^{\infty} I_b dv = \frac{hc^3 A g_i}{8\pi k \nu^2} \frac{N_T}{\Phi(T_{rot})} \, e^{-E_i/kT_{rot}}, \tag{3.2}$$

where h is Planck's constant, k is Boltzmann's constant, c is the speed of light, A is the Einstein A-coefficient for the transition, g_i is the state degeneracy, ν is the transition frequency, N_T is the column density, $\Phi(T_{rot})$ is the rotational partition function, and T_{rot} is the rotational temperature. In an absorption experiment such as the one conducted here, the Einstein A-coefficient used in Equation 3.2 must be converted to the Einstein B-coefficient through the relationship

$$A_{1\to 0} = B_{1\leftarrow 0} \frac{8\pi h \nu^3}{c^3}, \tag{3.3}$$

to account for the conversion from spontaneous emission to absorption. The upper state en-

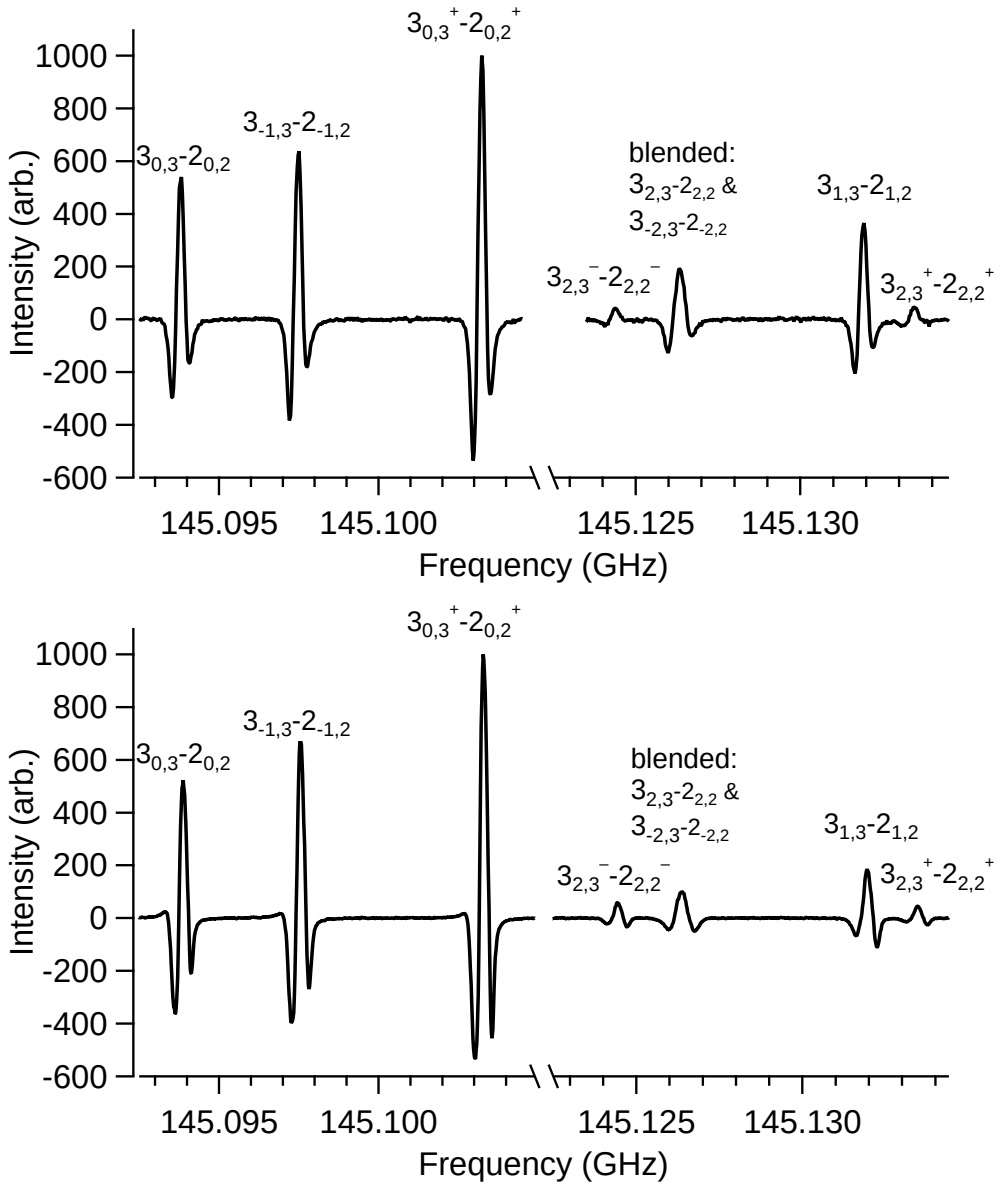

Figure 3.3 – Comparison of methanol spectra using a single pass optical configuration (top) and a multipass optical configuration (bottom). Methanol transitions are labeled with the corresponding quantum numbers.

ergies and degeneracies are conventionally used. Thus, a plot of $ln\left[\left(\int_{-\infty}^{\infty} I_b dv\right)\left(k/(h^2 \nu B g_u)\right)\right]$ versus E_u gives a line with slope inversely proportional to T_{rot} and with intercept equal to $ln(N_T/\Phi(T_{rot}))$. A weighted least squares approach is used for the linear regression analysis. The uncertainties of the integrated intensities are derived using standard error propagation from the 1-σ standard deviation of the noise observed in the power-normalized

spectrum and the frequency point spacing. The intensity scale for this experiment is not calibrated absolutely, precluding quantitative determination of the density. Nonetheless, the integrated intensity of each line is proportional to the product of the peak intensity and the linewidth at the zero-crossing points for the 2f lineshape. Using this approximation, relative abundance ratios can be determined even without absolute intensity calibration by taking the ratio of the intercepts from the Boltzmann diagrams for two species.

The Boltzmann diagram for methanol determined from the bottom spectrum of Figure 3.3 is given in Figure 3.4. The rotational temperature of methanol in the multipass setup as determined from this analysis is 9.6 ± 0.6 K. The strong linear correlation ($R^2 = 0.94$) shows that thermodynamic equilibrium is a reasonable approximation for the molecules probed in the expansion. As this experiment is designed to measure the branching fractions of the dissociation products, all product abundances are referenced to the ground vibrational state of methanol. Therefore, the methanol spectrum was reacquired and the Boltzmann analysis was repeated at a minimum of once per day, ensuring that day-to-day fluctuations in the methanol density were properly accounted for when relative abundances were determined.

In order to test the spectrometer sensitivity and detectability of products, searches were conducted for methanol dissociation products using a high-voltage plasma discharge source. This approach was used in a recent experiment that utilized both laser induced fluorescence and millimeter wave spectroscopy (Melnik et al., 2011), where the CH_3O and H_2CO products were observed. The CH_3O and H_2CO were similarly observed in the present work as products of methanol dissociation. Sample spectra showing rotational lines of each dissociation product are shown in Figures 3.5 and 3.6. In total, 5 lines each of CH_3O and H_2CO were detected. The number of observed lines was limited by the frequency coverage of the multiplier chain that was in use for this particular experiment, but provided a sufficient number of transitions to enable a full Boltzmann analysis to be performed. Between 20 and 600 spectral scans were averaged for each observed product line in order

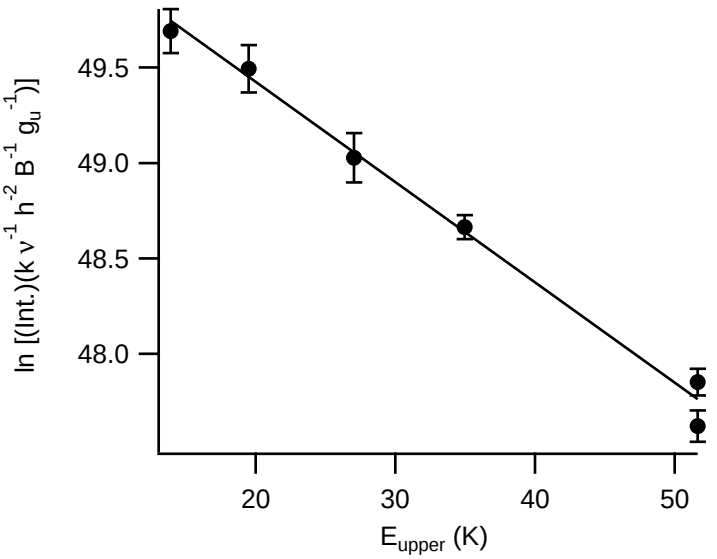

Figure 3.4 – Boltzmann diagram for methanol based on the bottom spectrum shown in Figure 3.3, where "Int." is the integrated intensity approximated as the product of the peak intensity and the linewidth at the zero-crossing points for the 2f lineshape.

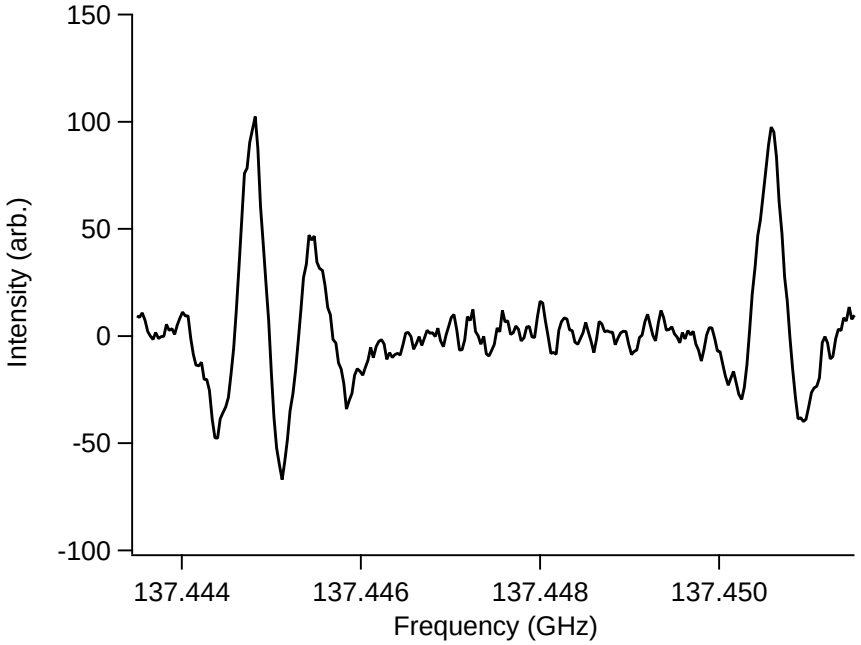

Figure 3.5 – Spectrum of CH_3O detected using a plasma discharge source acting on a methanol/argon mixture.

to increase the SNR and obtain accurate line intensity information for determination of percent abundance relative to methanol. Additional boxcar averaging across 3 frequency points was used to smooth the spectra for very weak lines.

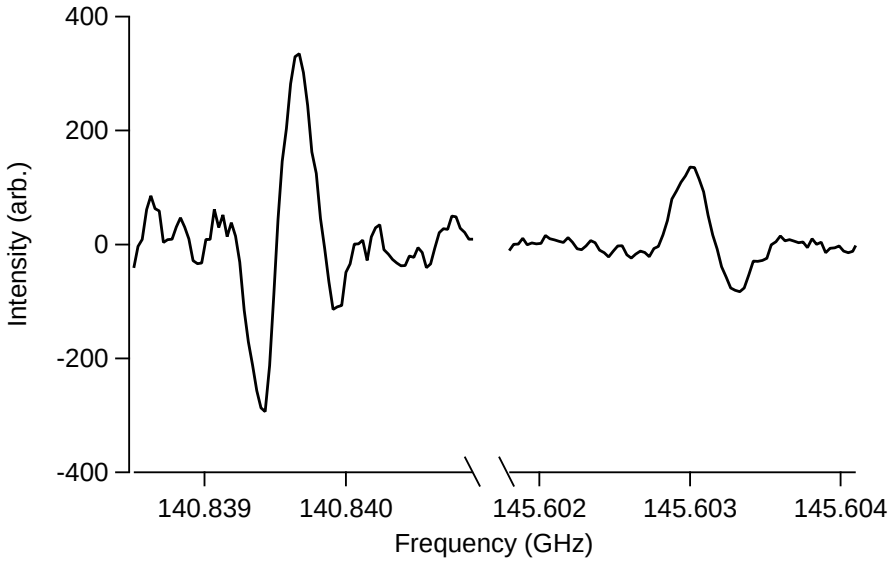

Figure 3.6 – Spectra of H_2CO detected using a plasma discharge source acting on a methanol/argon mixture.

Relative abundances compared to methanol were determined based on the Boltzmann analysis method described above. The Boltzmann diagrams for the products are shown in Figures 3.7–3.9. The CH_3O product was detected at $0.048 \pm 0.05\%$ relative to methanol, and a rotational temperature of 5.3 ± 2.7 K was determined. For H_2CO, only 2 lines were detectable using the double modulation detection scheme locked to the valve pulse. These lines have lower states that are very low in energy, and are therefore expected to be associated with the cold gas in the supersonic expansion. The additional 3 lines were only observed when the second lock-in amplifier was not used, i.e. the detection was not locked to the valve pulse. These lines involve much higher energy states, and are presumed to arise from the warmer background gas that is not associated with the expansion. We therefore use the two lines observed for the cold gas to estimate the temperature and abundance relative to methanol. Given that only two lines could be used for this analysis, the rotational temperature and abundance are not very well constrained. Nonetheless, the H_2CO product was detected at $0.036 \pm 0.014\%$ relative to methanol in the ground vibrational state, with a rotational temperature of 14 ± 5 K. Analysis of the warm gas component for H_2CO gives an abundance of 8.4 $\pm$ 1.5% relative to methanol in the ground vibrational state, with a

rotational temperature of 161 ± 80 K. Comparison of these two results for H_2CO indicates that the double-modulation detection scheme is a viable method for probing only the cold gas associated with the expansion, and eliminating confusion from any residual background gas in the chamber.

Using the results derived from the cold H_2CO lines, the branching ratio for CH_3O is >1.3 times that for H_2CO in the methanol dissociation mechanism under these conditions; a more quantitative analysis requires detection limits to be determined for the other possible methanol dissociation products (CH_2OH, OH, etc.).

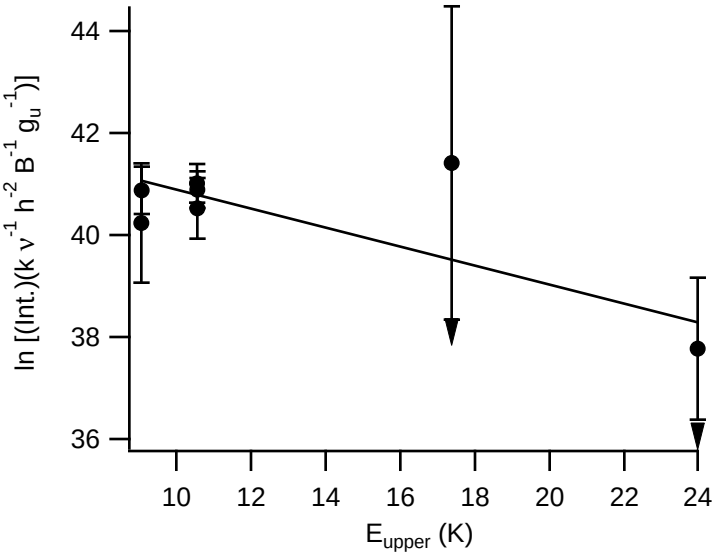

Figure 3.7 – Boltzmann diagram for CH_3O, where "Int." is the integrated intensity approximated as the product of the peak intensity and the linewidth at the zero-crossing points for the 2f lineshape.

3.2.5 Conclusions

This work describes the experimental design and first results from a multipass mm/submm spectrometer designed to probe dissociative reaction dynamics. This initial study focused on detection of the CH_3O and H_2CO products from the dissociation of methanol as a proof-of-concept for the experimental design, sensitivity limits, and quantitative nature of the results. Pure rotational spectral lines for methanol dissociation products were monitored

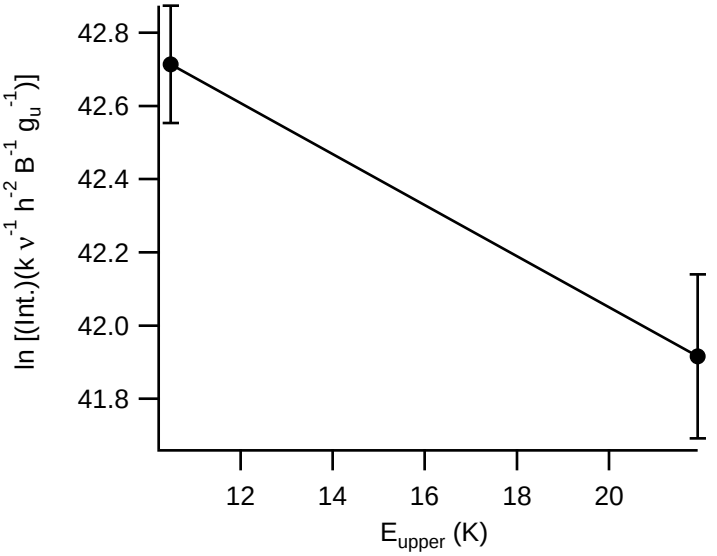

Figure 3.8 – Boltzmann diagram for cold H_2CO, where "Int." is the integrated intensity approximated as the product of the peak intensity and the linewidth at the zero-crossing points for the 2f lineshape.

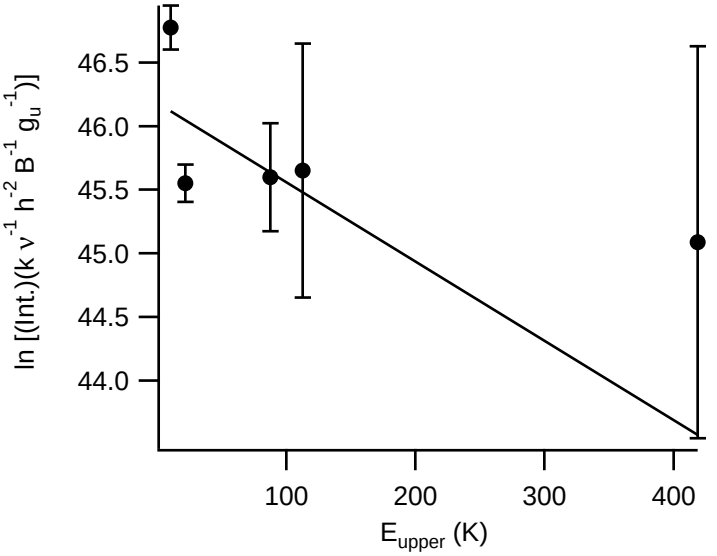

Figure 3.9 – Boltzmann diagram for warm H_2CO, where "Int." is the integrated intensity approximated as the product of the peak intensity and the linewidth at the zero-crossing points for the 2f lineshape.

via multipass direct absorption spectroscopy. Multiple lines from CH_3O and H_2CO were observed when a plasma discharge was used to dissociate methanol seeded in an argon supersonic expansion. A Boltzmann analysis was performed on the observed spectral lines, and the rotational temperature and abundance relative to methanol were determined for each product. A full quantitative determination of the branching ratios for the methanol dissociation mechanism under these conditions requires detection of the other dissociation products, which is not possible until rotational spectroscopic information on other possible dissociation products such as the CH_2OH radical is obtained.

Despite the limited information that this study reveals about the methanol dissociation mechanism, these results do demonstrate the promise that this approach has for examining the dissociation mechanisms for small organic molecules. This study has shown that the unstable products of dissociation reactions can indeed be quantitatively monitored using millimeter/submillimeter spectroscopic techniques. This method is therefore applicable to the study of any dissociation reaction where the products have permanent dipole moments. This technique also offers a structure-specific detection alternative in cases where mass spectrometry is not a viable option. Therefore, this approach offers a valuable new analytical method for identifying the participants in complicated reaction schemes, and can be applied to a variety of molecular systems.

This technique is applicable to a large range of chemical studies, as dissociation reactions involving small organics are of interest in several disciplines, including (but not limited to) astrochemistry, atmospheric chemistry, and combustion chemistry. Such studies are particularly valuable for molecules of astrophysical interest since dissociative reaction dynamics play a fundamental role in interstellar chemistry. Prime targets for astrochemical studies include the photodissociation reactions of small organics, which drive the chemistry on interstellar grain surfaces. Other important astrochemical mechanisms that could be studied using this approach include the production or dissociative recombination reactions involving molecular ions. Beyond dissociation reactions, this technique is more generally

applicable to the study of any unstable species that has a permanent dipole moment.

This technique opens the THz window for reaction dynamics studies, as the extension of this instrument to higher frequencies is straightforward, enabling spectroscopic studies across the entire 50 GHz to 1 THz frequency range. While this technique does have wide-ranging applications, any such study is dependent on the availability of the associated spectral information. In the case of dissociation studies, initial spectral studies that focus on dissociation product identification and compilation of rotational spectral line catalogs are required before quantitative results can be obtained.

It should also be noted that detection thresholds of dissociation products will be heavily dependent on spectral line strengths on a case-by-case basis. In general, dissociation products will likely have higher line strengths owing to their smaller partition functions, but it is also crucial that they be efficiently cooled in the expansion. Also, because any direct absorption technique allows for quantification of product, this experiment could greatly benefit from incorporation of cavity-enhanced spectroscopic techniques (see e.g. Alligood DePrince et al., 2013, and references therein) so as to increase spectral sensitivity even further beyond what can be achieved with the current spectrometer.

3.3 Application to Molecular Systems

3.3.1 Methanol Photodissociation Studies

The large effect that the methanol photodissociation BRs are predicted to have on the peak abundance of methyl formate highlights the importance of measuring the BRs in the laboratory. A gas-phase study promises the highest quantitative accuracy from a spectroscopic perspective, as well as providing the best agreement with quantum chemical *ab initio* calculations.

The UV absorption cross sections of methanol and its many isotopologues are well-established (Cheng et al., 2002). At wavelengths of approximately 164–200 nm, methanol

has a weak absorption feature which peaks at $\sim 6 \times 10^{-19}$ cm^2 near 184 nm. At shorter wavelengths, it has various vibronic absorption bands that peak at up to 15–20 $\times 10^{-19}$ cm^2, as well as a rising continuum at wavelengths below 138 nm.

Much effort has been directed at detection of UV-induced methanol photodissociation products (i.e. wavelengths of 120–200 nm). For this, a UV source is directed at the throat of the supersonic expansion so that photodissociation products may then be directed within the supersonic expansion, akin to the plasma discharge experiments presented above.

Two different types of UV sources could be used for this experiment: a continuous discharge lamp, or a pulsed excimer laser. Each have their advantages and disadvantages for studying photodissociation dynamics—namely, wavelength selection vs photon flux. Many experiments have been attempted, but to date no methanol photodissociation products have been observed. Below, I present the methods that have been initially employed for these experiments, and discuss considerations that must be addressed for future experiments.

Electrodeless Discharge Lamps

A variety of discharge lamps are available across much of the vacuum ultraviolet range of the spectrum, including both broadband, continuum and narrow band, line sources. This enables comprehensive wavelength-dependent studies, which are crucial for both astrophysical applications and benchmarks against theory.

A variety of electrodeless (i.e. microwave-driven) discharge lamps are available from Opthos Instruments, Inc. The low-pressure Hg line source overlaps well with the methanol absorption feature centered around $\sim$184 nm, with 10–20% of its output power centered at 184.9 nm; the Kr and Xe continuum sources overlap with the vibronic features between 130–170 nm; and, the Lyman-α line source and Ar continuum source both overlap with methanol's quasicontinuum absorption features at even shorter wavelengths. The Lyman-α source is particularly useful for application to astrophysical models. These lamps have photon fluxes rated at 10^{15} s^{-1}, and indeed this flux has been confirmed for two of the

longer wavelength lamps (Hg and Kr) using a calibrated power meter (Ophir Optics, 3A-P). Unfortunately, the photodissociation yield[a] of these lamps at the throat of the expansion is estimated to be approximately 10^{-6}–10^{-8}, which is challengingly low, and is limited simply by the short transit time of the sample across the UV beam.

Discharge lamps themselves generally contain no directional or focusing optics and are thus highly uncollimated. To compensate for this, a complex configuration of optics have been used to maximize the photon flux density at the interaction region of the throat of the supersonic expansion. Under this scheme, the light exiting from the $\varnothing 0.5$–1" lamp aperture was focused as much as possible directly at the aperture of the supersonic expansion.

The low photodissociation yield is due to both the relatively low instantaneous photon flux, and the short transit time of the molecular sample through the irradiation beam. A home-built optical chopper was used to periodically modulate the irradiating lamp; while since disbanded, all the parts can still be found in the laboratory and details on the design/construction of this apparatus can be found in Appendix B.1. Alternative steps need to be taken to improve the UV source brightness or increase the spectral detection sensitivity if one hopes to successfully implement this experimental scheme for future photodissociation studies, especially if applied to other organics besides methanol, which generally have even lower UV absorption cross sections.

GAM Excimer Laser

Photodissociation trials have also been undertaken using a pulsed excimer laser (Gam Laser, EX5) as the UV source. A pulsed laser has the advantage of providing much higher instantaneous photodissociation yields, at $\sim 2 \times 10^{-2}$ during the 1.5 mJ pulse of 157 nm light. However, a pulsed laser suffers two major disadvantages: low duty-cycles and limited wavelength selection.

Event timing is crucial during laser trials due to the pulsing nature of both the sample

[a]Photodissociation yield is calculated as $(1 - \exp[\text{-}\sigma_\lambda I_\lambda \Delta t])$, where σ_λ is the absorption cross section, I_λ is the photon flux density, and Δt is the total time of irradiation.

source and the laser. To accommodate this timing consideration, a digital delay generator (Stanford Research Systems, DG645) was used to control triggering, and a digital oscilloscope was used in place of the second LIA for on-the-fly control of time resolution. Under this scheme, a transient absorption signal was originally expected to occur $\lesssim$60 μs after the laser is fired[b]. The single LIA also introduces a significant delay (up to 150–200 μs) in the signal line, requiring careful consideration of the time frame for the search for spectral lines.

Other detection schemes that bypass a lock-in amplifier altogether have also been explored. One technique involves a gated integrator/boxcar averager (Stanford Research Systems), so that low duty cycle absorption signals may be detected more efficiently. Another technique simply involves monitoring the time evolution of direct absorption signals from the detector. Two analog pre-amplifiers (pre-amps) were constructed to enhance the dynamic range of the output signal of the ZBDs, so that they could be used with the instruments. More information on the design/construction of the pre-amps can be found in Appendix B.2.

This laser model is also capable of operation at 193 nm and $\sim$12 mJ/pulse—yet even at 10$\times$ more power, its photodissociation yield is $\sim$10$\times$ lower due to a significantly lower absorption cross-section at longer wavelengths. Still, this longer wavelength is much easier for experimental implementation, owing to reduced absorption by air and better optical properties among materials (i.e. higher reflectance and transmission), as compared to 157 nm. Many studies have been reported in the literature with this wavelength being used to produce methoxy from methanol (see, for example Oguchi et al., 2000). No experiments have yet been conducted at this wavelength. However, future studies with a laser at this wavelength could prove fruitful.

[b] assuming a transit distance of 2 cm at supersonic speeds

Concluding Remarks

No methanol photodissociation products have been detected using the VUV sources discussed above. Of the three channels that are predicted to dominate methanol photodissociation (CH_2OH, CH_3O, or H_2CO), CH_3O and H_2CO were not observed, and CH_2OH could not be searched for due to lack of spectral information. The non-detections could be due to:

a. insufficient detection sensitivity;

b. inadequate photodissociation efficiency; or,

c. an alternative channel, such as CH_2OH, that dominates UV-induced methanol photodissociation.

There is high confidence that a photodissociation product is detectable when one considers the successful benchmarks presented above (§3.2). This is especially true when one considers the additional electronic noise that the HV discharge induces in the detection electronics, from which a photodissociation experiment would not suffer. It is thus expected that detection sensitivity may simply be the limiting factor in the photodissociation studies outlined here. That being said, it cannot be completely ruled out that the photoproducts are not in their ground states by the time they are spectroscopically probed. It could also be that CH_3O immediately undergoes significant unimolecular decay (see, for example Melnik et al., 2011, and references therein).

Vacuum ultraviolet radiation is incapable of penetrating air under STP conditions. This may have affected the use of the excimer laser at 157 nm via imperfect purging of the beam path for the short distance ($\sim$6 cm) between the laser aperture and vacuum chamber window. VUV also has relatively poor optical properties with most materials. It is thus possible that too much UV radiation was lost prior to sample irradiation. The detection threshold for photoproducts was near the edge of what was theorized to be produced, and minor setbacks in the realized setup could easily have rendered the experiment unfeasible

with current equipment. To ensure that point (b) listed above is not an issue, a higher power UV source is highly recommended for revisiting methanol photodissociation. Also, incorporation of a multipass UV cell, such as what is reported by Duffy (2005), could also serve to increase photodissociation efficiency.

3.3.2 Methyl Hypochlorite Trials

Methyl hypochlorite (CH_3OCl) has also been tested as an alternative parent molecule for photodissociation studies. O−Cl chemical bonds are generally quite photosensitive, and reports in the literature support the use of methyl hypochlorite as a source of CH_3O (Krisch et al., 2004). Methyl hypochlorite was preferred over methyl nitrite (CH_3ONO) because its preparation is simpler and the hypochlorite is less explosive than the nitrite, which is in contrast to the nitrite being more widely reported in the literature as a parent molecule. Its UV absorption cross section has been characterized at wavelengths 200–460 nm (Jungkamp et al., 1995), however its VUV absorption cross section has not been reported.

Prior to each experiment, methyl hypochlorite was prepared using the techniques outlined by Krisch et al. (2004). While it can be stored within a foil-covered bottle at low temperatures (below $-40^{\circ}\mathrm{C}$), its degradation was found to limit the practicality of this. For the photodissociation trials, a seeded supersonic expansion was prepared in much the same way as the methanol photodissociation experiments, with the exception that the glass bubbler contains the dilute solution of dichloromethane and methyl hypochlorite prepared from the synthesis. The bubbler was also kept in an ice bath throughout its use, to prevent the sample from boiling away.

The rotational spectrum of methyl hypochlorite was predicted up to mm/submm wavelengths (for $J < 10$, without hyperfine splitting) based on a extrapolation from previous microwave studies (Ridgen and Butcher, 1964), so that its signal strength could be monitored on-the-fly to ensure sample was present. Methyl hypochlorite has an absorption cross-section of $\sim 12 \times 10^{-20}$ cm^2 for 248 nm light. The EX5 excimer laser could thus pro-

duce $\sim$5% depletion with a 20 mJ pulse. To date, however, no methoxy has been detected as a photodissociation product from either UV discharge lamps or 248 nm excimer laser.

3.3.3 A Spectral Search for Hydroxymethyl

Owing to the non-detection of CH_3O in the photodissociation studies described above, attention shifted to a search for CH_2OH. This, however, requires initiating a study of its pure rotational spectrum, as there is no data available in the literature. To this end, a search for the $J = 1 \leftarrow 0$ a-type transition was performed near 55,692 MHz. This was made possible by rotationally-resolved IR spectral studies which provided tight constraints ($1\sigma = 15$ MHz) on the CH_2OH rotational constants (Roberts et al., 2013).

CH_2OH preparation was attempted by combining a methanol-seeded Ar mixture (the same as is discussed above) with a He/5% Cl_2 balance and performing the HV plasma discharge on this mixture. The mixing of the methanol and chlorine gas mixtures was initially performed directly behind the valve, however this resulted in issues with the valve getting clogged due to undesired side-reaction products. To overcome this issue, two individual valves were used to keep the two mixtures separated. Each valve was mounted to an acrylic block so that the valves could be operated simultaneously, and channels within the acrylic block allowed for on-the-fly fast-mixing just prior to the discharge source and free-jet expansion.

No rotational lines were observed in the expected spectral region ($\pm 3\sigma$). This lack of detection may be due to either an unknown difficulty with the experimental chemical conditions, or a greater uncertainty in the expected transition frequency than was considered. This experiment should be continued once alterntive methods are used to confirm and/or optimize CH_2OH production. Meanwhile, experimental focus shifted back to studies of CH_3O.

3.3.4 Methoxy: Extending its Spectral Assignments

The pure rotational spectrum of methoxy has been the subject of only limited spectral studies. Endo et al. (1984) first reported the high-resolution pure rotational spectrum, which was obtained with a long-pathlength microwave spectrometer. This study established a derived Hamiltonian that included a number of terms to account for the effects that Jahn-Teller distortion induces in the microwave spectrum of the CH_3O $\tilde{X}^2E$ ground vibronic state. A JPL rotational line catalog (Pickett et al., 1998) has been created using the CALPGM software suite, and is based on the spectral lines reported by Endo et al. (1984) near 140 GHz ($J = {}^5/_2 \leftarrow {}^3/_2$) and 195 GHz ($J = {}^7/_2 \leftarrow {}^5/_2$). A number of studies have since improved the precision of the CH_3O molecular constants, as well as those of a number of CH_3O isotopologues (Momose et al., 1988; Liu et al., 2009b,a; Melnik et al., 2011).

These previous studies lent themselves quite readily to extending laboratory observations of CH_3O rotational lines. A dedicated effort has been undertaken toward this end, particularly for improving the spectral line catalog, which is most useful to the astronomical community. A number of strong transitions are predicted to occur near 247 GHz ($J = {}^9/_2 \leftarrow {}^7/_2$) and 303 GHz ($J = {}^{11}/_2 \leftarrow {}^9/_2$). Of particular interest has been spectral assignments/confirmations which overlap in frequency with the observational data that has been acquired by the Widicus Weaver research group at $\lambda = 1.2$ mm.

Experiments were carried out in a similar manner to those used for benchmarking the spectrometer, via a high-voltage plasma discharge coupled to the supersonic expansion of methanol. To minimize electrical noise that is picked up by the detection system, the operating conditions for the discharge voltage and current were reduced to 450 V and $\sim$15 mA, respectively. Also, the gap between the electrodes within the discharge source was increased from 1 mm to 5 mm so as to improve the yield of CH_3O and thus SNR of its lines. A summary of the observed rotational lines can be found in Table 3.1 and their spectra can be found in Figure 3.10(a–h). Curve fitting was conducted in the IGOR Pro software environment (WaveMetrics, Inc.) to determine line centers and uncertainties.

Table 3.1. Newly-observed transition frequencies of CH_3O (in MHz).

Upper State				Lower State				Obs	$O-C$[a]
N_K	Λ	t[b]	F	N_K	Λ	t	F		
$5_{\pm1}$	-1	11	4	$5_{\mp1}$	-1	11	3	247193.5[c]	N/A
$5_{\pm1}$	-1	7	5	$5_{\mp1}$	-1	7	4	247198.2[c]	N/A
$4_{-1,0,0}$	1	0,2,6	6,5,4	$3_{1,0,0}$	$1,-1,-1$	0,2,6	5,4,3	247414.8[c]	N/A
4_{-1}	1	3	5	3_1	1	3	4	247420.33	0.18
4_{-1}	1	9	4	3_1	1	9	3	247423.72	0.18
4_{-1}	1	13	3	3_1	1	13	2	247424.96	0.30
4_1	1	0	6	3_{-1}	1	0	5	247668.15	0.31
4_1	1	3	5	3_{-1}	1	3	4	247673.76	0.18
4_1	1	9	4	3_{-1}	1	9	3	247677.32	0.28
4_1	1	13	3	3_{-1}	1	13	2	247678.64	0.41

Notes.

[a] The calculated frequencies are those listed in the latest version of the JPL catalog (Version 1, 1/2/2006).

[b] The spin designation, t, follows the convention of the reference table described by the documentation for the JPL line catalog.

[c] Unresolved hyperfine splitting.

A summary of the molecular constants derived from a fit using the CALPGM software suite is shown in Table 3.2, which remains a very preliminary analysis. Information was incorporated from the report by Liu et al. (2009b)—particularly reconciling the results from Liu et al. with those using CALPGM—as well as our measurements of the lines observed at higher frequencies. Simulated stick spectra of the rotational lines for methoxy are shown in Figure 3.11, at rotational temperatures of both 300 K and 10 K. From the simulated stick spectrum, it is clearly shown that the lines targeted by this study are near the Boltzmann peak of the methoxy rotational spectrum at low temperatures, which are likely the most important features for an interstellar search, and which preclude a more complete spectral analysis of the warmer, more complex spectrum.

Table 3.2. Summary of Molecular Constants Determined for CH_3O (in MHz).

Constant	(Endo et al., 1984)		JPL Catalog[a]		(Momose et al., 1988)		(Liu et al., 2009b)		This Study	
A	154 960	(570)	151 472	(1 024)	160 050	(315)	154 670	(15)	154 615	(886)
B	27 931.14	(46)	27 930.124	(7)	27 929.849	(59)	27 930.38	(3)	27 930.22	(2)
D_K	2.11	[b]	−159	(65)	2.11	[b]	2.11	[b]	2.11	[b]
D_{NK}	0.769 9	(3 8)	−0.767 0	(37)	0.769 63	(1 08)	0.769 1	(6)	0.770 3	(11)
D_N	0.075 53	(44)	−0.075 301	(188)	0.075 788	(96)	0.075 36	(13)	0.075 15	(9)
$A\zeta_t$	54 330	(270)	54 334.5	[b]	52 273	(124)	52 036	(29)	54 701	(355)
$\eta_e\zeta_t$	1.82	(92)	−0.159 1	(121)	−0.936	(118)	0.374	(65)	−0.159	(9)
$\eta_K\zeta_t$	131.9	(181)	131.9	[b]	153.1	(58)	3.4	(37)	−13	(84)
$a\zeta_e d$	−1 865 980	(5 030)	−1 865 980	[b]	−1 873 283	(1 023)	−1 843 572	(143)	−1 877 493	(2 281)
$a_D\zeta_{ed}$	134	(75)	134	[b]	363	(25)	193	(6)	369	(236)
ϵ_{aa}	−40 930	(1 700)	−37 855	(12)	−36 897	(508)	−37 500	(93)	−38 111	(94)
ϵ_{bc}	−1 428	(66)	−1 458.14	(20)	−1 579.4	(160)	−1 107	(3)	−1 636	(35)
ϵ_1	−171.67	(38)	−171.79	(4)	−171.590	(85)	172.62	(13)	−171.43	(87)
ϵ_{2a}	2 420	(1 080)	−0.9	(68)	−984	(418)	−679	(79)	−8.2	(55)
ϵ_{2b}	436	[c]	−0.16	[c]	−172	[c]	−123	[c]	−1.5	[c]
h_1	75.446	(178)	86.53	(243)	76.380	(82)	−75.452	(260)	75.78	(67)
h_2	1 398	(40)	1 319.29	(86)	1 280.7	(54)	−1 331	(3)	−1 315.3	(12)
h_{1N}	0	[b]	0	[b]	−0.001 848	(298)	0.001 2	(6)	−0.001 05	(23)
h_{2N}	−0.004 7	(4 1)	0.003 6	(153 0)	−0.012 39	(67)	0.009 7	(3 4)	−0.014 3	(13 5)
h_{1K}	0.235 6	(11 6)	−10.93	(243)	−0.644	(85)	0.234	(254)	0.03	(67)
h_{2K}	−0.522	(47)	−0.115	(141)	−0.519	(17)	0.109	(14)	0.573	(104)
h_4	0.001 88	(1 38)	0.001 03	(1 62)	−0.000 38	(29)	−0.001 1	(5)	0.001 01	(1 26)
H_{KN}	−0.000 062	(34)	−0.001 03	(40)	−0.000 200	(30)	0	[b]	0	[b]
H_{NK}	0	[b]	0	[b]	−0.000 083 8	(16 2)	0	[b]	0	[b]
D_N^s	0	[b]	0	[b]	−0.087 1	(7 6)	0.031 3	(10 1)	0.070 2	(13 9)
D_{Na}^s	0	[b]	0	[b]	0	[b]	0.184	(44)	0	[b]
D_{Ka}^s	0	[b]	0	[b]	0	[b]	2.51	(16)	0	[b]
D_{Nb}^s	0	[b]	0	[b]	0	[b]	0.033 2	[b]	0	[b]
D_{Kb}^s	0	[b]	0	[b]	0	[b]	0.454	[b]	0	[b]
a_L	2.346	(37)	2.331 3	(18 4)	2.332	(80)	0	[b]	2.344 5	(17 9)
σ_0	119.00	(38)	121.11	(19)	121.64	(56)	0	[b]	121.17	(18)
$\sigma_\pm$	153.60	(109)	153.61	(51)	98.050	(118)	0	[b]	153.86	(45)
$T_0^2(C_0)$	4.343	(194)	4.923	(143)	3.067	(293)	0	[b]	4.896	(139)
$T_0^2(C_\pm)$	55.55	(109)	55.56	(51)	0	[b]	0	[b]	55.81	(44)
$T_{\pm 2}^2(C_0)$	0.279	(25)	0.336 6	(14 3)	0.278	(58)	0	[b]	0.333 6	(13 7)
$T_{\mp 2}^2(C_\pm)$	1.466	(88)	1.788	(51)	1.457	(208)	0	[b]	1.783	(46)
$T_0^1(P_\pm)$	0	[b]	0	[b]	3.632	(167)	0	[b]	0	[b]
RMS	0.046		0.056	(low-J)	0.1		0.326		0.114	

Notes.

[a] Version 1, 1/2/2006.

[b] Fixed.

[c] Scaled by (B/A).

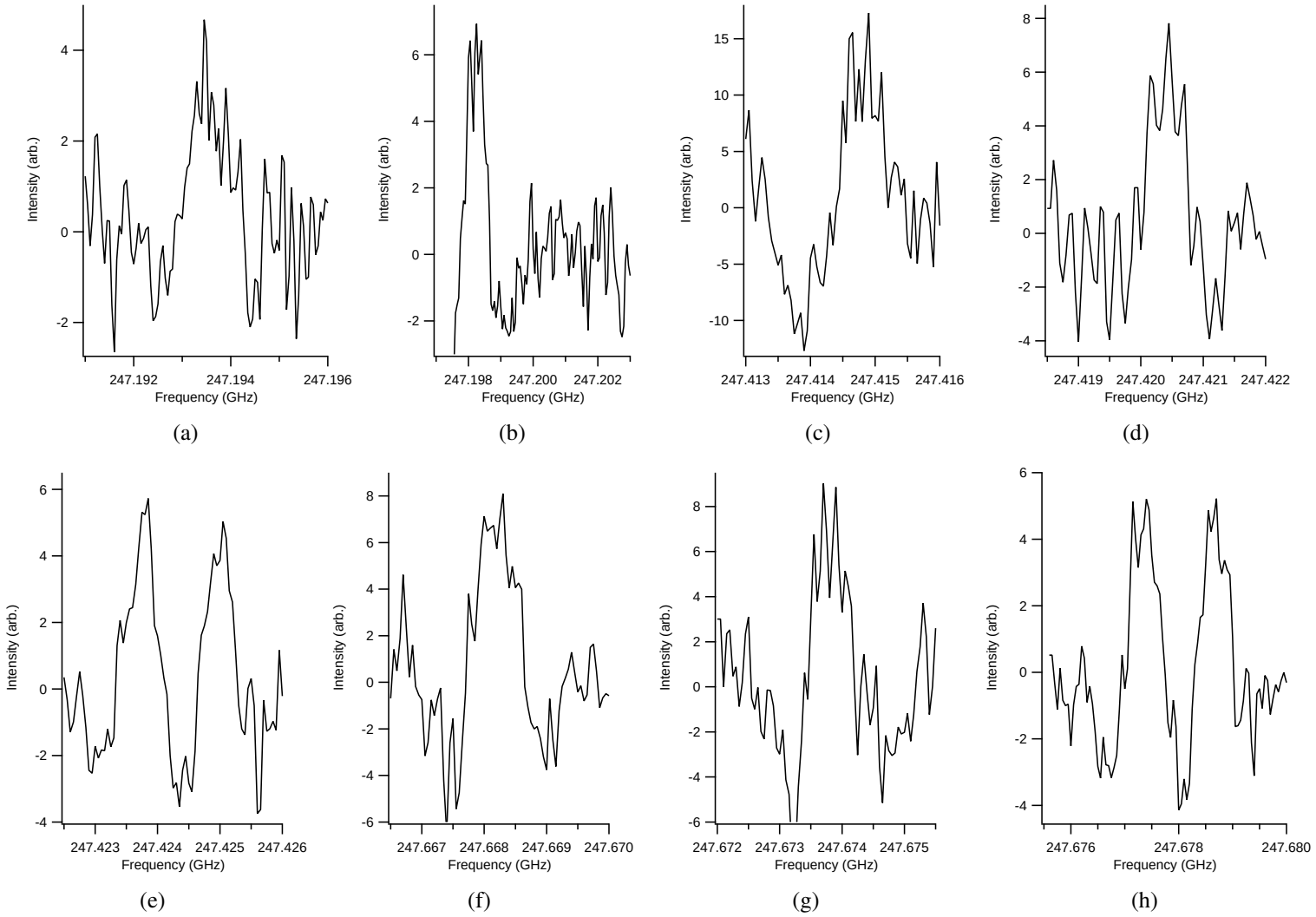

Figure 3.10 – Methoxy laboratory spectra observed near 247 GHz. Panels (a–c) likely contain multiple unresolved hyperfine features, and (c) may have a neighboring line just outside the scan range. These spectra all correspond to the transitions listed in Table 3.1

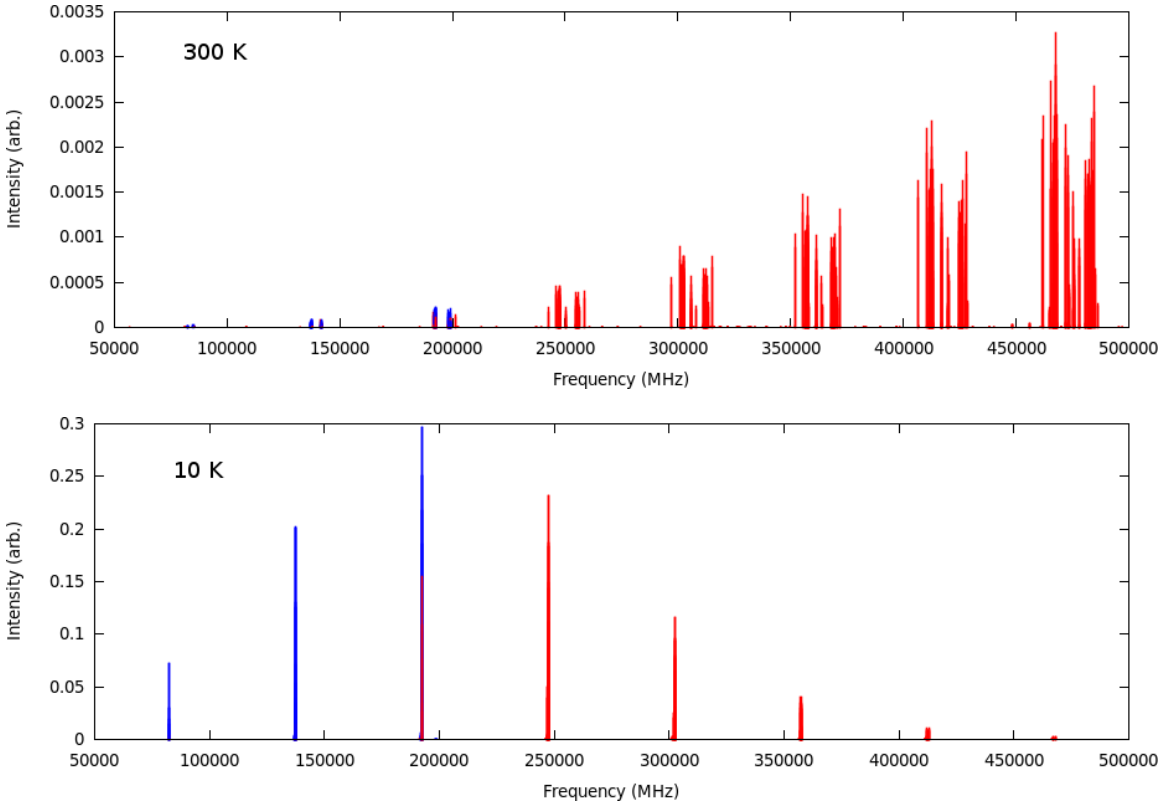

Figure 3.11 – Shown here are two simulated stick spectra for methoxy, at $T_{rot} = 300$ K (top) and $T_{rot} = 10$ K (bottom). The lines highlighted in blue are those that were used to produce the spectral fit for the JPL catalog (Ver. 1, 1/2/2006); the lines in red are unobserved. The lines near 250 GHz and 300 GHz that are strongest in intensity at $\sim$10 K have been the target of the experiments described above.

Chapter 4

Observational Astronomy with the CSO

I present here an overview of the observational astronomy projects in which I have participated during my time in the Widicus Weaver group. This work is a highly collaborative, long-term undertaking, which means the results presented here are only preliminary. Nonetheless, these observations lay the groundwork for comparisons to the astrochemical modeling studies as well as to the laboratory data that have and will be obtained using the methods outlined in the previous chapters. Much of the observational astronomy has been centered around data obtained with the Caltech Submillimeter Observatory (CSO) atop Mauna Kea in Hawaii.

4.1 Background

The CSO is a 10.4 m diameter radio telescope located 4,070 m above sea level. At this elevation, the precipitable water vapor generally remains $<$3 mm at night, providing excellent observing conditions for astronomy. The Widicus Weaver research group has conducted extensive observations with the CSO, amassing a library of 32 spectral surveys toward a variety of star-forming regions. Each spectrum contains up to hundreds or thousands of emission lines from tens to hundreds of molecular species. A figure containing all of the stacked spectra is shown in Figure 4.1. Each observed sightline was chosen based on pre-

viously observed molecular complexity combined with the stage of the source along the astrophysical evolutionary track from a cold, dense cloud in the interstellar medium to a warm, young stellar object.

Initial observations (pre-August 2012) were performed using the Caltech-built "Z-Rex" prototype receiver mounted at the Cassegrain focus of the CSO. When coupled with a University of Köln-built Acousto Optic Spectrometer (AOS5), effective resolutions of $\sim$1 MHz and spectral bandwidths of 4 GHz were achieved. More recently, a facility side-cab (Nasmyth focus) receiver was used in place of Z-Rex, and the Wideband Fast Fourier Transform Spectrometer (FFTS2) replaced the AOS5. These instrument upgrades enabled much quicker observational surveys, at even higher spectral resolutions, bringing the total number of line surveys to 32.

In general, system temperatures (SSB) were $\sim$100–200 K for all observations. The 10.4 m primary mirror provides a beam size of 28–33 arcseconds across the observed spectral range. While imaging studies remain limited for most of the sightlines' larger molecular species, it is likely that a beam size this large fully envelopes the sources.

4.2 Data Reduction

The raw data sets obtained with the CSO must first be reduced before they can be analyzed. This process is referred to as spectral deconvolution, as the raw data are a convolution of both the lower and upper sidebands of the telescope's superheterodyne (i.e. frequency-mixing) receiver. The raw data are contained in the CLASS file format (`http://www.iram.fr/IRAMFR/GILDAS`) and the data reduction is performed within the CLASS software. For more details on the data reduction, see Appendix C.

The double-sideband to single-sideband (DSB-to-SSB) deconvolution algorithm used is called the "Maximum Entropy Method", which was first implemented by Sutton et al. (1995) and has since become the most common algorithm used for this process. This is basically a process of converting multiply-redundant spectral sidebands in such a way

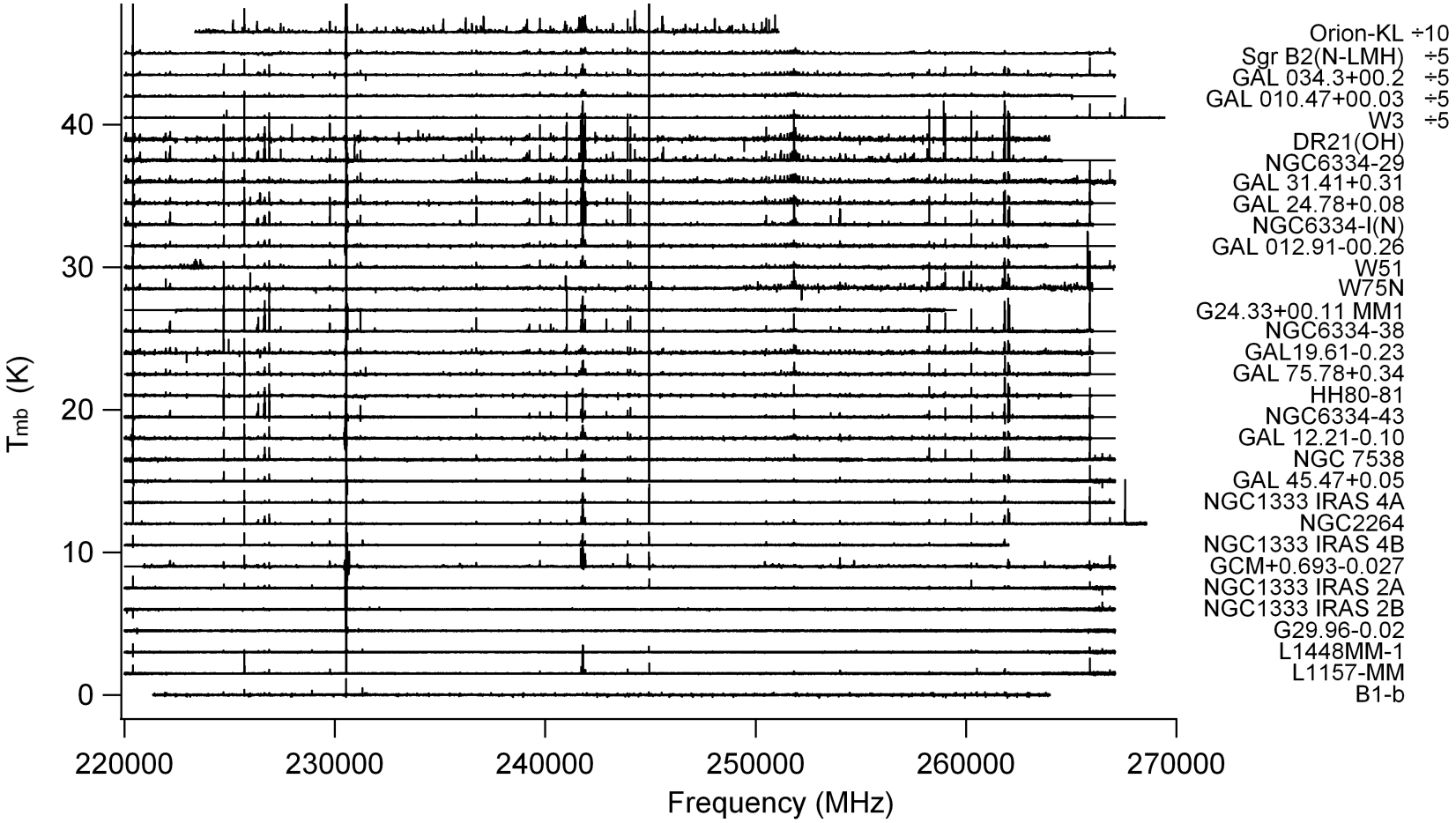

Figure 4.1 – Stacked (1.5 K offsets) single-sideband line surveys obtained with the Caltech Submillimeter Observatory (CSO).

that optical reconstruction can be performed to obtain a complete single-sideband (SSB) spectrum. Redundancy is crucial for the spectral deconvolution to work properly, and the observing scheme involves stepping across the entire spectral range in such a way that each frequency point has many overlapping sidebands (see Figure 4.2). The highest redundancy in our observations is $\sim$8, which is concentrated in a particular spectral region so as to provide a solid foundation for helping to anchor the deconvolution algorithm; a redundancy of $\sim$5 is more typical for the rest of the spectral region. The resulting spectrum for each source is a single, broadband, high-resolution spectrum spanning the frequency ranges of approximately 220–260 GHz, depending on the original spectral coverage. It was not uncommon to obtain slightly additional spectral coverage, when telescope time would otherwise be spent idling while another source was still rising, setting, or transiting.

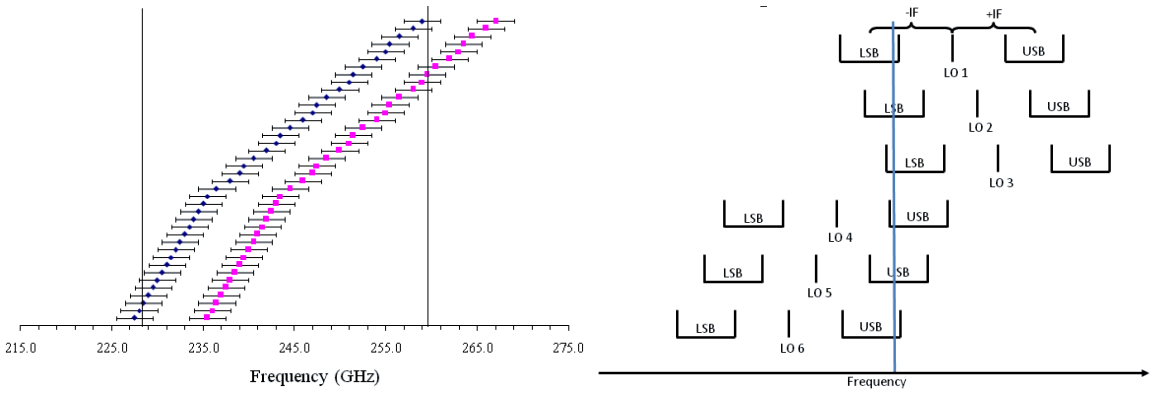

Figure 4.2 – Schematic diagram of the frequency sidebands spectral coverage used for the CSO observations. To the left, the lower- and upper-sidebands (in blue and pink, respectively) are shown for each individual scan, as the full spectral range is fully populated by these stepped scans. To the right, a particular rest frequency is shown consisting of a number of co-added spectra from sidebands of six individual scans.

4.3 Interstellar Methoxy

The CSO observations offer a large dataset with which laboratory spectra can be compared. There is much interest in the interstellar detection of methoxy and other organic species that are intermediates during the formation/destruction of more complex species. Such obser-

vations provide tight constraints that may be tested against current astrochemical models, as well as helping guide future ones.

Methoxy has recently been identified in the ISM, toward the dense, cold core B1-b via emission lines at wavelengths near 2 mm and 3 mm (Cernicharo et al., 2012). Relative intensities of the hyperfine components of the emission lines suggested a rotational temperature of 10 ± 3 K. At these temperatures, the rotational lines at higher frequencies, near 1.5 mm and 1.2 mm, are in fact much stronger in intensity. It is thus desirable to include the lines presented in §3.3.4 in future interstellar searches of methoxy.

In Figure 4.3, a simulated methoxy stick spectrum with a rotational temperature of 15 K—slightly warmer than the detections above—is shown overlapping a portion of the Widicus Weaver group's CSO line survey toward Orion-KL. The intensity scale of the simulated spectrum has been arbitrarily scaled. One can see that emission lines do indeed overlap in frequency where the strongest methoxy lines can be found, however they are all significantly blended with strong emission lines associated with common spectral "weeds". In the Orion-KL spectrum below, the strong features neighboring the simulated lines have each been labeled based on previous broadband line surveys of the Orion-KL and Sgr B2 regions at similar frequencies (Blake et al., 1986; Nummelin et al., 1998, respectively); the emission features that overlap with the simulated stick spectrum have been labeled based on a search of cataloged rotational lines using the "Splatalogue Database for Astronomical Spectroscopy" (`Splatalogue.net`, NRAO). This line confusion highlights the importance of first accounting for the complete overlapping mm/submm spectrum of a select few molecular species and their isotopologues prior to closer studies of the emission lines from less-abundant species. In all, about a dozen sources show emission lines in close proximity to the methoxy lines (see Appendix D, Figures D.1–D.6), including one source (G+0.693-0.027) that is a more unique physical environment than the rest, because of dust grain disruption due to shocks in the Galactic Center's central molecular zone (CMZ). Ultimately, a global spectral analysis of many other molecular species in each line survey must

be completed before spectral fits of CH_3O may be reliably concluded.

4.4 Spectral Fits

Work is currently still underway using spectral analysis software for global spectral fits of each line survey presented above for a subset of COMs. Many of these COMs (i.e. CH_3OH, CH_3OCH_3, CH_3CN, C_2H_5CN, $HCOOCH_3$) are notorious "interstellar weeds" and their analysis precludes a reliable study of most other interstellar species. Automated spectral fitting software has been designed and created in-house (Radhuber et al., A&A, *in revision*) to enable systematic analyses of each line survey. It rests upon the assumption of local thermodynamic equilibrium of all rotational states, and allows for the possibility of fits to multiple components with respect to velocity and rotational temperature.

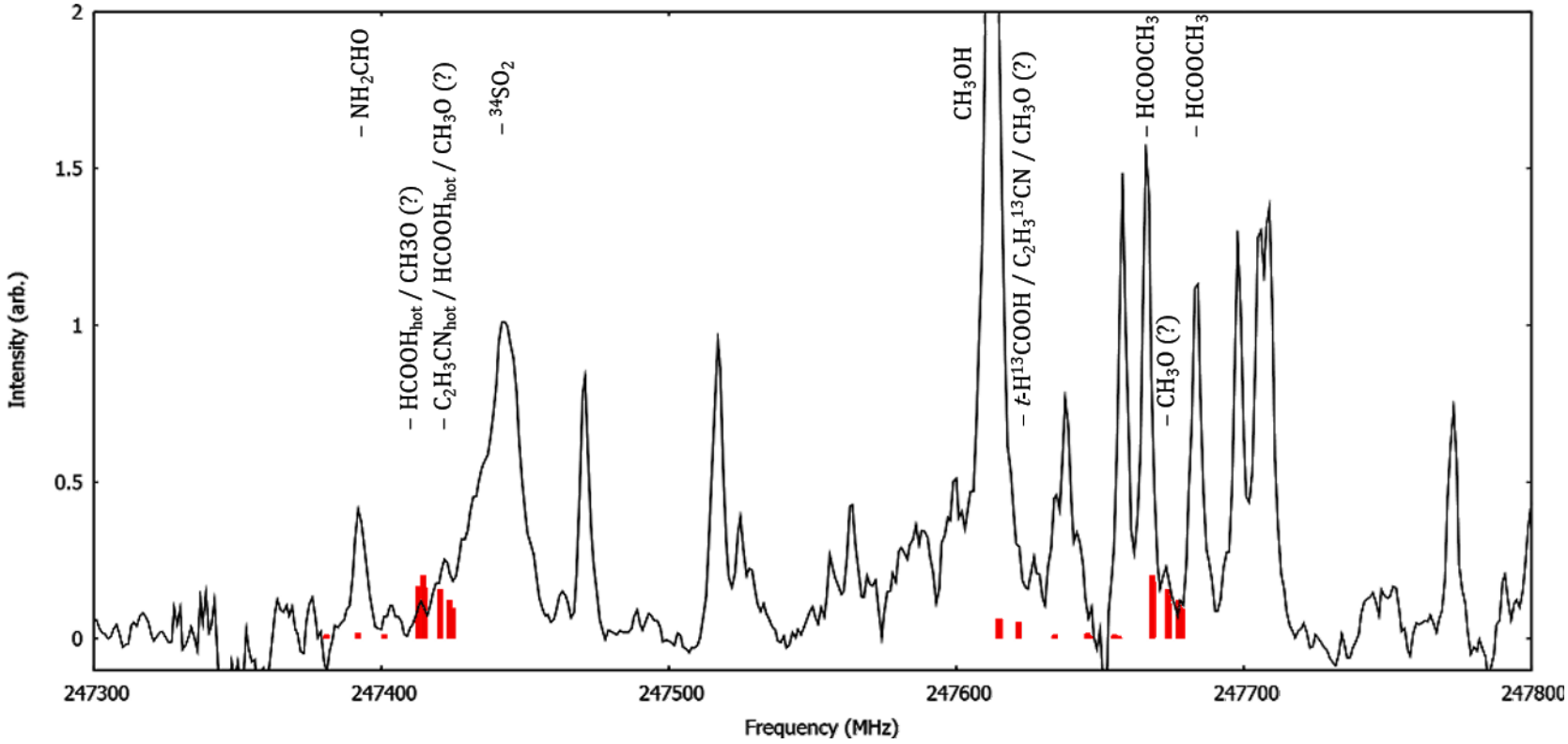

Figure 4.3 – Portions of the CSO line survey of the Orion KL region (black) and a stick spectrum of the methoxy radical (red). See text for details.

Chapter 5

Conclusions and Future Outlook

The work presented above is an example of the confluence of the three primary techniques used to study astrochemistry:

- astrochemical modeling;
- observational astronomy; and,
- experimental molecular spectroscopy.

The nature of the multidisciplinary aspects of astrochemistry demands either close collaboration of diverse research groups, or the auspices of a single, highly-versatile research group. In this case, the work of the latter is presented. I summarize here the major findings of the work presented above, and offer remarks about the future outlook on these subjects.

In §2.2.1, methanol photodissociation has been shown to play a significant role in the relative abundances of the stable $C_2H_4O_2$ structural isomers (i.e. methyl formate, acetic acid, and glycolaldehyde). One of these species is a well-known spectral weed (methyl formate), whereas another is an elusive interstellar species of high prebiotic interest (glycolaldehyde). While highly abundant in interstellar environments, there has been much uncertainty regarding the formation mechanism of interstellar methyl formate, and it is likely that grain surface chemistry plays a significant role. On the other hand, presented

in §2.2.2, two distinct gas-phase mechanisms have also been tested for their feasibility in forming methyl formate. It was found that one of them, the esterification reaction between protonated methanol and formic acid, not only may form a significant amount of methyl formate at warm interstellar temperatures ($T_{rot} \gtrsim 100$ K), but it may do so for the less thermodynamically-stable form (i.e. the *trans* diastereomer). This study thus opens the door for future studies of interstellar stereochemistry—the "holy grail" of which is of course the origins of homochirality. Extraterrestrial stereochemistry is likely to become an important topic in the field in the coming years, particularly with the advent of the current European Space Agency space-based mission *ROSETTA*, which has an enantioselective chromatograph onboard its COSAC experiment, and is planned to soon rendezvous with the comet 67P/Churyumov-Gerasimenko, to analyze its surface.

Given the importance of methanol photodissociation, attention was therefore focused on the experimental measurements of its branching ratios and dissociation products in the laboratory. To this end, a millimeter/submillimeter gas-phase spectrometer was designed, constructed, and benchmarked (§3.2). Efforts were made to measure methanol photodissociation products (§3.3.1), however this particular experiment will have to await a more powerful photodissociation source, which may become available soon. Experiments were also performed in support of new spectral measurements of its photodissociation products, hydroxymethyl (§3.3.3) and methoxy (§3.3.3), so that searches may be conducted in interstellar environments. Many new low-energy rotational lines of methoxy have been observed, and are being used to improve the spectral line catalog, which will aid both its interstellar search and the understanding of Jahn-Teller effects in small molecules.

During the same time as the modeling and laboratory work, observational astronomy was periodically conducted using the Caltech Submillimeter Observatory, ultimately amassing a library of 32 unbiased, broadband line surveys at $\lambda \approx 1.2$ mm. Work on the analysis of these observations using in-house spectral fitting software remains ongoing. Initially, the rotational spectra of nearly a dozen molecular species are being targeted, notably those

known as spectral weeds. Upon the completion of this initial analysis, targeted studies of molecular species of interest will then be possible. Specifically, an interstellar search for methoxy, and eventually hydroxymethyl[a] will be performed.

The methods and techniques presented above may all be generalized for the study of other chemical systems of interest. That is,

1. The OSU gas/grain astrochemical model is extensive and highly adaptable for the study of many other complex organic molecules;

2. The laboratory spectrometer is highly sensitive and could provide a testbed for many other dissociative reaction processes involving organic molecules; and,

3. The library of CSO line surveys is vast and likely contains emission features from dozens or even hundreds of yet-unidentified species, which only await either further spectral support in the laboratory, or specifically targeted spectral analyses.

[a]Upon the successful characterization of its experimental rotational spectrum.

Appendices

Appendix A

MM/SUBMM OPTICS

It is crucial to maintain a small beam profile throughout all experiments, so that excessive power loss does not disrupt maximum SNR and so that most of the spectral beam interacts only with the free-jet region (and thus coldest, most inert) of the supersonic expansion. All the optical solutions are presented here for the various multiplier frequency bands that were used in the work presented above. The labeling of the frequency bands of the multiplier chains are designated following the convention used by their manufacturer (Virginia Diodes, Inc.). I include the lens files and modeled beam from the SYNOPSYS™ (Optical Systems Design, Inc.) lens design software, as well as make note of whether the multipass optical cell was specifically implemented. SYNOPSYS™ was used only to serve as a guide to help with initial beam alignment, after which minor tweaks would be made to the system to peak up spectral power and, ultimately, the spectrometer's SNR. All focusing lenses were made of PTFE, most of which are commercially available (Thorlabs, Inc.).

A.1 VDI AMC Band 2 (55–60 GHz)

The lens file presented here is what was used for operation of the spectrometer at Band 2 (55–60 GHz), during the search of the $J = 1 \leftarrow 0$ a-type transition of hydroxymethyl. It was found that the beam profile could not be kept small enough for implementation of

the multipass optical cell; for much of the beam path, the beam radius exceeds ⌀3". Thus, the beam is introduced straight through the vacuum chamber, and is focused only at the interaction region of the supersonic expansion.

```
RLE
ID NEW LENS                                        1
FNAME '2 LENS 55.7GHZ - 100-4IN-plexi.RLE'
MERIT   0.100000E+13
LOG        1
WA1 5382.996
WT1 1.00000
APS               1
UNITS MM
OBG     4.8921
  0 AIR
  1 CV      0.0         TH         24.943
  1 AIR
  2 CV      0.0         TH         54
  2 AIR
  3 CAO     25.0        0.0        0.0
  3 CV      0.0         TH         12.8
  3 N1 1.44
  3 GID 'GLASS   '
  4 CAO     25.0        0.0        0.0
  4 CV     -0.025       TH         222 AIR
  4 AIR
  5 CAO     69.85       0.0        0.0
  5 CV      0.0041      TH         11.4
  5 N1 1.44
  5 GID 'GLASS   '
  6 CAO     69.85       0.0        0.0
  6 CV      0.0         TH         86 AIR
  6 AIR
  7 CV      0.0         TH         12.0
  7 N1 1.61
  7 GID 'GLASS   '
  8 CV      0.0         TH         252 AIR
  8 AIR
  9 CV      0.0         TH         252 AIR
  9 AIR
 10 CV      0.0         TH         0
 10 AIR
END
```

A.2 VDI AMC Band 4 (135–145 GHz)

The lens file presented below is what was typically used during operation of the spectrometer at Band 4, which includes all the trials for the benchmarks using the multipass optical cell. No physical changes to the optics were made when observing lines for formaldehyde, which lie outside the frequency range listed here.

```
RLE
ID NEW LENS                                        1
FNAME '2 LENS TELESCOPE 140GHZ - 100-300-plexi.RLE'
MERIT   0.100000E+13
LOG        1
WA1 2141.375
WT1 1.00000
APS              1
UNITS MM
OBG     2.386141
  0 AIR
  1 CV      0.0       TH     19.534186
  1 AIR
  2 CV      0.0       TH     52.1
  2 AIR
  3 CAO     25.0      0.00      0.0
  3 CV      0.0       TH     13.8
  3 N1 1.43
  3 GID 'GLASS   '
  4 CAO     25.0      0.0       0.0
  4 CV     -0.0250    TH    252.6 AIR
  4 AIR
  5 CAO     25.0      0.0       0.0
  5 CV      0.0083333333333   TH     7.6
  5 N1 1.43
  5 GID 'GLASS   '
  6 CAO     25.0      0.0       0.0
  6 CV      0.0       TH    32.8 AIR
  6 AIR
  7 CV      0.0       TH     12.0
  7 N1 1.60
  7 GID 'GLASS   '
  8 CV      0.0       TH     345 AIR
  8 AIR
```

```
  9 CV      0.0       TH     145.0 AIR
  9 AIR
 10 CV      0.0       TH     0.0
 10 AIR
END
```

The lens file presented below makes use of the optical arrangement used at lower frequencies, hence the ⌀4” lens at the second position.

```
RLE
ID NEW LENS                                        1
FNAME ’2 LENS TELESCOPE 140GHZ - 100-4IN-plexi.RLE’
MERIT   0.100000E+13
LOG        1
WA1 2141.375
WT1 1.00000
APS              1
UNITS MM
OBG     2.386141
  0 AIR
  1 CV      0.0       TH     19.534186
  1 AIR
  2 CV      0.0        TH        69
  2 AIR
  3 CAO     25.0       0.0       0.0
  3 CV      0.0        TH        12.8
  3 N1 1.44
  3 GID ’GLASS   ’
  4 CAO     25.0       0.0       0.0
  4 CV     -0.025      TH        250 AIR
  4 AIR
  5 CAO     69.85      0.0       0.0
  5 CV      0.0041     TH        11.4
  5 N1 1.44
  5 GID ’GLASS   ’
  6 CAO     69.85      0.0       0.0
  6 CV      0.0        TH        50 AIR
  6 AIR
  7 CV      0.0        TH        12.0
  7 N1 1.61
  7 GID ’GLASS   ’
  8 CV      0.0        TH        252 AIR
```

```
  8 AIR
  9 CV      0.0        TH        252 AIR
  9 AIR
 10 CV      0.0        TH        0
 10 AIR
END
```

A.3 VDI AMC Band 5 (145 GHz, 190 GHz, 220 GHz)

The lens file included here is what was used for peaking up methoxy lines with Band 5, prior to switching to Band 6 for new observations. It was found that a 3" custom-made lens quite efficiently focused the beam at both Band 5 and Band 6, thus enabling the ability to operate at a broad frequency range without significant changes to any physical parts.

```
RLE
ID NEW LENS                                        1
FNAME '2 LENS TELESCOPE 193GHZ - 3IN-4IN-plexi.RLE'
MERIT   0.100000E+13
LOG        1
WA1 1557.36
WT1 1.00000
APS              1
UNITS MM
OBG     1.62171944198
  0 AIR
  1 CV      0.0       TH         10.27541272158
  1 AIR
  2 CV      0.0       TH         33.2
  2 AIR
  3 CAO     38.1       0.0       0.0
  3 CV      0.02       TH        41.91
  3 N1 1.44
  3 GID 'GLASS   '
  4 CAO     38.1       0.0       0.0
  4 CV     -0.02       TH        100.0 AIR
  4 AIR   5 CAO     69.85     0      0
  5 CAO     69.85      0.0       0.0
  5 CV      0.0        TH        11.4
  5 N1 1.44
  5 GID 'GLASS   '
```

```
  6 CAO     69.85       0.0        0.0
  6 CV     -0.0041      TH         50 AIR
  6 AIR
  7 CV      0.0        TH         12.0
  7 N1 1.61
  7 GID 'GLASS   '
  8 CV      0.0        TH         345 AIR
  8 AIR
  9 CV      0.0        TH         145.0 AIR
  9 AIR
 10 CV      0.0        TH         0
 10 AIR
END
```

A.4 VDI AMC Band 6 (247 GHz, 303 GHz)

Here I include the lens file which was used to guide the operation of the spectrometer at Band 6 frequencies. The only significant difference between this lens solution and that of Band 5 near 193 GHz is the distance between the feedhorn and first lens. It should be noted, however, that the second lens was not used during spectroscopy experiments, as it was found to not significantly affect observed line intensities, and it was advantageous to minimize the number of surface elements along the beam path so as to minimize etalons in the power spectrum.

```
RLE
ID NEW LENS                                    1
FNAME '2 LENS TELESCOPE 245GHZ - 3IN-4IN-plexi.RLE'
MERIT   0.100000E+13
LOG        1
WA1 1223.64268571
WT1 1.00000
APS              1
UNITS MM
OBG     1.18119803677
  0 AIR
  1 CV      0.0        TH         5.0730509
  1 AIR
  2 CV      0.0        TH         45
```

```
  2 AIR
  3 CAO      38.1        0.0        0.0
  3 CV       0.02        TH         41.91
  3 N1 1.44
  3 GID 'GLASS   '
  4 CAO      38.1        0.0        0.0
  4 CV      -0.02        TH         100 AIR
  4 AIR   5 CAO      69.85     0       0
  5 CAO      69.85       0.0        0.0
  5 CV       0.0         TH         11.4
  5 N1 1.44
  5 GID 'GLASS   '
  6 CAO      69.85       0.0        0.0
  6 CV      -0.0041      TH         50 AIR
  6 AIR
  7 CV       0.0        TH         12.0
  7 N1 1.616
  7 GID 'GLASS   '
  8 CV       0.0        TH         345 AIR
  8 AIR
  9 CV       0.0        TH         145.0 AIR
  9 AIR
 10 CV       0.0        TH         0
 10 AIR
END
```

A.5 Multipass Optical Cell

Generally speaking, the multipass optical cell was implemented only for Bands 4 and 5, which was found to be the optimum trade-off between power loss and signal gain. Significant power loss could be due to either clipping the edge of various optical mounts, or when the spot size on the multipass mirrors was $\gg \omega$. The various optical parameters used for the design and implementation of the $\varnothing$3" multipass optical cell are presented in Table A.5.

The size of the spherical mirrors and mirror spacing was selected so that the optical cell could be fully contained within the vacuum chamber. Two $\varnothing$2" steering mirrors were also used directly behind the first mirror, so that the incoming beam could be precisely controlled.

Table A.1. Typical optical parameters of the ⌀3” multipass cell

Parameter	Symbol[a]	Value
Mirror diameter	D	3”
Mirror focal length	f	3”
Mirror radius of curvature	R	6”
Pattern height	h	2.5”
Number of passes	N	7
Actual mirror spacing	L	11.2”
Spot size	ω	0.73”

Notes.

[a] Following the convention used by Kaur et al. (1990).

.

Appendix B

Misc. Electronics

A number of electronic apparatuses were custom-built during the design, construction, and experimentation of the spectrometer discussed in Chap. 3. While somewhat elementary from an academic perspective, they were found to be incredibly helpful in the laboratory, and the savings in cost that they provided (labor-included) was immense with respect to commercially-available instruments. The details of their design and construction are included here.

B.1 *in vacuo* Optical Chopper

The design/construction of a home-built optical chopper for use with the UV electrodeless discharge lamps is presented here. This chopper was briefly implemented as a means of performing phase-sensitive detection of photodissociation products.

B.1.1 DC Motor and Chopper Wheel

A 1,080 rpm DC brush motor (Phidgets, 3261) was used (*in vacuo*) to drive an optical chopper wheel (Thorlabs, MC2F57). The DC motor was powered using a standard 12 V_{DC}, 2.0 A power supply and motor controller (Phidgets, 1065). The DC motor was able to continuously operate under vacuum conditions without modification (i.e. no additional

heat sink). The chopper wheel was attached to the shaft of the DC motor using a simple sleeve adapter machined specifically for this purpose.

B.1.2 External Communication

A fast-response, UV-sensitive GaP photodiode (Thorlabs, FGAP71) was used *in vacuo* to monitor the activity of the chopper and serve as input for an external analog-to-digital converter (A/D) circuit. This A/D circuit served as the phase reference source for a LIA. The photodiode itself was located directly beneath[a] the UV focal point and throat of the supersonic expansion. The photodiode was used in unbiased voltage mode (Fig. B.1, left) with a 2 MΩ load, and the peak voltage output during full illumination of the UV beam was ∼500 mV. A standard voltage comparator IC (Texas Instruments, LM393) was used to convert the signal from the chopped UV beam to a TTL (Fig. B.1, right).

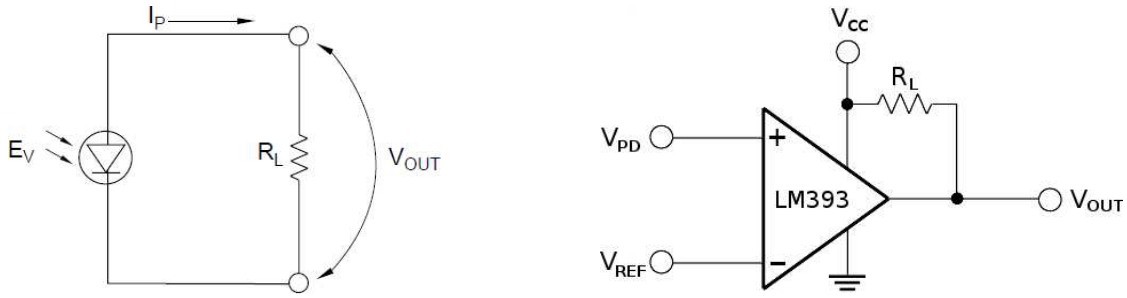

Figure B.1 – Electronic circuits used for the function of the optical chopper. The photodiode was used in unbiased voltage mode, with R_l set at 2 MΩ (left), while a voltage comparator integrated circuit (IC) was used for analog-to-digital conversion (right). See text for details.

Under typical conditions, the photodiode voltage was an sinusoidal-like signal ranging between 0 and ∼500 mV, and it was desired to achieve a TTL binary signal that oscillated between 0 and 5–10 V. The reference voltage V_{REF} was set to 380–390 mV, the supply voltage was ∼4.2 V, and the pull-up load resistor R_L was 49.9 kΩ. The A/D circuit was powered by two batteries: a) a AA battery powering a resistive voltage divider circuit

[a] A plano-convex lens was needed to refocus the diverging UV beam onto the collecting area of the photodiode.

($R_1 = 60\Omega$, $R_2 = 20\Omega$) provided the reference voltage, V_{REF}; and, b) a 9-Volt battery provided the IC supply voltage, nominally $V_{CC} \approx 5$–10 V. The resulting TTL pulse has a response time (to 95% full signal) of $\sim$90 μs, and thus gives $<$2% phase accuracy across the entire chopping cycle.

B.2 Pre-amps for ZBD Use

The zero-bias diode detectors (ZBDs) used by the Widicus Weaver research group typically have a responsivity of 1500–3000 V/W. Under standard spectrometer conditions, this results in a output voltage of approximately -10 mV to -30 mV. While a lock-in amplifier (LIA) has no problem with this voltage scale, it is much too small of a scale for a gated integrator/boxcar averager and/or oscilloscope. To overcome this issue, two different pre-amps were constructed to increase the dynamic range of the ZBD voltage output. For this application, circuits based on low-noise operational amplifiers (op-amps) were designed and constructed; one is a simple inverter with moderate gain and a low-pass filter, whereas the other employs higher gain and a user-controllable DC voltage offset.

Both amplifier circuits presented below are based on the same op-amp integrated circuit (IC). The choice of the specific op-amp chip was based on the ability to operate rail-to-rail from a single supply, and have low noise and high bandwidth. The component of choice was thus the CMOS-based IC OPA350 (Texas Instruments).

B.2.1 Gain-of-10 Inverter

The first pre-amp was designed with only moderate filtering and direct amplification in mind. For this, an inverting op-amp circuit was chosen. A first-order low-pass filter was also incorporated into the design, to provide a bandwidth rolloff of 6 dB/octave at frequencies below a desired value. The circuit diagram of this first pre-amp is shown in Fig. B.2, and the values for the electrical components are shown in Table B.1. For this circuit, the

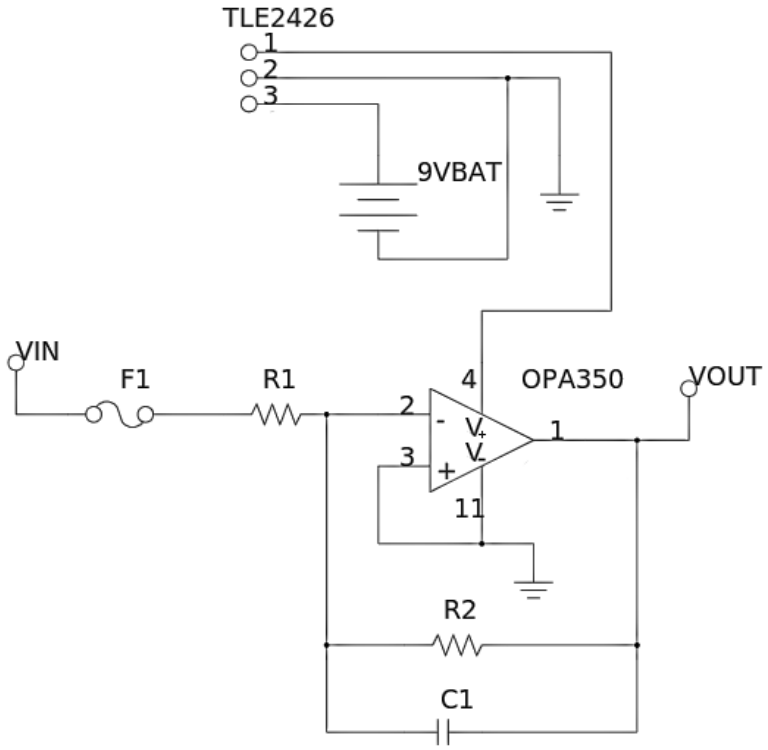

Figure B.2 – Electric circuit for the first op-amp-based pre-amplifier (a gain-of-10 inverter).

Table B.1. Components' electrical values for pre-amp #1.

Component	Value
F_1	$1/2$ A
R_1	1 kΩ
R_2	100 kΩ
C_1	5 pF

rolloff frequency is

$$f_0 = \frac{1}{2\pi C_1 R_2} \approx 320 \text{ kHz}, \tag{B.1}$$

thus enabling detection of a transient signal during a sample's crossing of the spectral beam (10s of μs), but filtering out higher frequency noise. The gain is calculated to be:[b]

[b]It must be noted that the actual gain for this particular circuit is ∼10 when used with the ZBDs. The reason for this is unknown, as it operates as designed when used with any other equipment. Thus, this pre-amp is labeled as gain-of-10 for all intents and purposes.

$$gain = \frac{R_2}{R_1} = 100. \tag{B.2}$$

A 9-volt battery supplies a "rail splitter" IC (Texas Instruments, TLE2426), whose output then supplies power to the op-amp[c]. Initially, a resistive divider was used in place of the rail splitter, but it was found to have a number of performance issues (ambient noise, low bandwidth, and high power consumption). To reduce the risk of damage to the ZBD, a fast-acting fuse ($1/2$ A) is used at the input of the pre-amp.

B.2.2 Gain-of-200 Inverter, with DC Offset

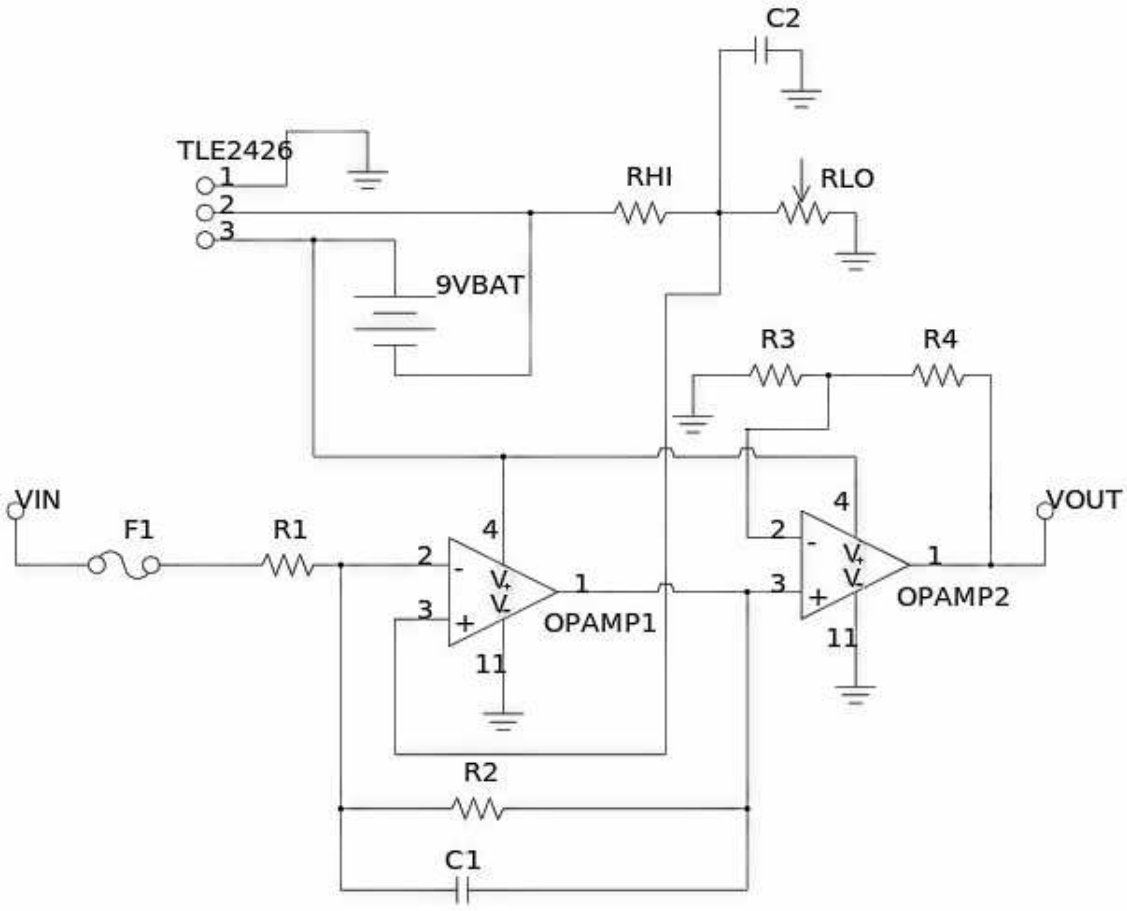

Figure B.3 – Electric circuit for the second pre-amp (a gain-of-200 inverter, with DC offset).

[c]The OPA350 has an allowed supply voltage V_S of 2.7–5.5 V.

Table B.2. Components' electrical values for pre-amp #2.

Component	Value
F_1	$1/2$ A
R_1	1 kΩ
R_2	10 kΩ
C_1	5 pF
R_3	50 Ω
R_4	1 kΩ
R_{HI}	1 MΩ
R_{LO}	5 kΩ (max)
C_2	100 pF

A second, more sophisticated pre-amp was constructed with much higher gain in mind. To accommodate this higher gain, a DC voltage offset was required so that the baseline voltage of the desired signal did not exceed either what the power source could supply, or the readout limitations of an oscilloscope. The oscilloscope issue was particularly problematic, as oscilloscopes typically do not provide the ability to zoom all the way in on large voltage offsets, yet we were interested specifically in tiny effects within a large signal.

Compared to the first, the circuit for this second pre-amp (Fig. B.3) essentially only contains one additional subcircuit, however a number of other modifications were also made with respect to the first. The first subcircuit of this pre-amp is a gain-of-10 inverter, which feeds into an additional op-amp subcircuit. This second op-amp subcircuit is simply a voltage follower, and provides only further amplification ($gain = {}^{R_4}/_{R_3} = 20$). In this way, neither op-amp is operating near their high-gain limit. Both op-amps are supplied by the half-voltage of a 9-volt battery.

The key modification of the first op-amp subcircuit is that which provides the DC voltage offset: a user-controllable variable resistor (R_{LO}) forms part of a resistive voltage divider, the output of which provides a reference voltage to the first op-amp subcircuit. This pre-amp's first op-amp subcircuit thus amplifies the difference voltage between that

of the ZBD and the reference voltage—the first pre-amp's op-amp circuit does the same thing, except that its reference voltage is simply Ground. The TLE2426 IC must be operated slightly differently from that of the first pre-amp: for this circuit, its output is held at ground (pin 1), causing its Common (pin 2) to float at -0.5×9 V, and its Input (pin 3) at $+0.5 \times 9$ V. This way a small negative voltage can be used as a reference voltage for the ZBD's small negative output voltage. The reference voltage from the resistive voltage divider is always

$$V_{REF} = (-\frac{1}{2}V_9) \times \frac{R_{LO}}{R_{HI} + R_{LO}}, \tag{B.3}$$

where $-1/2 V_9$ refers to the voltage coming from the negative rail of the TL2426. It was chosen to set R_{HI} to a large value (1 MΩ) so that the divider would not drain the battery very quickly when the variable resistor was set to zero (for $V_{REF} \approx 0$). It is crucial that this reference voltage be highly stable. To this end, a bypass capacitor (C_2) is used between V_{REF} and ground to filter out high-frequency ripple.

Appendix C

CSO DSB Spectral Deconvolutions

While spectral deconvolution has been performed many times over, there remains very little documentation on this process (the whole of which shall be referred to as "the pipeline"). The general steps within the pipeline are as follows:

1. Remove abnormal spectral features (i.e. spikes, spurs);
2. Remove the baseline (i.e. standing waves, dust continuum);
3. Perform the spectral deconvolution; and,
4. Check the final SSB spectrum against the original DSB.

These steps are each contained within a set of scripts, most of which[a] operate within the CLASS program of the GILDAS software environment.[b] The process is very much an iterative process, where a rough first pass is made to get to a "model" SSB spectrum, which helps to then identify problematic scans. The scripts and process are not unlike that which is presented by McGuire et al. (2013)[c], with the exception being how the baseline removal is performed. This process is crucial to the quality the final line survey data, yet it can easily produce bad results if proper care is not taken.

[a] The exceptions being a few Perl scripts to speed up certain tasks.
[b] `http://www.iram.fr/IRAMFR/GILDAS`
[c] `http://tracker.cv.nrao.edu/PRIMOS/CSO_260_290_Survery_Data/`

The baseline must be removed for each spectral scan, one by one, either by-eye or algorithmically. Generally speaking, the baseline of each individual spectral scan can be approximated quite well as a flat, constant offset from zero intensity. The by-eye method can take many hours for each source, due to the presence of hundreds individual spectral scans, and it is also rather inconsistent. It's been found that the standard deviation of baselines estimated by-eye for a set of scans overlapping in frequency is generally comparable to the ideal final noise level after deep integration. Thus, estimates by-eye produce significant, yet unnecessary, additional error. For spectrally-rich scans (i.e. those from about half the sources), the presence of strong spectral features pose a challenge for an automated algorithm, even for a high-order polynomial fit.

The general flow chart for the automated baseline removal process is shown in Figure C.1. A single parameter is used to control how aggressively outliers are removed during each pass through a scan. The intensity cutoff is simply the difference from the mean by a multiple of the standard deviation of the current pass through the spectral scan; multiplying factors in the range of 1.5–2 typically work the best. Once no more outliers exist, the scan is thought to contain only the baseline. When this occurs, either a constant offset is determined via the mean of all the remaining baseline values, a first- or higher-order polynomial is fit to the remaining values, or a running boxcar average is obtained. Under most circumstances, a constant offset is used and yields standard deviations many orders of magnitude lower than a by-eye estimate. In a handful of spectrally-rich line surveys, and in the case of the few line surveys which contain standing wave-like patterns along the baseline, a boxcar average must be performed. The boxcar width is an additional parameter that must be set (generally ± 50 channels). This latter process takes much longer than a simple offset/curve fit, but it yields great results. In general, non-zeroth order polynomials yield the worst results, as they tend to yield poor fits near the edges.

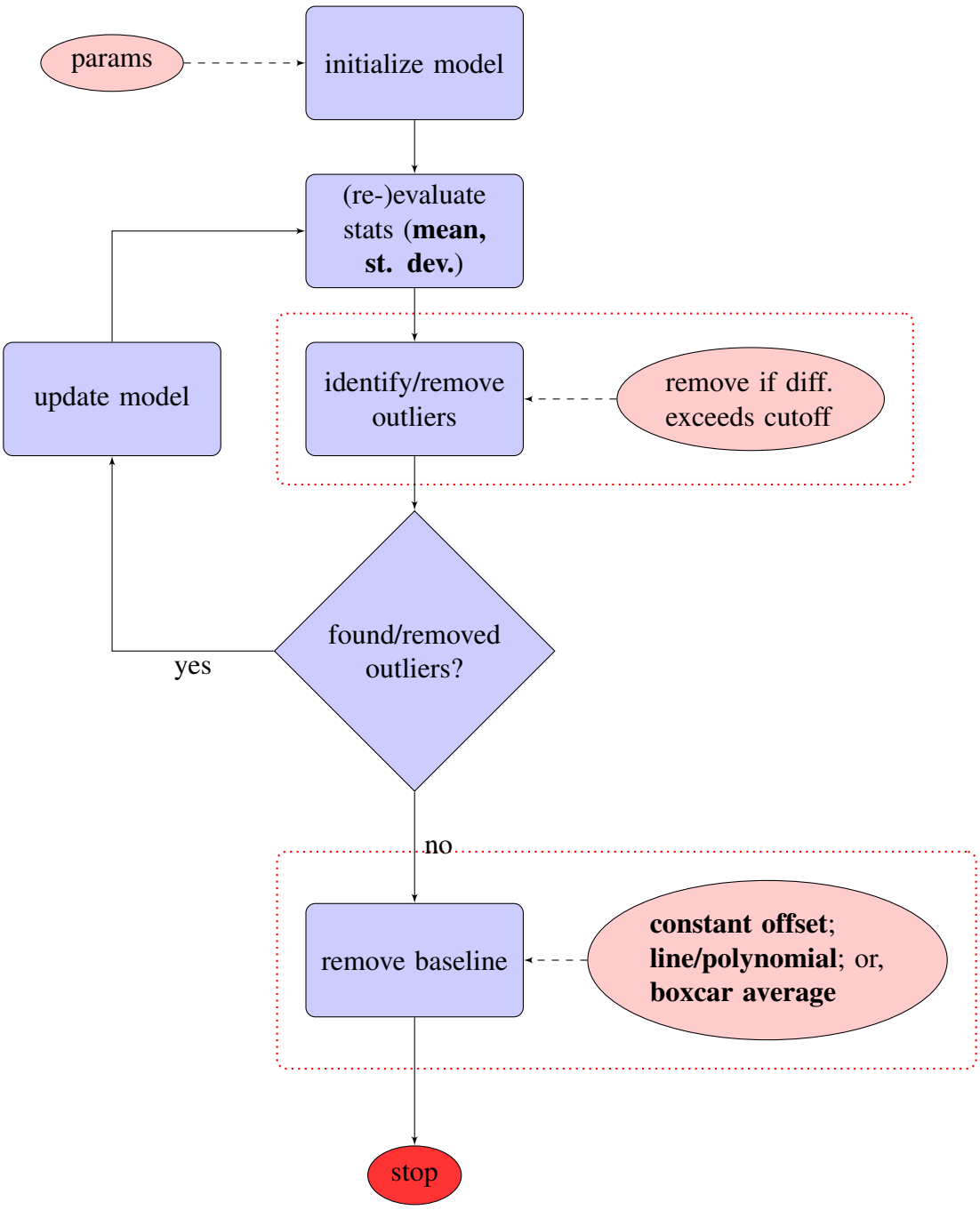

Figure C.1 – Flow chart for an automated baseline removal algorithm.

Appendix D

Methoxy vs CSO Line Surveys

Included here (Figures D.1–D.6) are examples of the CSO line surveys with emission lines in close proximity/overlapping with a predicted stick spectrum (at $T_{rot} = 10$ K) of methoxy. The scale of the stick spectrum has been scaled arbitrarily so as to closely match observations. A complete spectral analysis is pending, while the "spectral weeds" are first being fully analyzed.

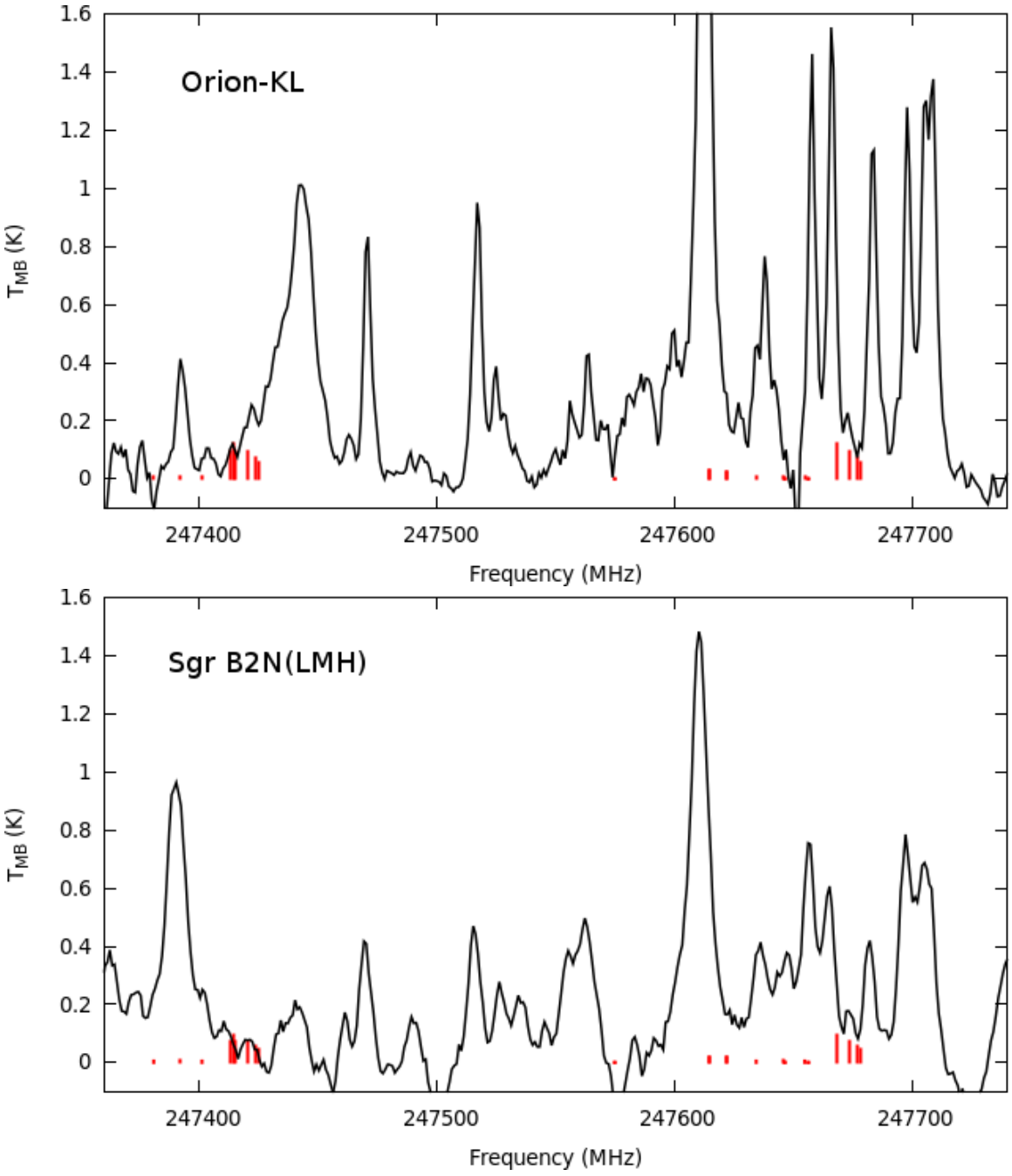

Figure D.1 – Simulated methoxy stick spectrum ($T_{rot} = 10$ K, arb. scaling) atop a portion of the CSO line surveys.

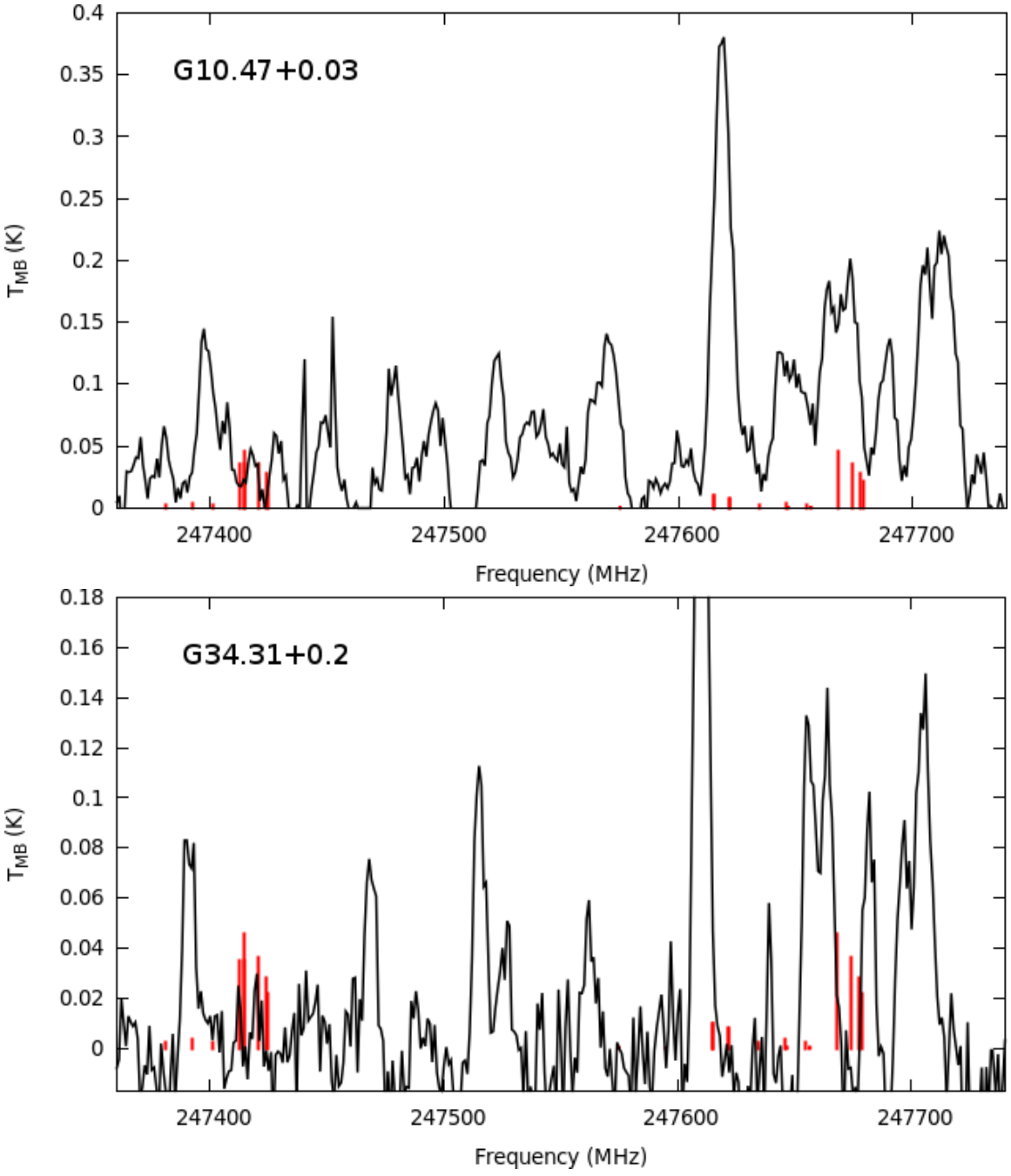

Figure D.2 – Simulated methoxy stick spectrum ($T_{rot} = 10$ K, arb. scaling) atop a portion of the CSO line surveys (cont'd).

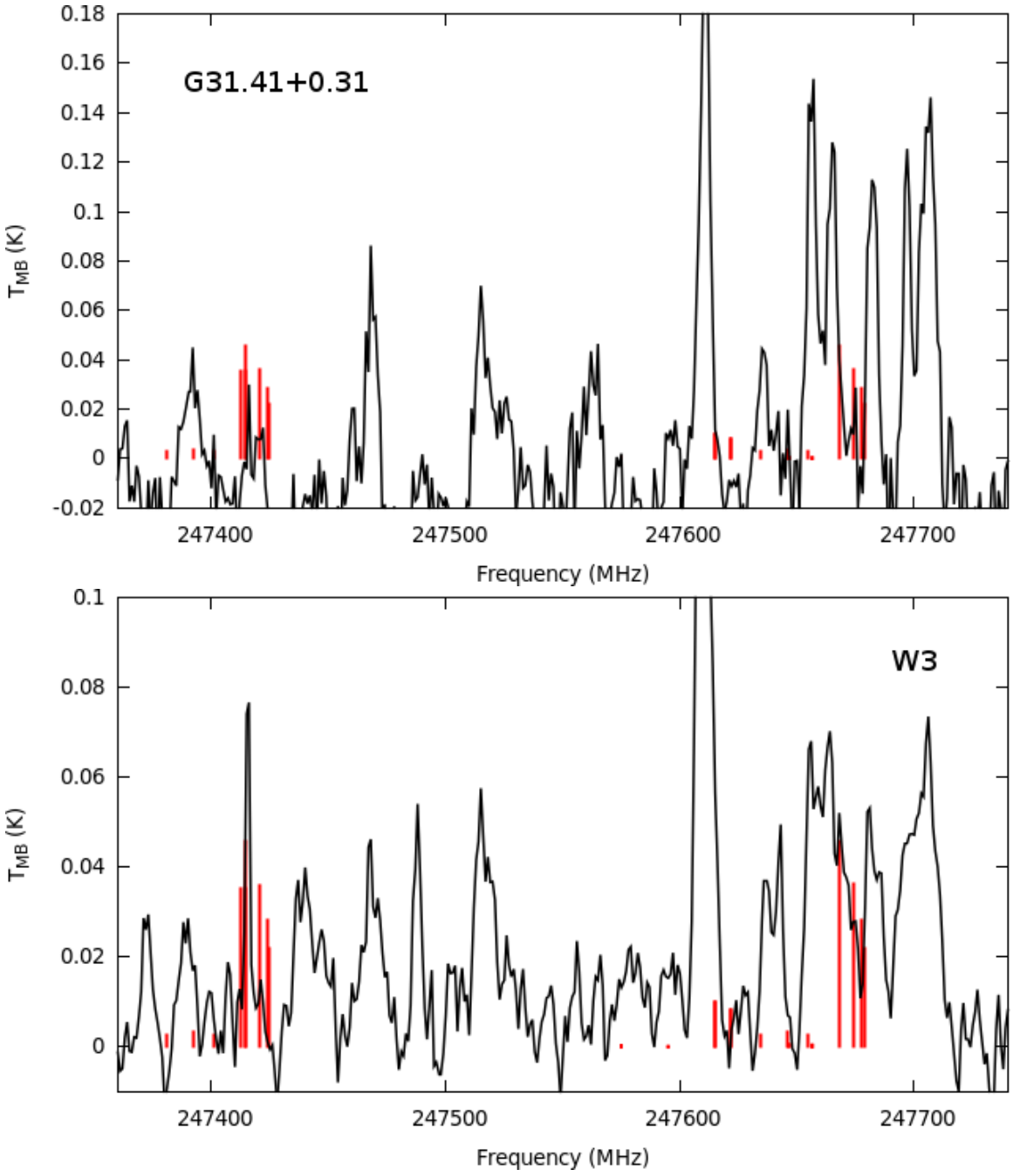

Figure D.3 – Simulated methoxy stick spectrum ($T_{rot} = 10$ K, arb. scaling) atop a portion of the CSO line surveys (cont'd).

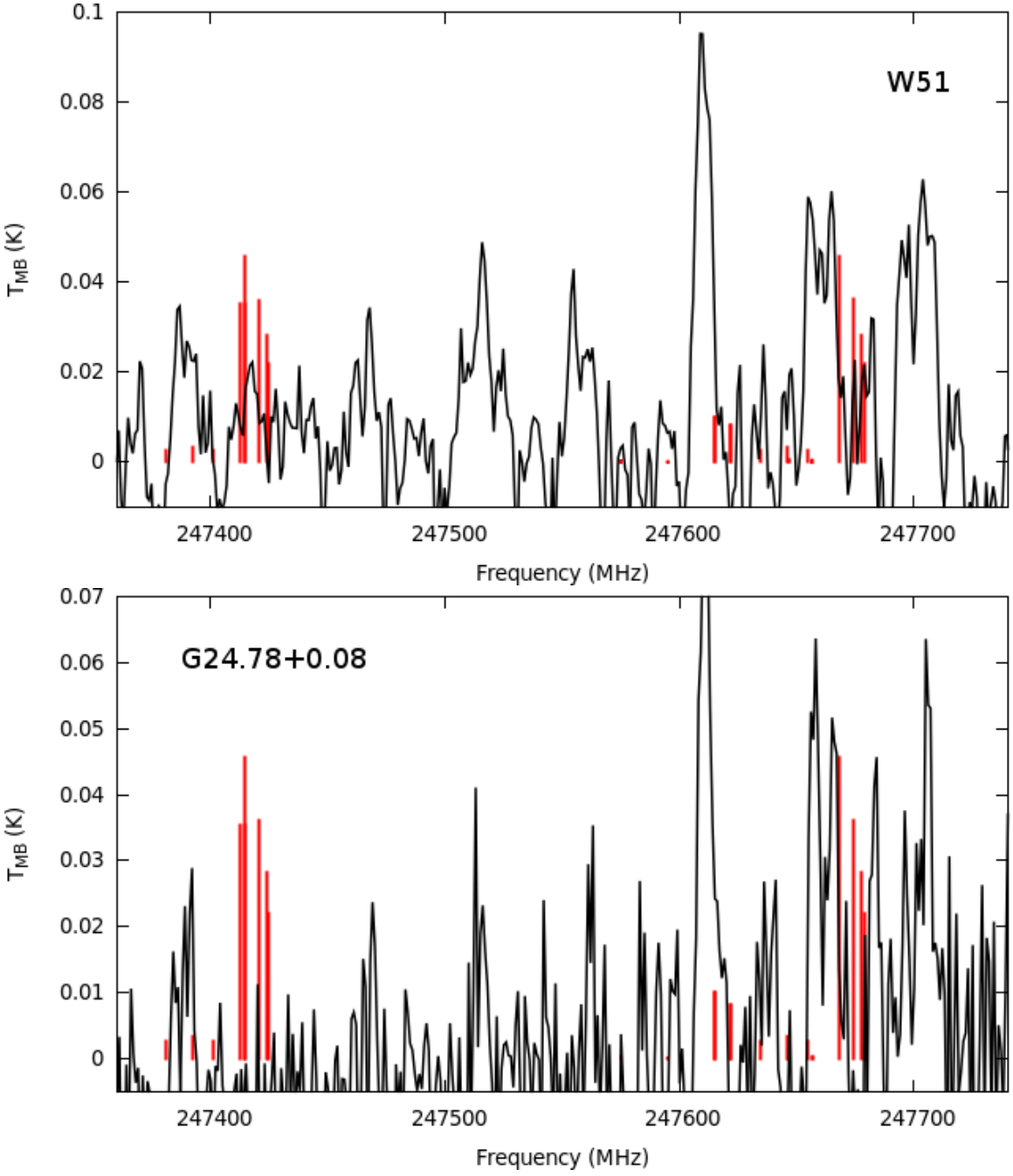

Figure D.4 – Simulated methoxy stick spectrum ($T_{rot} = 10$ K, arb. scaling) atop a portion of the CSO line surveys (cont'd).

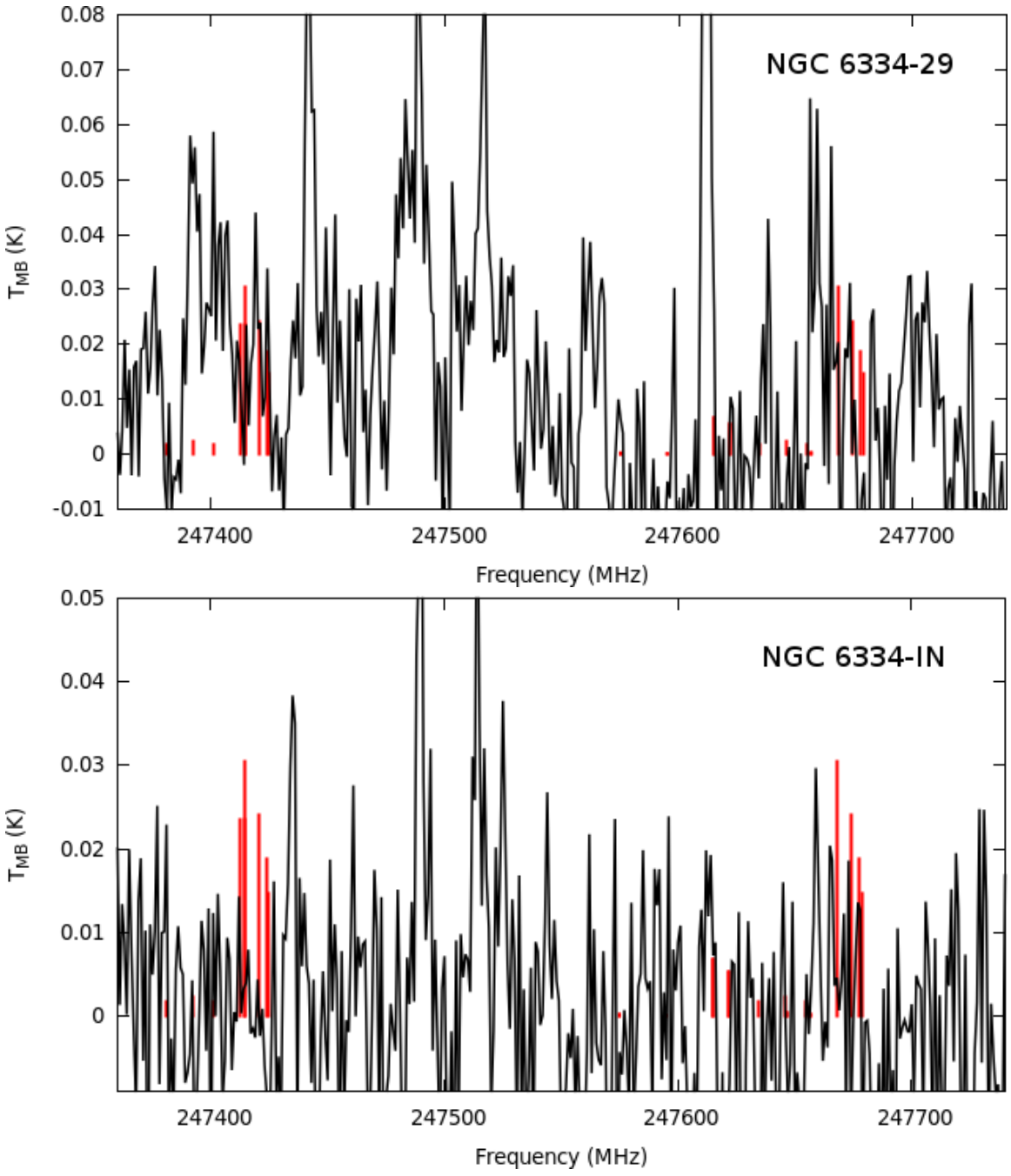

Figure D.5 – Simulated methoxy stick spectrum ($T_{rot} = 10$ K, arb. scaling) atop a portion of the CSO line surveys (cont'd).

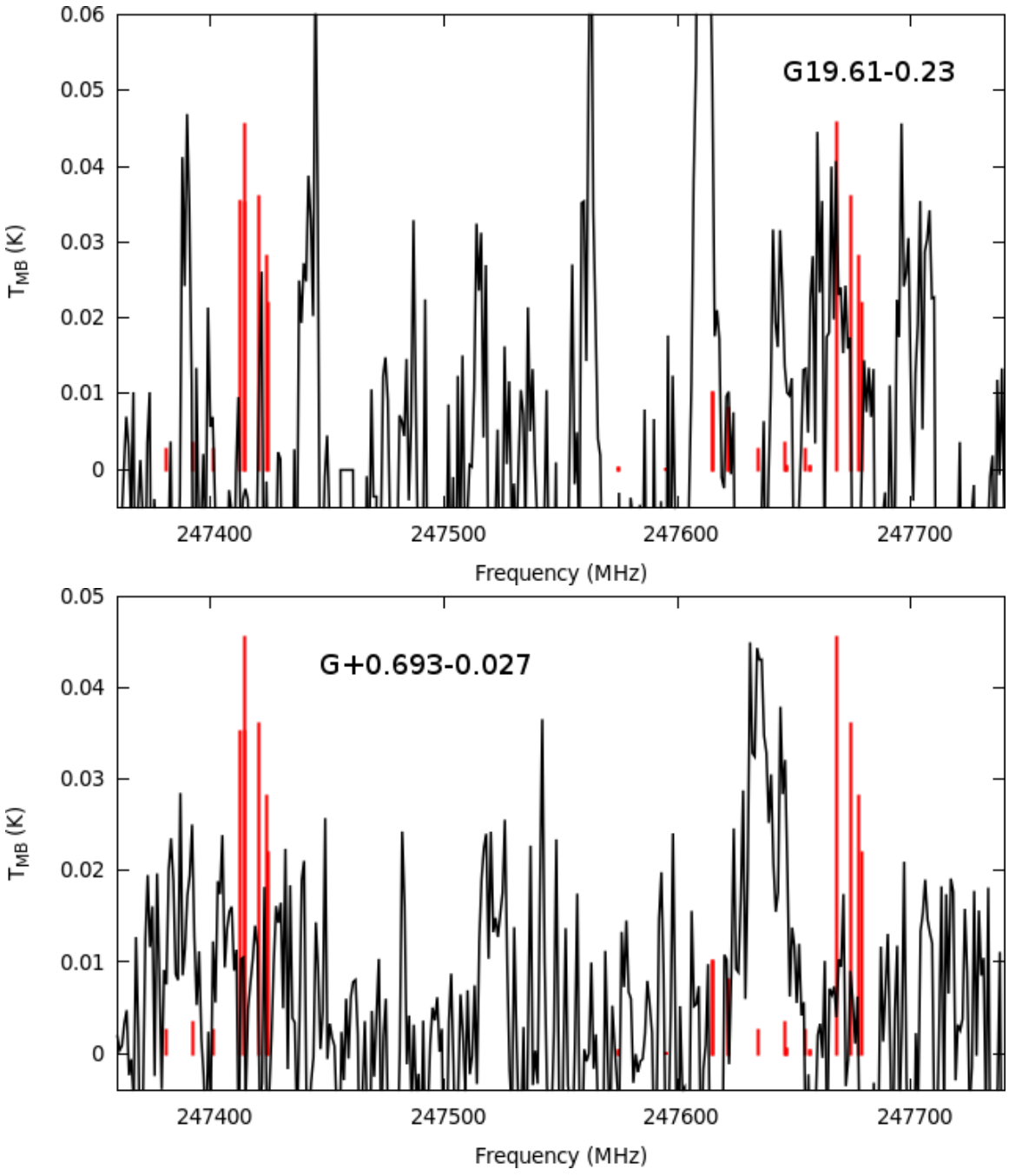

Figure D.6 – Simulated methoxy stick spectrum ($T_{rot} = 10$ K, arb. scaling) atop a portion of the CSO line surveys (cont'd).

Bibliography

Y. Aikawa, V. Wakelam, R. T. Garrod, and E. Herbst. *The Astrophysical Journal*, **2008**, *674*:984–996.

Bridget Alligood DePrince, Blithe E. Rocher, Anne M. Carroll, and Susanna L. Widicus Weaver. *Review of Scientific Instruments*, **2013**, *84*(7).

Robert A. Beaudet and Robert L. Poynter. *Journal of Physical and Chemical Reference Data*, **1978**, *7*(1):311–362.

M. T. Beltrán, C. Codella, S. Viti, R. Neri, and R. Cesaroni. *The Astrophysical Journal, Letters*, **2009**, *690*:L93–L96.

G. A. Blake, J. Farhoomand, and H. M. Pickett. *J. Phys. Chem. Ref. Data*, **1986**, *115*(1): 226–228.

R. Bocquet, J. Demaison, L. Poteau, M. Liedtke, S. Belov, K. M. T. Yamada, G. Winnewisser, C. Gerke, J. Gripp, and Th. Köhler. *Journal of Molecular Spectroscopy*, **1996**, *177*(1):154–159.

S. Bottinelli, C. Ceccarelli, B. Lefloch, J. P. Williams, A. Castets, E. Caux, S. Cazaux, S. Maret, B. Parise, and A. G. G. M. Tielens. *The Astrophysical Journal*, **2004**, *615*: 354–358.

S. Bottinelli, C. Ceccarelli, R. Neri, J. P. Williams, E. Caux, S. Cazaux, B. Lefloch,

S. Maret, and A. G. G. M. Tielens. *The Astrophysical Journal, Letters*, **2004**, *617*: L69–L72.

R. Braakman and G. A. Blake. *Journal of Applied Physics*, **2011**, *109*(6).

N. Brouillet, D. Despois, A. Baudry, T.-C. Peng, C. Favre, A. Wootten, A. J. Remijan, T. L. Wilson, F. Combes, and G. Wlodarczak. *Astronomy and Astrophysics*, **2013**, *550*:A46.

J. M. Brown, L. R. Zink, D. A. Jennings, K. M. Evenson, and A. Hinz. *The Astrophysical Journal*, **1986**, *307*:410–413.

S. Brünken, H. S. P. Müller, F. Lewen, and G. Winnewisser. *Phys. Chem. Chem. Phys.*, **2003**, *5*(8):1515–1518.

Laurie J. Butler and Daniel M. Neumark. *The Journal of Physical Chemistry*, **1996**, *100* (31):12801–12816.

B. W. Carroll and D. A. Ostlie. *An introduction to modern astrophysics*. Pearson Addison-Wesley, San Francisco, 2007. ISBN 9780805304022.

J. Cernicharo, N. Marcelino, E. Roueff, M. Gerin, A. Jiménez-Escobar, and G. M. Muñoz Caro. *The Astrophysical Journal, Letters*, **2012**, *759*:L43.

A. H. H. Chang and S. H. Lin. *Chem. Phys. Lett.*, **2002**, *363*(1–2):175–181.

A.H.H. Chang and S.H. Lin. *Chemical Physics Letters*, **2004**, *384*(4–6):229–235.

Zhichao Chen, Andre T. J. B. Eppink, Bo Jiang, Gerrit C. Groenenboom, Xueming Yang, and David H. Parker. *Phys. Chem. Chem. Phys.*, **2011**, *13*:2350–2355.

B.-M. Cheng, M. Bahou, W.-C. Chen, C.-h. Yui, Y.-P. Lee, and L. C. Lee. *Journal of Chemical Physics*, **2002**, *117*:1633–1640.

C. A. Cole, N. Wehres, Z. Yang, D. L. Thomsen, T. P. Snow, and V. M. Bierbaum. *The Astrophysical Journal, Letters*, **2012**, *754*:L5.

Frank C. De Lucia. *Journal of Molecular Spectroscopy*, **2010**, *261*(1):1–17.

Brian C. Dian, Gordon G. Brown, Kevin O. Douglass, and Brooks H. Pate. *Science*, **2008**, *320*(5878):924–928.

Liam M. Duffy. *Review of Scientific Instruments*, **2005**, *76*(9).

P. Ehrenfreund and S. B. Charnley. *Annual Review of Astronomy and Astrophysics*, **2000**, *38*:427–483.

Yasuki Endo, Shuji Saito, and Eizi Hirota. *The Journal of Chemical Physics*, **1984**, *81*(1): 122–135.

J. Farhoomand, H. M. Pickett, and G. A. Blake. *The Astrophysical Journal, Letters*, **1985**, *291*:L19–L22.

L. Farkas and Y. Hirshberg. *Journal of the American Chemical Society*, **1937**, *59*(11): 2450–2453.

Lin Feng, Jie Wei, and Hanna Reisler. *The Journal of Physical Chemistry A*, **2004**, *108* (39):7903–7908.

Wan Yong Feng and Chava Lifshitz. *The Journal of Physical Chemistry*, **1994**, *98*(24): 6075–6081.

Colin G. Freeman, Peter W. Harland, and Murray J. McEwan. *Australian Journal of Chemistry*, **1978**, *31*(10):2157–2160.

Colin G. Freeman, Peter W. Harland, and Murray J. McEwan. *Australian Journal of Chemistry*, **1978**, *31*(12):2593–2599.

Hugo Fricke and Edwin J. Hart. *The Journal of Chemical Physics*, **1936**, *4*(7):418–422.

R. T. Garrod and E. Herbst. *Astronomy and Astrophysics*, **2006**, *457*:927–936.

R. T. Garrod, V. Wakelam, and E. Herbst. *Astronomy and Astrophysics*, **2007**, *467*:1103–1115.

R. T. Garrod, S. L.. Widicus Weaver, and E. Herbst. *The Astrophysical Journal*, **2008**, *682*: 283–302.

Robin T. Garrod and Susanna L. Widicus Weaver. *Chemical Reviews*, **2013**, *113*(12):8939–8960.

N. Gopalsami, A. C. Raptis, and J. Meier. *Review of Scientific Instruments*, **2002**, *73*(2): 259–262.

T. E. Graedel, W. D. Langer, and M. A. Frerking. *The Astrophysical Journal, Supplement*, **1982**, *48*:321–368.

J. Hagege, P. C. Roberge, and C. Vermeil. *Trans. Faraday Soc.*, **1968**, *64*:3288–3299.

N. Harada, E. Herbst, and V. Wakelam. *The Astrophysical Journal*, **2010**, *721*:1570–1578.

N. Harada, E. Herbst, and V. Wakelam. *The Astrophysical Journal*, **2012**, *756*:104.

S. Harich, J. J. Lin, Y. T. Lee, and X. Yang. *The Journal of Chemical Physics*, **1999**, *111* (1):5–9.

S. Harich, J. J. Lin, Y. T. Lee, and X. Yang. *The Journal of Physical Chemistry A*, **1999**, *103*(49):10324–10332.

Eric Herbst and Ewine F. van Dishoeck. *Annual Review of Astronomy and Astrophysics*, **2009**, *47*(1):427–480.

H. Hoch and F. Patat. *Z. Elektrochem.*, **1935**, *41*(7):494–498.

J. M. Hollis, F. J. Lovas, and P. R. Jewell. *The Astrophysical Journal, Letters*, **2000**, *540*: L107–L110.

J. M. Hollis, P. R. Jewell, F. J. Lovas, and A. Remijan. *The Astrophysical Journal, Letters*, **2004**, *613*:L45–L48.

A. Horn, H. Møllendal, O. Sekiguchi, E. Uggerud, H. Roberts, E. Herbst, A. A. Viggiano, and T. D. Fridgen. *The Astrophysical Journal*, **2004**, *611*:605–614.

S. B. Howell. The Latest Results from the NASA Kepler Mission: Exoplanets and Astrophysics. In *American Astronomical Society Meeting Abstracts*, volume 222 of *American Astronomical Society Meeting Abstracts*, page 300.01, June 2013.

Wen-Chiun Ing, Chad Y. Sheng, and Joseph W. Bozzelli. *Fuel Processing Technology*, **2003**, *83*(1-3):111–145.

J. K. Jørgensen, C. Favre, S. E. Bisschop, T. L. Bourke, E. F. van Dishoeck, and M. Schmalzl. *The Astrophysical Journal, Letters*, **2012**, *757*:L4.

Tim P. W. Jungkamp, Ulf Kirchner, Mark Schmidt, and Ralph N. Schindler. *Journal of Photochemistry and Photobiology A: Chemistry*, **1995**, *91*:1–6.

Devinder Kaur, A. M. de Souza, J. Wanna, Sameer A. Hammad, Louis Mercorelli, and David S. Perry. *Applied Optics*, **1990**, *29*(1):119–124.

W. F. Kolbe and B. Leskovar. *Review of Scientific Instruments*, **1985**, *56*(8):1577–1581.

M. J. Krisch, L. R. McCunn, K. Takematsu, L. J.Butler, F. R. Blase, and J. Shu. *J. Phys. Chem. A*, **2004**, *108*:1650–1656.

J. C. Laas, R. T. Garrod, E. Herbst, and S. L. Widicus Weaver. *The Astrophysical Journal*, **2011**, *728*:71.

Jacob C. Laas, Brian M. Hays, and Susanna L. Widicus Weaver. *The Journal of Physical Chemistry A*, **2013**, *117*(39):9548–9554.

Jinjun Liu, Ming-Wei Chen, Dmitry Melnik, Terry A. Miller, Yasuki Endo, and Eizi Hirota. *The Journal of Chemical Physics*, **2009**, *130*:074303.

Jinjun Liu, Ming-Wei Chen, Dmitry Melnik, John T. Yi, and Terry A. Miller. *The Journal of Chemical Physics*, **2009**, *130*:074302.

M. A. Requena-Torres, J. Martín-Pintado, A. Rodríguez-Franco, S. Martn, N. J. Rodríguez-Fernández, and P. de Vicente. *Astronomy and Astrophysics*, **2006**, *455*(3):971–985.

M. C. McCarthy, W. Chen, M. J. Travers, and P. Thaddeus. *The Astrophysical Journal, Supplement*, **2000**, *129*(2):611.

B. A. McGuire, P. B. Carroll, and A. J. Remijan. *ArXiv e-prints*, **2013**.

Dmitry G. Melnik, Jinjun Liu, Ming-Wei Chen, Terry A. Miller, and Robert F. Curl. *The Journal of Chemical Physics*, **2011**, *135*(9):26pp.

Takamasa Momose, Yasuki Endo, Eizi Hirota, and Tadamasa Shida. *The Journal of Chemical Physics*, **1988**, *88*(9):5338–5343.

Holger S. P. Müller, Frank Schlöder, Jürgen Stutzki, and Gisbert Winnewisser. *Journal of Molecular Structure*, **2005**, *742*(1–3):215–227. URL `http://www.astro.uni-koeln.de/cdms/`.

M. J. Mumma and S. B. Charnley. *Annual Review of Astronomy and Astrophysics*, **2011**, *49*:471–524.

J. L. Neill, A. L. Steber, M. T. Muckle, D. P. Zaleski, V. Lattanzi, S. Spezzano, M. C. McCarthy, A. J. Remijan, D. N. Friedel, S. L. Widicus Weaver, and B. H. Pate. *Journal of Physical Chemistry A*, **2011**, *115*:6472–6480.

J. L. Neill, M. T. Muckle, D. P. Zaleski, A. L. Steber, B. H. Pate, V. Lattanzi, S. Spezzano, M. C. McCarthy, and A. J. Remijan. *The Astrophysical Journal*, **2012**, *755*:153.

A. Nummelin, P. Bergman, A. Hjalmarson, P. Friberg, W. M. Irvine, T. J. Millar, M. Ohishi, and S. Saito. *The Astrophysical Journal, Supplement*, **1998**, *117*:427.

K. I. Öberg, R. T. Garrod, E. F. van Dishoeck, and H. Linnartz. *Astronomy and Astrophysics*, **2009**, *504*:891–913.

K. I. Öberg, S. Bottinelli, J. K. Jørgensen, and E. F. van Dishoeck. *The Astrophysical Journal*, **2010**, *716*:825–834.

Tatsuo Oguchi, Akira Miyoshi, Mitsuo Koshi, and Hiroyuki Matsui. *Bull. Chem. Soc. Jpn.*, **2000**, *73*(1):53–60.

Erik A. Petigura, Andrew W. Howard, and Geoffrey W. Marcy. *Proceedings of the National Academy of Science*, **2013**, *110*(48):19273–19278.

H. M. Pickett, R. L. Poynter, E. A. Cohen, M. L. Delitsky, J. C. Pearson, and H. S. P. Müller. *J. Quant. Spec. and Rad. Trans.*, **1998**, *60*(5):883–890.

Sandra Pizzarello, Stephen K. Davidowski, Gregory P. Holland, and Lynda B. Williams. *Proceedings of the National Academy of Science*, **2013**.

Raymond P. Porter and W. Albert Noyes, Jr. *Journal of the American Chemical Society*, **1959**, *81*(10):2307–2311.

John S. Ridgen and Samuel S. Butcher. *J. Chem. Phys.*, **1964**, *40*(8).

M. A. Roberts, E. N. Sharp-Williams, and D. J. Nesbitt. *Journal of Physical Chemistry A*, **2013**, *117*:7042–7049.

Sunita Satyapal, Jeunghee Park, Richard Bersohn, and Benjamin Katz. *The Journal of Chemical Physics*, **1989**, *91*(11):6873–6879.

C. A. Schmuttenmaer, R. C. Cohen, N. Pugliano, Heath, A. L. Cooksy, K. L. Busarow, and R. J. Saykally. *Science*, **1990**, *249*(4971):897–900.

L. E. Snyder. *Proceedings of the National Academy of Science*, **2006**, *103*:12243–12248.

E. C. Sutton, R. Peng, W. C. Danchi, P. A. Jaminet, G. Sandell, and A. P. G. Russell. *The Astrophysical Journal, Supplement*, **1995**, *97*:455–496.

E. Vigren, M. Hamberg, V. Zhaunerchyk, M. Kaminska, J. Semaniak, M. Larsson, R. D. Thomas, M. a. Ugglas, I. Kashperka, T. J. Millar, C. Walsh, H. Roberts, and W. D. Geppert. *The Astrophysical Journal*, **2010**, *709*:1429–1434.

C. Walsh, T. J. Millar, and H. Nomura. *The Astrophysical Journal*, **2010**, *722*:1607–1623.

C. Walsh, H. Nomura, T. J. Millar, and Y. Aikawa. *The Astrophysical Journal*, **2012**, *747*: 114.

C. Walsh, T. J. Millar, H. Nomura, E. Herbst, S. Widicus Weaver, Y. Aikawa, J. C. Laas, and A. I. Vasyunin. *Astronomy and Astrophysics*, **2014**, *563*:A33.

S. L. Widicus Weaver and D. N. Friedel. *The Astrophysical Journal, Supplement*, **2012**, *201*:16.

E. S. Wirström, W. D. Geppert, Å. Hjalmarson, C. M. Persson, J. H. Black, P. Bergman, T. J. Millar, M. Hamberg, and E. Vigren. *Astronomy and Astrophysics*, **2011**, *533*:A24.

D. E. Woon and E. Herbst. *The Astrophysical Journal, Supplement*, **2009**, *185*:273–288.

W. S. Xia, R. S. Zhu, M. C. Lin, and A. M. Mebel. *Faraday Discuss.*, **2002**, *119*:191–205.

L. M. Ziurys. *Proceedings of the National Academy of Science*, **2006**, *103*:12274–12279.